Large Scale Anisotropy of Ultra-High Energy Cosmic Rays measured by Telescope Array Experiment

23　12　　　（　　）

Abstract

The origin of Ultra-High Energy Cosmic Rays (UHECRs) is one of the most interesting questions in astroparticle physics. Despite the efforts by previous experiments, there is no consensus on the origin and the propagation of UHECRs.

Telescope Array (TA) experiment observes air shower generated by UHE-CRs using an array of surface particle detectors (SDs) and fluorescence detectors (FDs) and other important calibration devices.

The TA is installed in the desert of Utah, USA, about 1400 m above sea level (39.3° N and 112.9° W). TA experiment has 507 SDs with 1.2 km spacing covering about 700 km^2 ground area. We searched for large scale anisotropy using SD data taken from May 2008 until May of 2011.

The range of UHECR propagation is expected to be restricted in the short distance because of their interaction with Cosmic Microwave Background (CMB) photons. The observed arrival directions are expected to correlate with local large scale structure (LSS) if UHECR sources are some astrophysical objects.

We used galaxies in 2 Mass Extended Source Catalogue to represent the matter distribution in the LSS and calculated the propagation of protons to the Earth. The deflections by the regular Galactic Magnetic Field (GMF) is taken into account. The random magnetic deflections of UHECRs in the Galactic and Extra-Galactic space are included. We compared the arrival directions of UHECRs with the expected flux from the matter using one-dimensional Kolmogorov-Smirnov (KS) test.

As a result, we observed the UHECR arrival directions are compatible with the isotropy and no clear deviation is observed. The UHECR data is also compatible with the proton LSS model when the effect of appropriate GMF is taken into account.

Contents

1. Introduction

The origin of Ultra-High Energy Cosmic Rays (UHECRs) is one of the most interesting questions in astroparticle physics. Despite the efforts by previous experiments, there is no consensus on the origin and the propagation of UHECRs.

In this context, Telescope Array (TA) experiment[1, 2] is expected to play an important role as the largest detector in the northern hemisphere which consists of an array of surface particle detectors (SDs) and fluorescence detectors (FDs) and other important calibration devices like Electron Light Source (ELS), Center Laser Facility(CLF) and others.

The energy spectrum, composition, and arrival directions are main items to be measured. They include direct information about the origin of UHE-CRs.

Energy spectra of UHECRs measured by Akeno Giant Air Shower Array (AGASA) [3], High Resolution Fly's Eye (HiRes) [4], Pierre Auger and Yakutsk experiments differ from each other. UHECRs are expected to be restricted in the short distance because they cannot keep their energy because of the interaction with Cosmic Microwave Background (CMB) photons. The contribution of energy flux from distant sources sharply decreases at higher energies from this reason and this is expected to result in the flux suppression at the highest energies. This process is known as Greisen-Zatsepin-Kuzmin (GZK) limit [5] and the interaction mainly consists of pion photo-production and electron-positron pair production when the UHECR is a proton.

However, the AGASA data did not find the flux suppression. On the other hand, the HiRes experiment observed the flux suppression [11], and the Pierre Auger experiment confirmed the appearance of the flux suppression [7].

Except for the flux suppression, the measured energy spectra by the different experiments are in good agreement after energy shift at the dip, which may be a feature predicted by electron-positron pair production in collisions of protons with CMB photons [6]. It suggests that the shape of the energy spectra is rather consistent with each other and the understanding of the difference of the energy scales of experiments is an issue. The preliminary result of TA experiment confirmed the appearance of the flux suppression more than 3 σ level below continuous energy flux [8, 9].

Xmax is the atmospheric depth of the shower max at which number of sec-

ondary electrons of UHECRs in the atmosphere reaches maximum. Xmax is known as the parameter which is sensitive to the composition of the primary particle.

Xmax distribution of UHECRs measured by Pierre Auger [10] and HiRes [11] experiments also differ from each other. The average and dispersion of Xmax distribution are in good agreement with pure proton QGSjet models according to HiRes experiment. But on the other hand, the average and dispersion of Xmax distribution does not agree with pure proton models and suggests the heavier component of the composition in case of Pierre Auger experiment. The preliminary Xmax result of TA experiment is quite consistent with pure proton QGSjet models as HiRes experiment [12].

Arrival direction distribution of UHECRs is observed in many experiments and studied by many authors, but did not result in clear origins.

To search for auto-correlation is a direct way to search for point-like sources using only observed arrival directions. AGASA found small scale anisotropy of the arrival distribution of UHECRs above 40 EeV within 2.5 degrees, which is comparable with its angular resolution [13]. On the other hand, HiRes did not find any significant signals for any point-like sources [17, 18]. The cumulative auto-correlation of the arrival directions which were observed by Pierre Auger was shown in Ref.[19]. The largest deviation of the auto-correlation from the isotropic expectation corresponds to a little more than 95 % confidence level for an angular scale of 11 degrees, and there is no significant signal. The auto-correlation of the preliminary arrival directions which were observed by TA SD was not significant [20].

To search for cross correlation is a way to extract the common properties of sources. The correlation with BL Lac objects was discussed by using the AGASA and Yakutsk data [14–16]. The authors of Ref. [21] made a comprehensive study of correlation with various classes of powerful extragalactic sources and found that BL Lac objects and unidentified gamma-ray sources might be correlated with the AGASA and Yakutsk data. Cross correlation of UHECRs observed by HiRes with BL Lac objects studied by Refs. [14–16] was not supported by the HiRes data [22]. Pierre Auger experiment showed the spatial cross correlation between the arrival directions of its 27 events above 57 EeV and the positions of nearby active galactic nuclei (AGNs) from Véron-Cetty and Véron (VCV) catalogue with much more than 3 σ confidence level [23, 24]. After the report, the confidence level of the correlation decreased much, but the correlation in 99.7 % confidence level exists also using updated results [19].

Large scale anisotropy is a more general anisotropy predicted by several authors [25–28]. HiRes reported disagreement with local large scale structure (LSS) which is constructed using 2MRS catalogue within the angular scale of 10 degrees above 40 EeV and 57 EeV with more than 95 % confidence level [29].

Our analysis started from our results of energy spectrum and pure proton composition. UHECRs are expected to be restricted in the short distance from flux suppression at high energies, so arrival directions are expected to exhibit local large scale anisotropy because of smaller magnetic deflections.

The trigger efficiency of our SD array reaches almost 100% when the energy of UHECRs is above 10 EeV in this cut condition. This efficiency results in the flat and constant acceptance of our SD array. The observation with our array is continuous to have about 100% duty cycle, which gives seasonal flatness of the acceptance. This feature of the acceptance is quite different from that of FD data. In addition to that, the statistics of SD data is larger than that of FD data. These features of SD data are good to explore the anisotropy. So we used SD data for this study.

We reviewed the recent progress of the study of candidates of UHECR sources as astrophysical objects, and propagation of UHECRs and observation results in Section 2. In Section 3, we described the detailed information of TA detectors and data acquisition systems. Monte Carlo simulation (MC) which we developed is described in Section 4. The detailed data reduction including calibrations is described in Section 5. The methods and results of large scale anisotropy search using the data described in the previous section are explained in Section 6. Summary and conclusion are shown in Section 7.

2. Review of Ultra-High Energy Cosmic Ray Physics

Today, UHECRs are observed in several experiments which have large acceptance and even about more than 100 EeV UHECRs are actually observed. On the other hand, the origin and the generation mechanism of the UHECRs are very poorly known. This situation may be partially because of the difficulty of the interpretation of observation results some of which look contradicted and partially because of the very small statistics and partially because of the difficulty to measure the intergalactic and the Galactic magnetic field precisely.

In this section, we review this situation of UHECRs starting from rather theoretical point of view. The constraints of sources are based on the criterion of particle acceleration known as Hillas criterion and the studied acceleration mechanisms which make the expected injection spectrum are shown in Section 2.1. In Section 2.2, we review the propagation processes including interaction with CMB photons which may be the cause of observed flux suppression and including magnetic deflection which may have a big influence on the observed arrival direction distribution. The observation method using extensive air shower (EAS) generated by UHECRs is described in Section 2.3, and we review the observation results in Section 2.4.

2.1. Source Candidates and Cosmic Ray Acceleration

- Updated Hillas plot including radiation losses.

  Candidates of UHECR sources need to satisfy some physical requirements to accelerate particles to ultra-high energy. As summarized in Ref.[30], UHECR sources should have enough power and geometry where the accelerated particles can be kept inside while being accelerated, while the magnetic and photon fields cannot be too strong to avoid large radiation and photo-meson energy losses. UHECR sources should satisfy also observed conditions such as UHECR energy spectra, photon limits and neutrino limits and so on.

  One simple criterion about the geometry was considered long ago. The accelerated particle is presumably confined by the magnetic field, so the particle's Larmor radius should not exceed the size of the candidate of the UHECR source, while the particle is being accelerated. This criterion is recognized as the Hillas criterion [31], and is often presented as the Hillas plot where the size of the accelerator and the magnetic field strength are plotted.

7

In Fig.1, not only the Hillas criterion but also the criterion of synchrotron radiation losses for each type of candidates are considered as shaded regions.
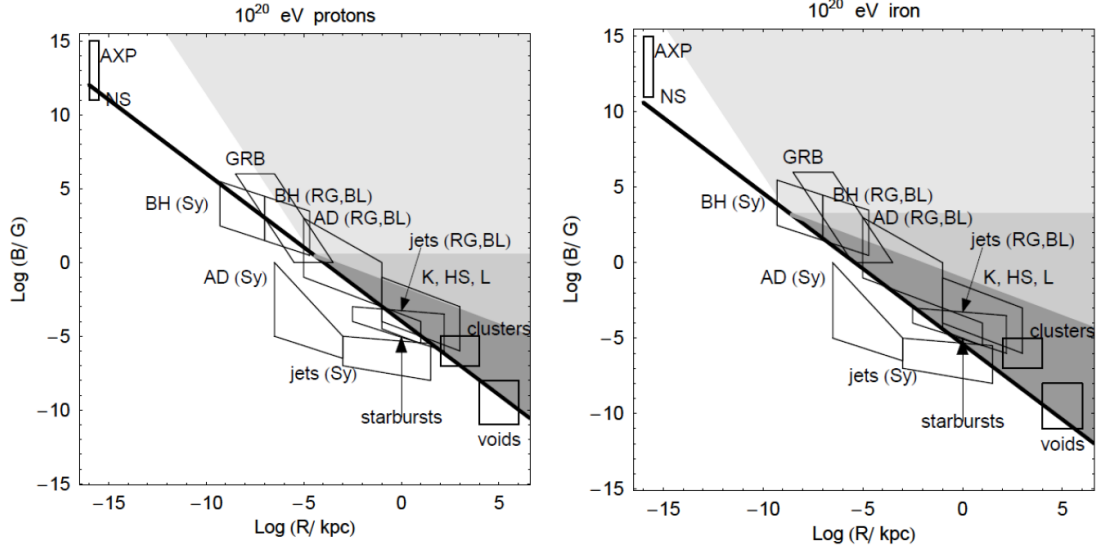

Figure 1: Updated Hillas plot considering criterion of the geometry and the synchrotron radiation loss. Left figure is the criterion of 100 EeV protons. Right figure is the criterion of 100 EeV irons. Boxes denote parameter regions for various objects. NS:neutron stars, AXP: anomalous X-ray pulsars and magnetors, BH: super-massive central black holes of AGN from low power Seyfert galaxies (Sy), to powerful radio galaxies (RG) and blazers (BL). AD: central parsecs of active galaxies from Sy, RG, and BL. K:relativistic knots, HS: hot spots, and L:lobes of powerful galaxies. The thick line represents the lower boundary of the area allowed by the Hillas criterion. Shaded areas are allowed by the radiation loss. Light gray, gray and dark gray assume different conditions of accelerations. Light gray and gray do not consider diffusive process and light gray does not consider synchrotron radiation loss but radiation loss in the ordered field in the very specific configuration. Dark gray region is allowed by synchrotron radiation loss in the diffusive acceleration process. [30]

Several possible candidates of UHECR sources are often discussed in this literature. As candidates of UHECR sources, radio-loud AGNs are discussed in Ref.[32–39], gamma-ray bursts (GRBs) are discussed in Ref.[40–45], and low luminosity GRBs and hypernovae are considered in Ref.[46, 47]. Accelerations in the vicinity of black holes are considered [48–52], and magnetors and clusters of galaxies are also discussed as UHECR sources [53–57].

- Acceleration Mechanisms

Acceleration mechanisms of particles determine the concrete injection energy spectrum of the UHECR source. From the observations of cosmic-ray energy spectra, it is clear that the spectra universally follow power-law. (See Fig.2)

The first-order [58] and second-order [59] Fermi acceleration generate power-law energy spectrum. In Fermi's original paper, the collision between a particle and a massive cloud was assumed. An infinitely massive cloud with unchanged velocity collides with particles which have random incident angles in the hydromagnetic waves or irregularities in the magnetic field. These collisions result in power-law energy spectra in average. Second-order Fermi acceleration considers an additional term to describe the diffusion of the particles in momentum space.

Bell's simple model is the first order Fermi acceleration assuming only the presence of strong shock waves and that the velocity vectors of the high energy particles are randomized on either side of the shock [60]. This model gives the unique index of differential energy spectrum, -2. This mechanism seems to explain the physical reasons why power-law energy spectra with a unique spectral index should occur in various astrophysical environments.

Different concrete acceleration conditions for shock acceleration like this kind of diffusive acceleration are considered as following.

The accelerated particle crosses a boundary between layers with different velocities in the shock [61–63]. In case of ultrarelativistic shocks in AGN jets, in the case of isotropic scattering of particles, the acceleration energy spectrum index is -2.23 $\pm$ 0.01 according to Ref.[64]. This index depends on scattering properties of the medium [65, 66]. The large angle scattering was found to make -2.7 acceleration energy spectrum index [65]. The effect of compression of upstream magnetic field results in decreasing acceleration energy spectrum index [66].

In case of mildly relativistic internal shocks of GRBs, the acceleration energy spectrum index is about -2 according to Ref.[67, 68]. In case of ultrarelativistic external shocks of GRBs, the condition of the acceleration is similar to AGN jets.

9

Inductive(one-shot, or direct) acceleration mechanisms other than diffusive acceleration are also considered [31]. The particle is expected to be accelerated by large scale electric field in this mechanism. Strong ordered fields on relatively large scales are required. Large scale jets case [39] and the case of neutron stars [55] and black holes [50–52] are considered.

- Implication of the type of astrophysical objects on the UHECR observations

  From the point of UHECR observations, astrophysical objects considered above can be categorized into persistent and transient sources. Flare like burst emitted from AGNs and GRBs are categorized as transient sources. If UHECR sources are transient sources like GRBs, it is expected to be quite difficult to identify a GRB as a source of an UHE charged particle which is observed on the Earth, because charged particle arrive at the Earth much later than the arrival of photons because of the existence of magnetic field as mentioned later in this section. So spatial cross correlation search between UHECR arrival directions and persistent sources like AGNs were tried, when we want to find out some kinds of persistent sources [14–16, 19, 21–24].

2.2. Cosmic Ray Propagation

2.2.1. Energy Losses of UHECRs

The accelerated UHE particles which started from some astrophysical objects, need to keep their energies to reach the Earth to be observed as UHECRs. The space is filled with about 410 (/cm^3) CMB photons universally, so the interaction of the UHE particles with CMB photons is thought to be the most important process for UHE particles to lose their energies.

Here, we show several important energy loss processes to consider the propagation of UHECRs.

1. Adiabatic Energy Losses
   Adiabatic energy losses occur inevitably by the cosmological expansion. This energy loss is given by

$$-E^{-1}dE/dt = H(z). \tag{1}$$

   Here, $H(z) = H_0\sqrt{(1 + z)^3\Omega_m + \Omega_\Lambda}$, where $H_0 = 72$ km/s/Mpc $\Omega_m = 0.27$ and $\Omega_\Lambda = 0.73$ according to [70].
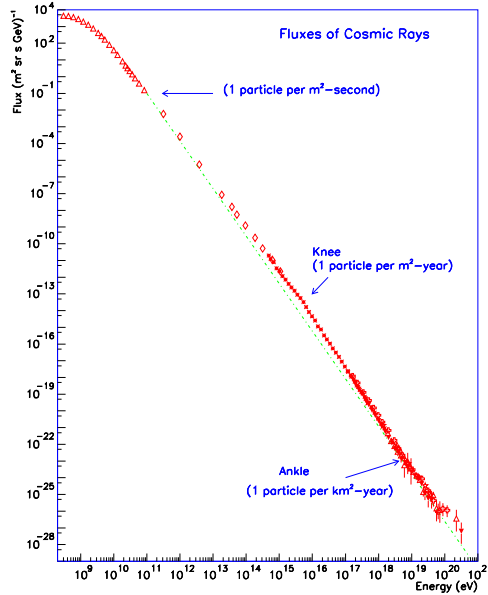
Figure 2: Compilation of observed differential energy spectra [69]. Green broken line is the energy spectrum with -2.7 power index. [1]

2. Electron-positron pair production

   Electron-positron pair production induced by CMB photons does not break the accelerated nuclei. In case of proton, this process is expressed as $p + \gamma_{CMB} \rightarrow p + e^+ + e^-$. This process is important around 10 EeV in case of proton as we can see in Fig.3. On the other hand, this process is important around when Lorentz factor Γ is a little above 10^9 which corresponds to a little above 60 EeV in case of iron as we can see in Fig.4.

3. Pion production

   This proton process becomes the dominant process of the energy above about 60 EeV. This process is expressed as $p + \gamma_{CMB} \rightarrow N + \pi$. The expected sharp steepening energy spectrum due to this process is recognized as GZK cutoff [5].

4. Photo-disintegration

   This process of UHE cosmic ray nuclei becomes the dominant process when Lorentz factor is above about $3 \cdot 10^9$ which corresponds to a little above 180 EeV in case of iron. This process is expressed as $A + \gamma_{CMB} \rightarrow$

11

$(A-1)+1$, $A+\gamma_{CMB} \to (A-2)+2...$ In the lower energy, the leading process of this process is one and two nucleon emission process.

As emphasized in Ref.[6], the dip feature of energy spectrum can be given by the pair production process of proton. And steep flux suppression of higher energy UHECRs can be given both by pion production process and photo-disintegration process.

For UHECR arrival direction analysis, this remarkable flux suppression caused by pion production process of UHECR proton is important. Because of this process, UHECR protons which is more than about 60 EeV cannot travel more than 200 Mpc from the source [71].

UHECR heavy nuclei sources are also expected to be restricted to nearby extra galactic sources because of photo-disintegration process. But in this case, the influence of magnetic deflection is expected to be serious as described in the following section.
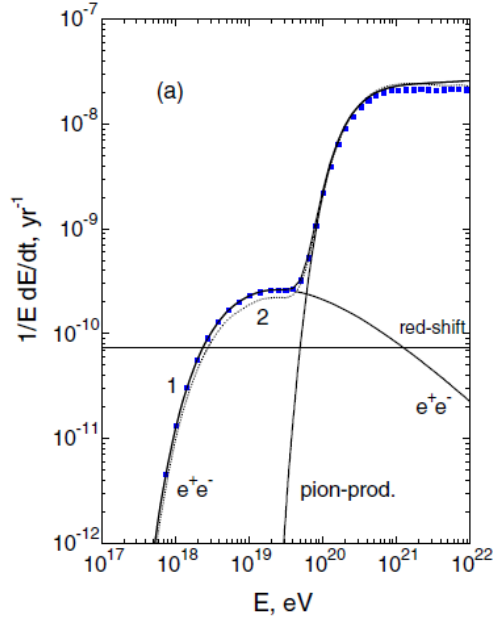

Figure 3: UHE proton energy losses $E^{-1} \cdot dE/dt$ at z = 0 [6].

The distance dependence of the contribution to the observed flux is shown in Fig.5 when we assume the uniform source density, changing the consideration of the processes of the proton propagation. The left top figure shows
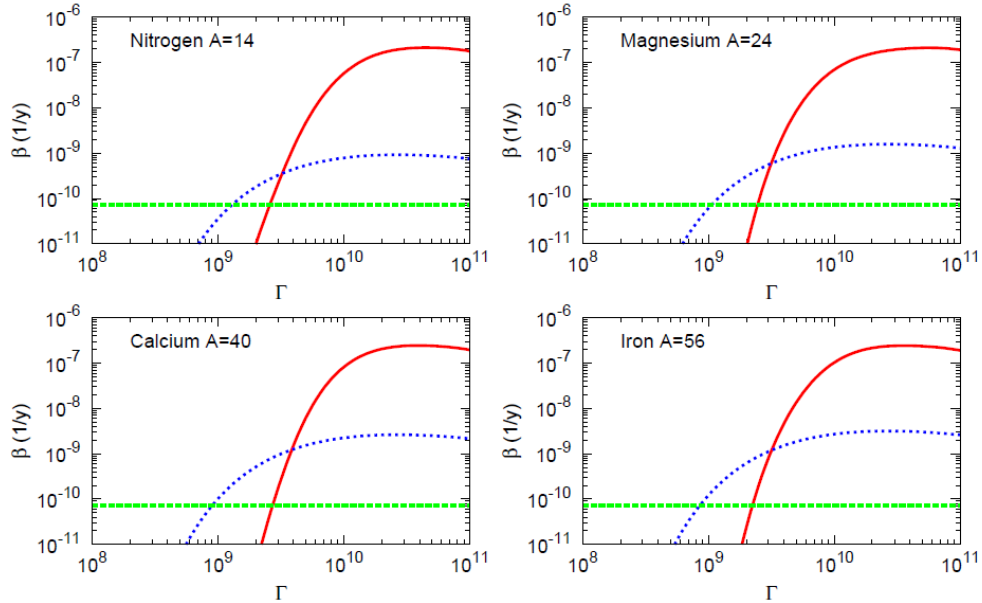
Figure 4: Energy losses for heavy nuclei due to photo-disintegration and pair production on CMB (red full line and blue dotted line, respectively) and adiabatic energy loss (green dashed line) [72]. The horizontal axis is the Lorentz factor of the nuclei.

the case considering only D^{-2} diffusion. Number of sources is proportional to D^2, so the contribution to the flux is same at each distance in this case. The fraction within a few hundred Mpc increases about 2 times larger with pair production process than the case only with diffusion at around 10 EeV as shown in the difference between the right top figure and the left bottom figure. And we can see that the fraction within a few hundred Mpc drastically increases above 40 EeV with pion production process, which is known as GZK limit.

2.2.2. Extra Galactic Magnetic Field

The magnetic deflection of UHE protons by intergalactic magnetic field is simulated by several authors. When SPH (smoothed particle hydrodynamics) simulation with magnetic field is done, the magnetic deflection angle is much less than $1°$ for 100 EeV protons in Ref.[73]. In this simulation, the mean magnetic field strength in filament is about 0.1-0.01nG according to the figure 7 in this reference.
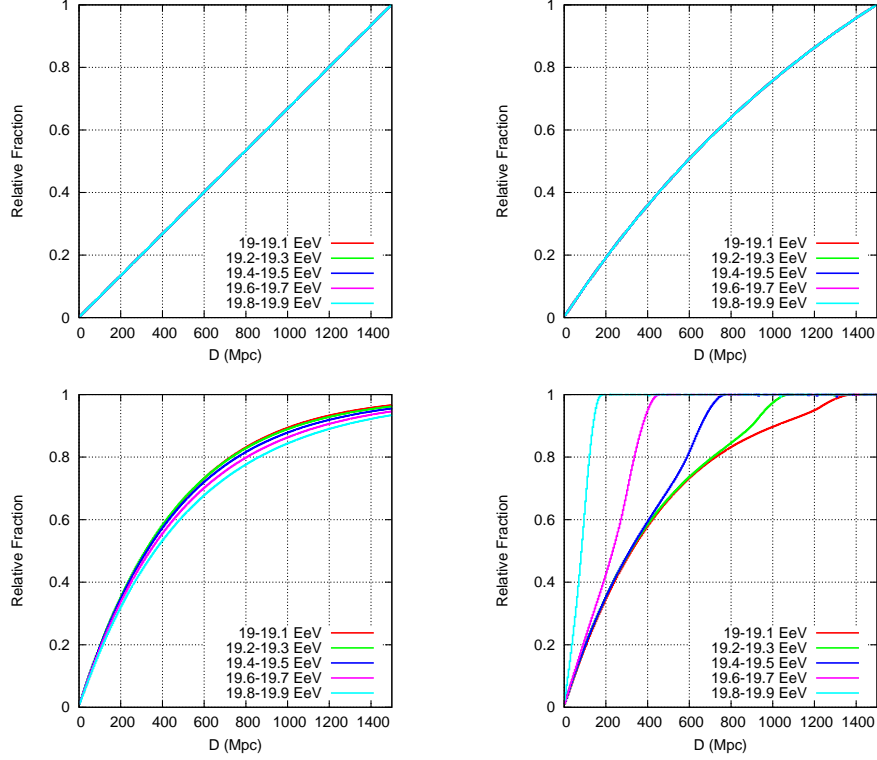
13

Figure 5: The distance dependence of the fraction of the contribution to the observed flux is shown in these figures when we assume the uniform source density and injection energy spectrum $E^{-2.62}$, changing the consideration of the processes of the propagation. The vertical axis in each figure means the cumulative fraction of the contribution to the observed flux within the distance. The different colors mean the different observed energy range. The left top figure considers only D^{-2} diffusion. The right top figure considers diffusion with redshift loss. The bottom left figure considers diffusion, redshift loss and electron positron pair production energy loss interacting with CMB photons. The bottom right figure considers diffusion, redshift loss, pair production loss and pion production energy loss interacting with CMB photons.

14

When hydrodynamics simulation is done, the mean deflection angle is about 15° for 100 EeV protons in Ref.[74]. 3-4° separation angles between events remain even with such large deflection angles according to the paper. In this simulation, the average magnetic field strength in filament is about 10 nG.

When another hydrodynamics simulation is done, the magnetic deflection angle can be about 20° for 100 EeV protons in Ref.[75]. In this simulation, the extra galactic magnetic field strength located in the filament-like structure is about 100 nG.

The results of simulation seem to be different about 1 order of magnetic field deflection angle and 3-4 order of magnetic field strength.

The arrival time delay of observed events of UHE protons compared with the travel time of light is also calculated in Ref.[76]. Average time delay compared with light travel time is about 1 Gyrs for around 10 EeV UHE protons, and about 100 kyrs for around 100 EeV UHE protons according to this reference. The arrival time delay of UHECR nuclei would be estimated to be longer than these results. This too much delay vanishes the meaning of arrival time distribution of UHECRs to identify astrophysical sources. We cannot observe UHECRs during this time range.

2.2.3. Irregular Galactic Magnetic Field

In Ref.[77, 78] the deflections of UHECRs in the random Galactic magnetic fields are estimated as

$$\delta_r = 0.6° \cdot \left(\frac{10^{20} eV}{E/Z} \right) \left(\frac{B_r}{4\mu G} \right) \sqrt{\frac{D}{4kpc}} \sqrt{\frac{L_c}{50pc}} \tag{2}$$

, where D is the distance from the Earth and L_c is the coherent length of random magnetic field and B_r is the random field strength.

The random component of the deflection angle of 40 EeV protons is estimated as 0.2-1.5°. Recently, the deflection angles of 40 EeV proton is anticipated to be about 3 degrees using the information of updated Faraday rotation measurement which is reported in Ref.[123].

2.2.4. Regular Galactic Magnetic Field

Faraday rotation of linearly polarized radiation from pulsars and from extragalactic radio sources (EGRs) is the most powerful probe of the diffuse magnetic fields in our Galaxy.

Faraday rotation measurement (RM) is given by $0.812 \int_0^{d[pc]} (B_{||}[\mu G])(n_e[cm^{-3}])dl$ (rad m^{-2}) where dl is the elemental vector and $B_{||}$ is the vector magnetic field along the line of sight toward us, and n_e is the free electron density and d is the distance.

Faraday rotation is the result of the integration of $n_e \mathbf{B} \cdot d\mathbf{l}$ along the line of sight, so we need the model of n_e and B structure to estimate $B_{\perp}$ component which is needed to calculate the deflection angle of UHECRs.

Despite the progress of several observations of Faraday rotation, there is no confirmed overall picture of the Galactic magnetic fields including its disk fields and halo fields.

The recent analysis of the RMs of EGRs around the disk of our Galaxy gave $11° \pm 2°$ pitch angle [80]. This looks a clear progress about the geometry of the Galactic magnetic fields in the disk. But the total picture of the Galactic magnetic fields in the disk may not be so clear. The magnetic field models which are shown in Fig.6 are typically considered. The detail of the formulation of the models is shown in Section.6.2. Strictly speaking, any single magnetic field models of the disk of our Galaxy is not enough to fit RM data [81].

The RM amplitudes of EGRs in the mid-latitudes of the inner Galaxy are systematically larger than that of pulsars, indicating that antisymmetric magnetic fields in the Galactic halo are extended towards the Galactic center, far beyond the pulsars [82]. Model fitting of RM amplitudes has confirmed this conclusion [83]. The toroidal type of the Galactic magnetic fields in the halo which is antisymmetric below and above the plane is needed to explain the RM amplitudes in the mid and high-latitudes. Fig.7 is the recently observed RM amplitueds [123] which show clear antisymmetric feature below and above the plane. The quantitative interpretation of the observed RM is explained in Section.6.2.

The local vertical field component Bz was suggested as about 0.2 μG in the solar vicinity in Ref.[84, 85]. On the other hand, the recent observations of RM amplitudes in the high-latitudes exhibit the different result to the south Galactic pole and to the north Galactic pole [86]. RMs of 0.0 ± 0.5 rad m^{-2} and 6.3 ± 0.7 rad m^{-2} toward the north and south Galactic poles indicates that there is no coherent vertical magnetic field in the Milky Way at the Sun's position.

The regular field strength of the Galactic magnetic fields at some points is measured in some accuracy. The measurement of the regular field strength

16

in solar vicinity gave 1.5 ± 0.4 μG [87], and 4.4 ± 0.9 μG near the Norman arm [88].
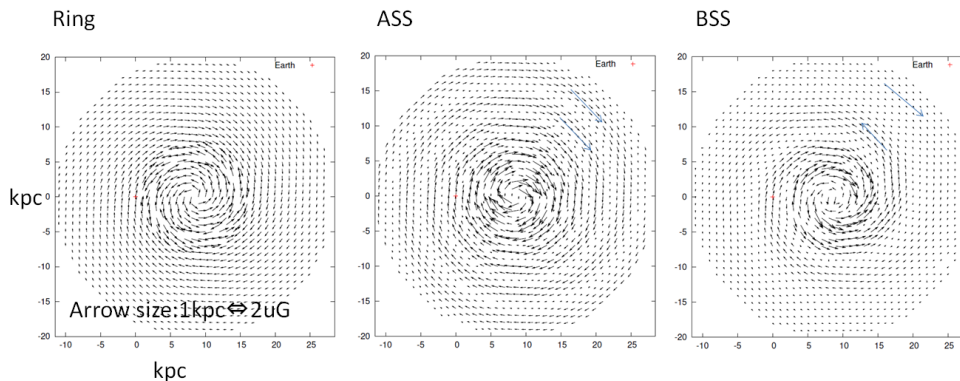

Figure 6: Examples of the models of the regular GMF are shown in this figure. The arrow size of 1 kpc corresponds to the 2 uG field strength. The left figure is an example of the ring model which is shown in Ref.[83]. The center figure is an example of ASS model which is shown in Ref.[121]. The right figure is an example of BSS model which is shown in Ref.[83].

2.3. Air Shower Generation and Observation Methods

- Air Shower Generation

The differential energy flux of cosmic rays decreases following power law whose index is about -3 as shown in Fig.2, indicating that the statistics of higher energy decreases drastically. So the statistics of UHECRs is very small, and this makes the observation difficult. For direct measurement of cosmic rays at the top of atmosphere, a 2 m^2·str aperture detector which observes for 100 hours is expected to observe about 50 cosmic rays above 100 TeV as an example [89]. This means that this observation is expected to observe about only $5 \cdot 10^{-7}$ cosmic rays above 10^{18} eV. It is not realistic to construct a big chamber which covers more than km^2 at the top of atmosphere. So the indirect measurement using extensive air shower is the main method for the observation of UHECRs.

When UHECRs survive even after the propagation described in the previous section, UHECRs arrive at the Earth. When such high energy charged particles collide with particles in the atmosphere on the Earth,
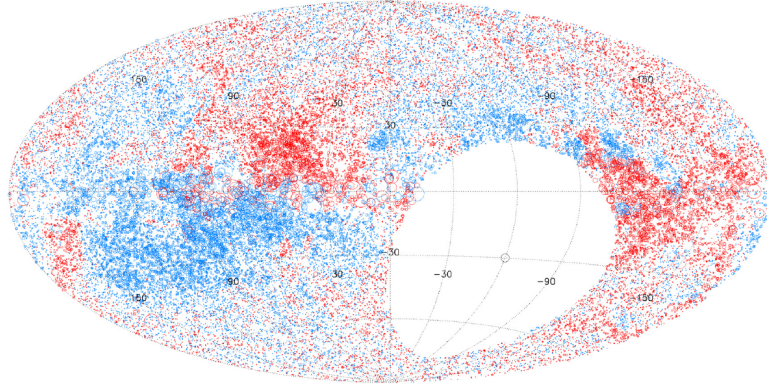
Figure 7: Observed RM values by NVSS. Red circles are positive and blue circles are negative RM values. The size of the circle is linear with magnitude of RM. [123]

the collision generates a lot of secondary particles. This phenomenon is recognized as an air shower. The schematic view of the development of an air shower is shown in Fig.9.

The hadronic interaction which is induced by an UHECR generates many energetic secondary pions and these pions decay and generate electro-magnetic showers. The leading process of π^0 decay is $\pi^0 \to 2\gamma$ and the secondary gamma rays create electron-positron pairs. The leading process of secondary electrons is the bremsstrahlung when the energy of electrons is above the critical energy which is about 88 MeV under 1 atm condition. The leading process of $\pi^\pm$ is $\pi^\pm \to \mu^\pm + \nu_\mu$ and the secondary muons decay into electrons.

1 particle generate 2 particles in the both processes of the electron-positron pair creation and the bremsstrahlung and these processes increase the number of secondary particles logarithmically. This is the main component of the extensive air shower development.

- Particle Detection using Ground Based Array

The ground based particle detector for UHECRs which consists of plastic scintillators is used in AGASA. This type of detectors detects the scintillation light emitted in the plastic scintillators using PMTs. The scintillation light is known to be proportional to the energy deposition of charged particles passing through them. The ground based particle detector which consists of water tanks is used in Pierre Auger, and
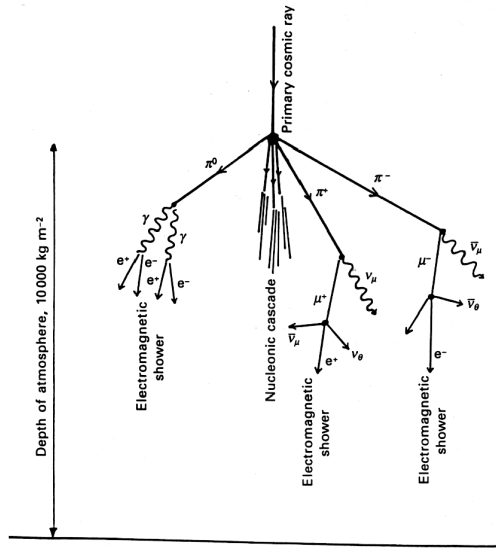
18

Figure 8: The schematic view of the development of an extensive air shower. [90]

Haverah Park. This type of detectors detects the Cherenkov light emitted in the water tanks using PMTs. The Cherenkov light is emitted in the tracks of relativistic particles in the detector. These detectors can monitor energetic secondary particles in the air shower in their way.

The geometry of the ground based array is designed to cover the large air shower geometry induced by UHECRs and to archive enough large statistics. The schematic view of the arrival timing distribution in the air shower is described in Fig.9. The timing distribution of the arrival secondary particles is important to determine the geometry of the air shower. So the high speed devices like plastic scintillators and PMTs which have several ns decay time are usually selected and enough small spacings of the array are designed. Recently FADCs are instrumented in data acquisition devices and the timing distribution of the output of PMTs is directly recorded in TA and Pierre Auger. The determination of the geometry of the air shower is directly related to that of the arrival directions of UHECRs.

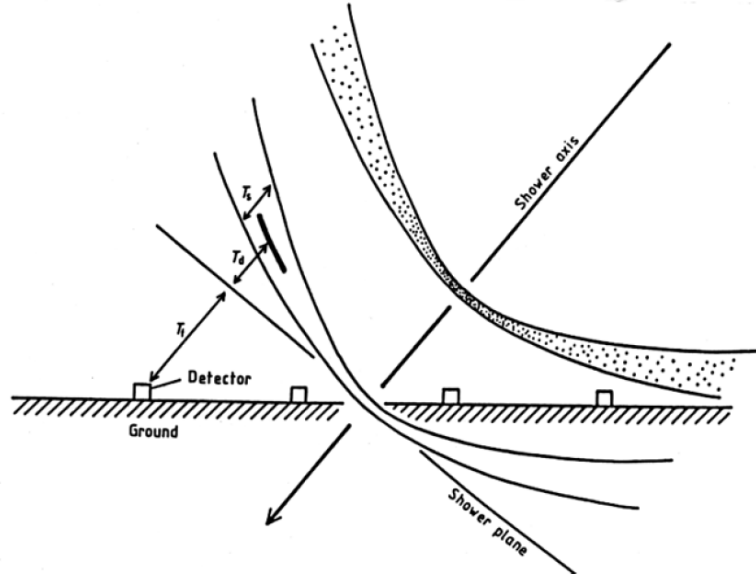The secondary particles spatially spread wider in the lateral direction

Figure 9: The schematic view of the ground based array observing an extensive air shower. T_f is the propagation time of the tangential plane of the shower front on the array which is called as shower front. T_d is the average time delay of the secondary particles in the air shower. T_s is the thickness of the shower front. [91]

depending on the development of the air shower. The lateral distribution of secondary electrons depending on the development is approximately given in the formula

$$\rho_e = N_e C(s, r_m) \left(\frac{r}{r_m}\right)^{s-2} \left(1 + \frac{r}{r_m}\right)^{s-4.5} \tag{3}$$

and

$$C(s, r_m) = \frac{\Gamma(4.5 - s)}{2\pi r_m^2 \Gamma(s)\Gamma(4.5 - 2s)}, \tag{4}$$

where r is the lateral distance, ρ_e is the number density of electrons, N_e is the total number of electrons, r_m is the Moliere radius which represents the Coulomb scattering of low energy electrons and s is the age parameter which increases as the air shower develops and reaches 1 at the maximum development. This formula is obtained using some approximations which is called as B approximation for an infinitely

large primary energy, and this is known as Nishimura-Kamata-Greisen (NKG) function.

The actual detector response happens in more complicated situation. The modified lateral distribution function is set to adjust each experiment.

The information of the lateral distribution includes the total number of electrons on the ground. The total number of electrons is known as a parameter which is approximately proportional to the primary energy. It is impossible to measure directly the total number of charged particles with sparse ground array so practically S(600) which means the signal 600m distant from the core position is used as an energy estimator in AGASA and S(1000) which is 1000m distant from the core is used in Pierre Auger as an energy calibration parameter. This S parameter is usually reconstructed using modified NKG function and there is also a mention that the systematics and the fluctuations of the energy depositions are at minimum at certain hundreds of meters from the shower core [92, 93].

An extensive air shower simulations need to evaluate S parameter corresponding to the certain primary energy, because there is no calibration sources for now other than air showers which are detected by the fluorescence detectors. So the ambiguity of hadron interaction models and the composition of UHECRs in the simulation becomes the systematic error of the energy determination in this method. This is the main systematic error of the energy determination of this method. This systematic error is estimated about 12 % in AGASA.

The large number of secondary particles enables the sparse spacing and the large coverage of the ground array. The recent large ground array for UHECRs cover more than hundreds of km^2, which results in the observation of more than several hundreds of particles per 100 hours which is more than 1 EeV. In addition to that, this detection method does not much depend on the ambiguity of the atmosphere on the Earth because this detection method observes only the energetic particles. So we can observe at the daytime and the night uniformly without much calibration of the atmosphere, which enables simple anisotropy analysis of the arrival directions of UHECRs.

- Fluorescence Detection

When the secondary charged particles go through 1 g/cm^2 atmosphere, those particles lose about 2.2 MeV of their energy [94]. In the process the secondary charged particles in the air shower excite and ionize mainly nitrogen in the atmosphere, and the nitrogen emits photons which have ultra violet wavelength as air fluorescence light. So the total photons of the air fluorescence at one depth of the atmosphere is approximately proportional to the total number of charged particles in the air shower. The technique of the fluorescence detection makes use of this phenomenon.

Fluorescence detectors observe the air fluorescence light induced by the extensive air shower using telescopes. So the detectors can measure the total number of charged particles depending on the atmospheric depth. The fluorescence detectors are instrumented in the observatories of Pierre Auger, HiRes, Fly's Eyes.

The fluorescence detectors can directly observe the longitudinal development of air showers other than ground array. The longitudinal development of the air shower includes the important information of the composition and the energy of primary UHECRs.

The first interaction points of the UHE heavy nuclei are expected to be higher than the light nuclei and the fluctuation of the points is expected to be smaller because heavy nuclei consist of many light nuclei. The Xmax means the atmospheric depth when the number of charged particles is at the maximum in the air shower. This observable reflects the feature of the first interaction point and the ambiguity of this observable is rather small because there are much number of charged particles at the depth. So the Xmax is known as an important observable for the determination of the composition of UHECRs.

If we multiply the integration of the observed longitudinal development of charged particles by the energy loss rate 2.2 MeV per g/cm^2, we can roughly calculate the primary energy. More correctly, muons do not lose their all energy in the atmosphere and hit the ground with about 10 GeV, so the observed total energy misses this kind of escaped charged particles and neutrinos and the simulation of the missing energy is needed to be calculated. The missing energy is estimated to be about 5 % for protons and 15 % for irons.

The longitudinal development of charged particles are estimated from

the observed photons and from the distance from the location of the telescopes and from the florescence yield which is measured in several laboratories, so the atmospheric transparency and the scattering feature of the photons should be precisely calibrated in this method. This systematic error of the calibration is the main source of the systematic error of the energy.

2.4. Observed Energy Spectrum, Composition and Arrival Directions

There are several observations of UHECRs and results, here we review the results.

- Energy Spectrum

  The compilation of the observed energy spectra is shown in Fig.10. Energy spectra of UHECRs measured by Akeno, AGASA [95], Fly's Eye [96], HiRes, Pierre Auger [97] and Yakutsk [98] experiments shown in this figure. In this figure, those results are overlaid with preliminary TA results (FD, SD and Hybrid). The HiRes, Auger and preliminary TA SD experiment clearly show the flux suppression.

  The measured spectra by the different experiments are in good agreement after energy shift at the dip, which is a feature predicted by electron-positron pair production in collisions of protons with CMB photons [6]. This energy shift is carried out in Fig.11. In this figure, TA and HiRes results are not scaled at all because the dip energy scale and the flux suppression energy scale at the high energy end agree the prediction by the pure proton model.

  The difference of the energy scale between experiments is an issue especially for anisotropy analysis. For example, 20 % shift of the energy scale cause about 2 times larger/smaller statistics over a certain energy threshold under E^{-3} energy spectrum. This difference makes the simple compilation of observed UHECRs in different experiments difficult. If the systematic error of the energy does not much depend on the energy as suggested by Ref.[6], the simple multiply of the discrepancy of the energy scale enables the compilation of the UHECRs observed in different experiments, but it needs a great care about the energy dependence of the systematic error of the energy determination.
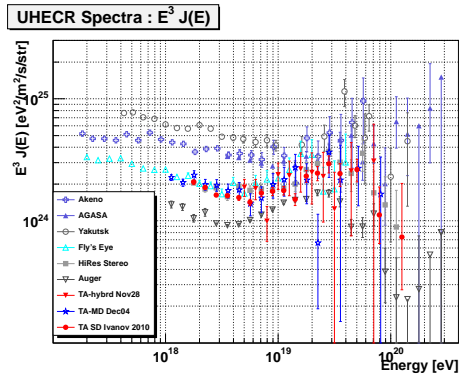
- Composition
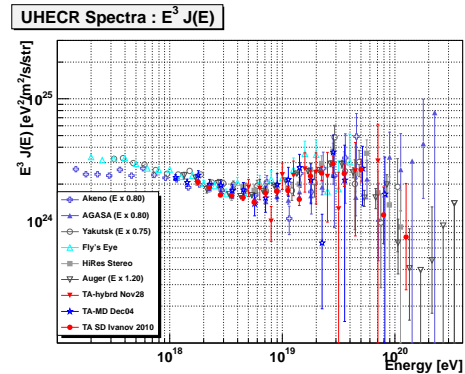
23

Figure 10: The compilation of observed energy spectra.

Figure 11: The compilation of scaled observed energy spectra.

The results of the observed Xmax is shown in Fig.12, 13 and 14.

In Fig.12, the average and dispersion of Xmax distribution observed in Pierre Auger are drawn. We can see in this figure that Xmax distribution significantly deviate from the expectation of proton models.

In Fig.13, the average and dispersion of Xmax distribution observed in HiRes are shown. We can see in this figure that the Xmax distribution is in good agreement with pure proton QGSjet models from the both points of the average and the dispersion in this experiment.

In Fig.14, the preliminary results of the average values of Xmax distribution observed in TA are drawn. We can see in this figure that the average of the Xmax distribution is in good agreement with pure proton QGSjet models.

In Fig.15, the preliminary results of the compatibilities between the Xmax distribution observed in TA and several models using Kolmogorov-Smirnov (KS) test are shown. We can see in this figure that the shape of the Xmax distribution is in good agreement with pure proton QGSjet models. On the contrary, pure iron model is rejected in $10^{18.4-19.4}$ eV energy range in much more than 99.7 % confidence level.

Interpretation of these results is not so easy. The composition of the observed UHECRs is expected to be purely proton in TA and HiRes because of no significant feature of the deviation from the both points of the average and the dispersion of Xmax distribution. These results

24

may contradict the results in Pierre Auger. This discrepancy may be because of the different observation techniques or the different analysis methods or the difference of the location of the observatory (northern hemisphere and southern hemisphere. We do not have the answer yet anyway.
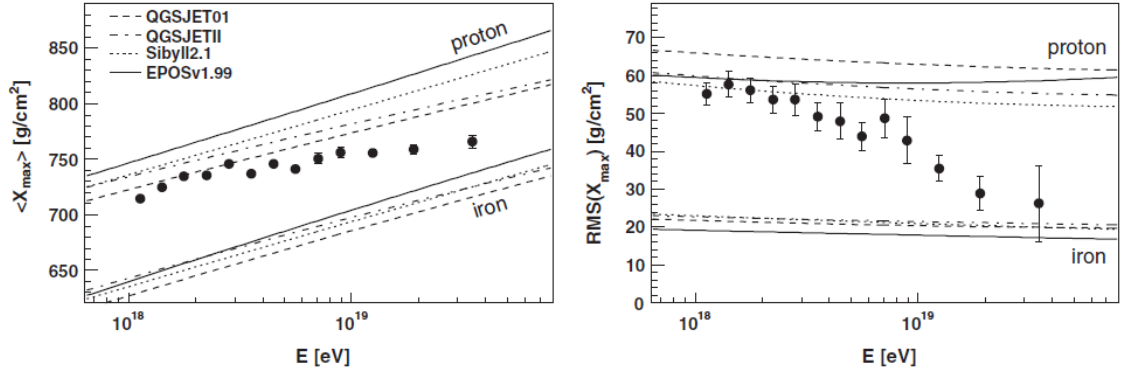

Figure 12: Left: Observed average Xmax distribution in Pierre Auger. Right: Observed root mean square of the Xmax distribution in Pierre Auger. [10]

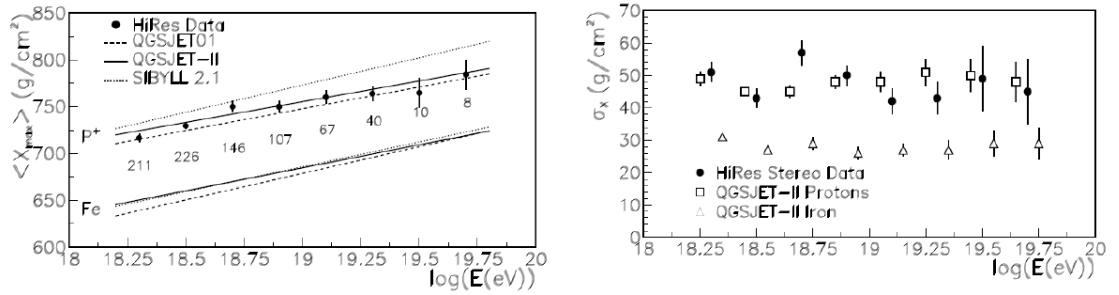
Figure 13: Left: Observed average Xmax distribution in HiRes stereo data. Right: Observed sigma of the Xmax distribution using HiRes stereo data. [11]
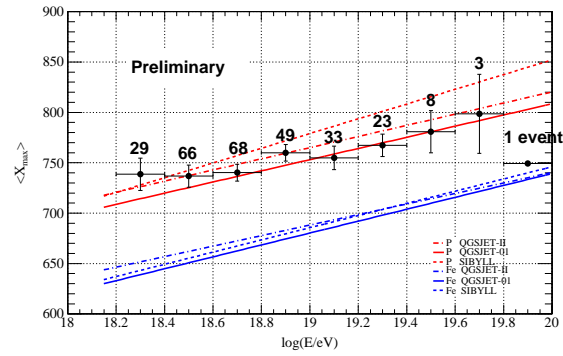
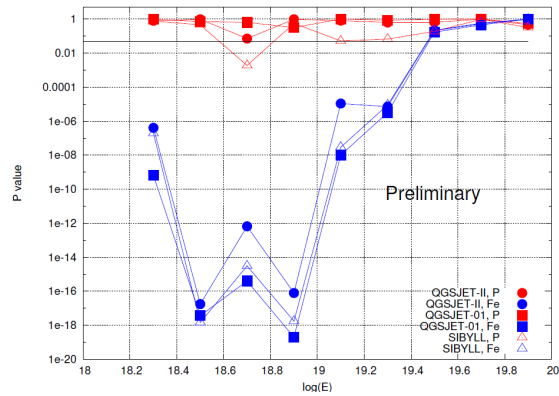Figure 14: The preliminary observed average Xmax distribution using TA stereo data. [12]

Figure 15: The Kolmogorov-Smirnov (KS) test is carried out for Xmax distribution between the TA stereo data and several models and the compatibility is drawn in this figure. [12]

- Arrival Directions

  Arrival directions published by AGASA, Auger and HiRes are shown in Fig.16, 17 and 18.

  The observed 58 arrival directions of UHECRs above 40 EeV in AGASA is shown in Fig.16. Doublets and triplets found by AGASA is shaded circles in this figure. These clusters seem to distribute all over the exposure and suggest the extra Galactic sources of UHECRs.
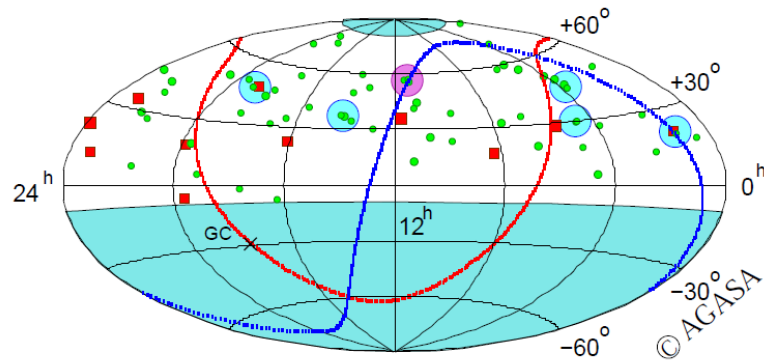

  Figure 16: The observed arrival direction distribution in AGASA taken from [99] The skymap in equatorial coordinate of arrival directions of cosmic rays with energies above 40 EeV observed between 1990 and 2002. This skymap uses Hammer projection. Events with energies above 100 EeV are shown in red. Clusters are indicated as shaded 2.5° circles. Blue circles are for doublets and pink circles are for triplets. The galactic plane is red line, and the super-galactic plane is blue line in this map.

  The observed 69 arrival directions of UHECRs above 55 EeV (originally 57 EeV but a bit changed later) in Pierre Auger is shown in Fig.17. Tested directions of AGNs from VCV catalogue are also shown as blue circles in this figure. The cross correlation between the arrival directions of UHECRs and AGNs deviate from isotropy in 99.7 % confidence level. There may be the feature of the concentration of the arrival directions around the Centaurus A (Cen A) in larger angular scale from Fig.17. The largest deviation of number of events around Cen A from the isotropic expectation reaches more than 3 σ with 18 degrees angular scale, but the deviation is not significant if the selection bias of the angular scale is taken into account.
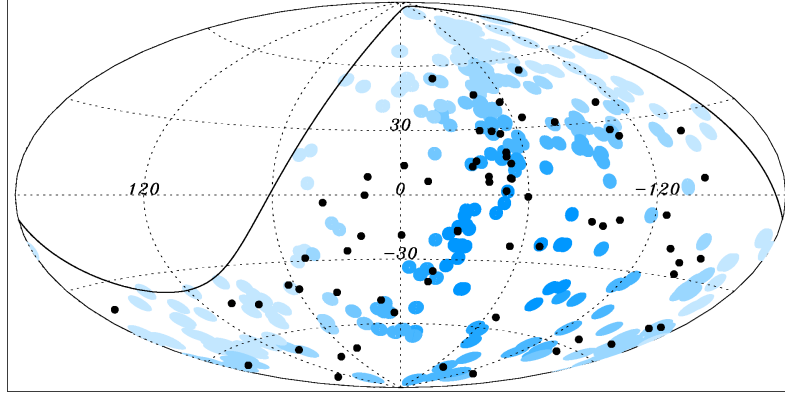
Figure 17: The observed arrival direction distribution in Pierre Auger. This skymap is drawn using Hammer projection in galactic coordinate. Blue shaded circles of 3.1° radius are centered at the 318 AGNs in VCV catalog within 75 Mpc in Pierre Auger field of view. Darker blue indicates larger relative exposure. [19]

The observed 309, 27, and 10 arrival directions of UHECRs used for the LSS analysis above 10, 40, and 57 EeV in HiRes is shown in Fig.18. These events are cut under $|b| < 10°$ because of lacking of the coverage of 2MRS catalog. Arrival directions of UHECRs are completely separated and it is clear that there is no cluster especially in the middle and bottom figure in Fig.18. In addition to that, we cannot see any events in the darkest color in the bottom figure. This means the rather strong rejection of LSS model even with such small amount of data. HiRes reported the disagreement with LSS which is constructed using 2MRS catalogue within the angular scale of 10 degrees above 40 EeV and 57 EeV with more than 95 % confidence level [29]. This result may be rather serious issue for the anisotropy search.
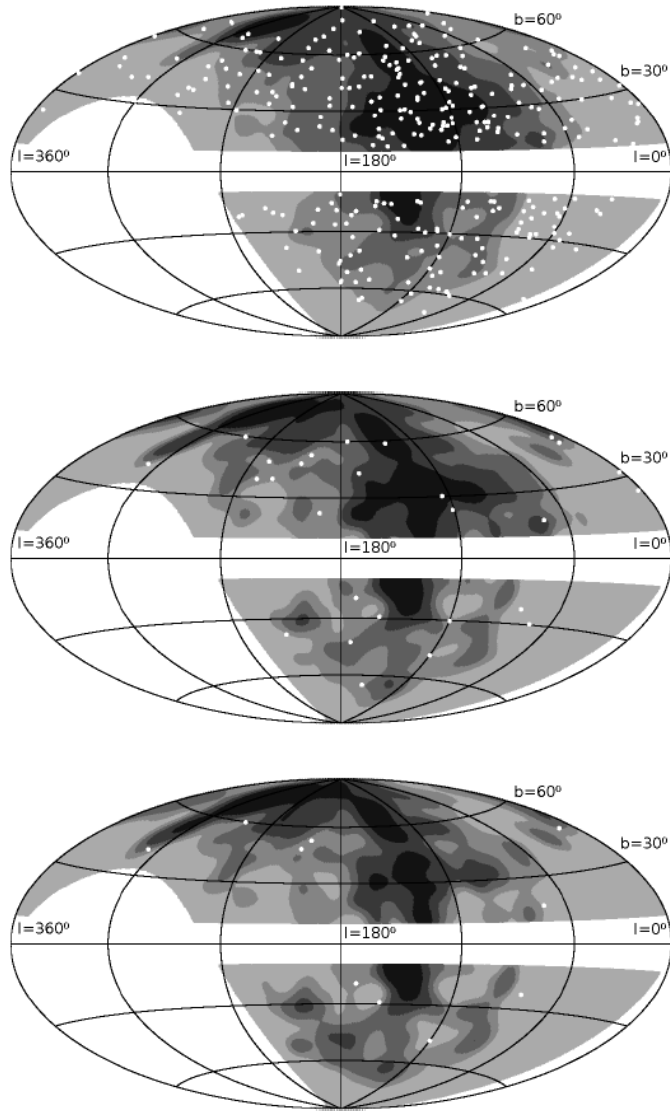
Figure 18: The observed arrival direction distribution in HiRes [29]. This skymap is drawn using Hammer projection in galactic coordinate. White dots indicate HiRes events and the contour indicate expected flux weighted with exposure with threshold energies 10 EeV(top), 40 EeV(middle), and 57 EeV(bottom). Darker gray indicates higher value and each band contains 1/5 of the total flux weighted with exposure. And All maps are made by using 6 degree smearing angles.

3. TA Detector

The site of the Telescope Array experiment is located in the desert of Utah in USA, about 200 km southwest of Salt Lake City. The center of the array where CLF is built is located at 39.3° Latitude, -112.9° Longitude, and is 1382 m above sea level. The Telescope Array experiment is the largest hybrid detector in the northern hemisphere, which consists of 2 types of detector: SD array and FDs. The SD array consists of 507 SDs which consists of 2 layers of 3 m^2 plastic scintillators are deployed in a square grid with 1.2 km spacing, covering about 700 km^2. SD array is surrounded by 3 FD stations which are on the corners of an about 30 km triangle. Since this experiment requires large acceptance, long distance radio network system was developed for the facilities in the TA site. The system consists of 3 communication towers and 5 sites (3 FD stations, CLF, and Cosmic Ray Center in Delta City). There are 3 SD DAQ sub-arrays with which SD host electronics communicate from each communication tower called as Black Rock Mesa (BRM), Long Ridge (LR) and Smelter Knolls (SK) sub-arrays. 3 FD stations are called as BRM, LR, and Middle Drum (MD) Station. Those are connected with 2.4 GHz and 5.7 GHz wireless LAN [100]. The Telescope Array underwent commissioning in 2007 and started routine data collection operations in March 2008. The experiment is being performed by a collaboration of about 120 members from about 25 institutions in 4 countries (Japan, United States, South Korea, and Russia). Fig.19 shows the layout of the Telescope Array.

3.1. Surface Particle Detector

Each SD has 2 layers of 1.2 cm thick scintillators. The scintillation light is gathered by wavelength shifting (WLS) fibers and brought out to a PMT for each layer. The SD electronics consists of 2 channels of 12-bit FADCs with 50 MHz sampling, FPGA for fast signal processing, CPU for slow signal processing, CPLD for board control, 1 charge controller, ADCs for monitoring, and DACs for setting high voltage of PMTs. Power for the PMTs and electronics is supplied by solar power system, and communication with the SD host electronics at the communication tower is performed with a wireless LAN modem board using 2.4 GHz spread spectrum technology. Fig.20 shows a SD in the field. Fig.21 and Fig.22 show the configuration of a scintillator box in which plastic scintillators are.

When signals from 2 PMTs of the SD exceed 0.3 single muon peak, level-0 trigger is generated and the waveform is stored locally in a memory with a
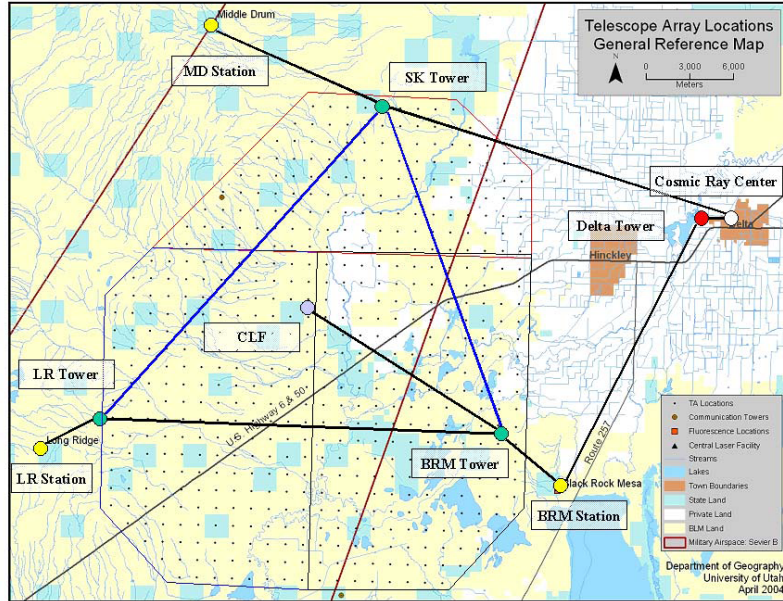
Figure 19: The layout of the Telescope array. The dots represent the positions of SDs. 3 communication towers marked as BRM, LR and SK Tower are located near the edge of the SD array. The SD DAQ sub-arrays called as BRM, LR and SK sub-arrays are located in the southeast, southwest, and north respectively. 3 FD stations are marked as BRM, LR, and MD Station.

time stamp by a GPS. When both PMT signals exceed a trigger threshold of 3 muon peaks, the trigger timing information is locally stored in a list (level-1 trigger). The trigger timing of level-1 trigger is transmitted with the data for monitoring to the SD host electronics every second. The timing of level-1 trigger is checked by the SD host electronics and data taking of wave forms is started if there are at least 3 adjacent counters within 8 μs time window (level-2 trigger). TA SD array started full operation in March 2008. Since May of 2008, the fraction of running time is more than 97 % and the fraction of good SDs which are used for the analysis is more than 98 %. The detailed performance is shown in Section.5.

Since 3 DAQ sub-arrays were operated independently at first, there was inefficiency of shower triggers around the boundaries of neighboring shower triggers around the boundaries of neighboring sub-arrays. We installed cross-boundary trigger to improve and make the shower efficiency uniform inside the array region in November 2008 [101].

The local SDs send monitor data to SD host electronics every second with level-1 trigger information. This monitor data which is locally accumulated enables us real-time calibration and monitoring. The monitor data includes level-1 trigger rate, GPS time stamps, and clock counts between 1 pps as every second data, and includes level-0 trigger rate, battery voltage and battery charging current as every minute data, and includes charge histogram, pulse height histogram, pedestal histogram, and GPS condition information as every 10 minutes data. Fig.23 shows charge histograms for one SD. This charge histogram including all charge information enables precise SD calibration which is shown in Section.5.

Figure 20: A SD in the field. There is a scintillator box under the roof to avoid the overheat caused by the sunshine. In a scintillator box, there are 2 layers of plastic scintillators. A SD electronics and a battery box are on the back of a solar panel. The height of an antenna pole is about 3m and the direction of the antenna is carefully adjusted for good communication with the communication tower.
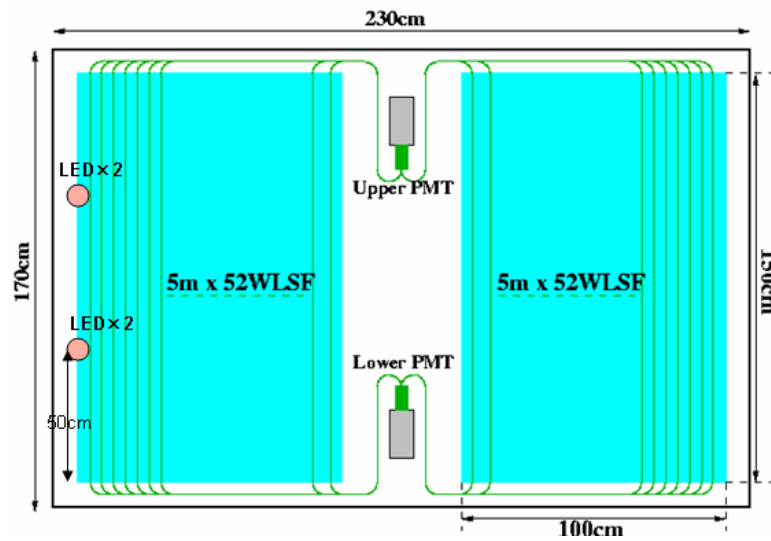

Figure 21: The configuration of a scintillator box of a SD. The size of the box is 230cm × 170cm × 10cm. The box is made of 1.2, 1.5mm thick stainless steel. The weight of this box is about 190kg. The blue color corresponds to the area of plastic scintillators. 1 layer consists of 8 150cm × 25cm × 1.2cm size of plastic scintillators. 4 scintillators are to the left and the right respectively. Green lines correspond to WLS fibers. Since 13 WLS fibers are on each plastic scintillator, PMT reads out the light from the both edge of the 104 WLS fibers.
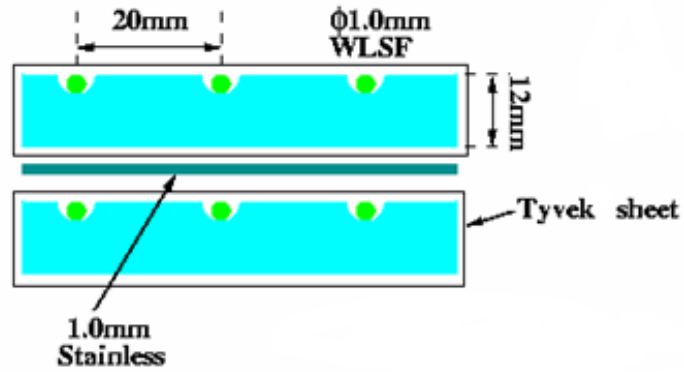
Figure 22: The vertical section in the SD scintillator box. The blue box corresponds to plastic scintillators. 4 plastic scintillators are covered with 2 sheets of tyvec sheet. There is a 1mm thick stainless steel between the 2 layers.
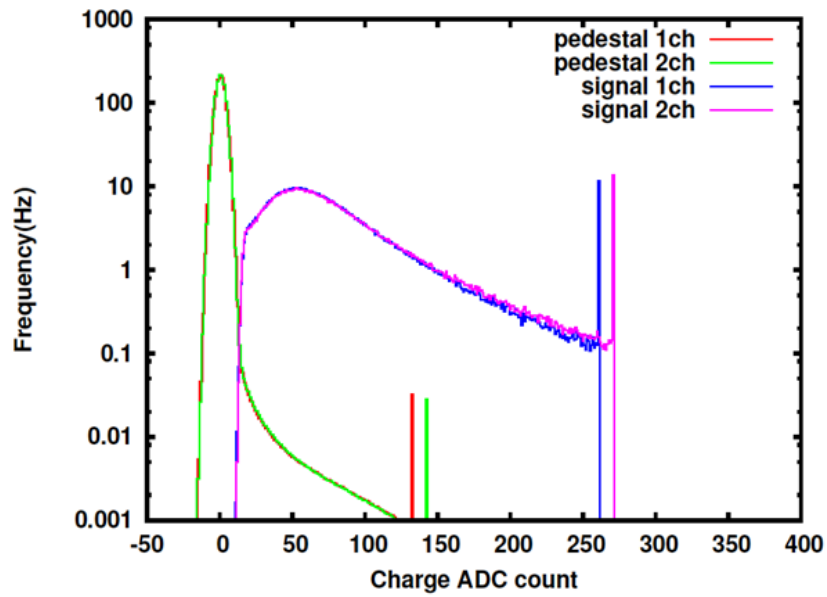

Figure 23: An example of charge histograms collected in a local SD. The peak of pedestal FADC distributions are adjusted to 0 count.

3.2. Fluorescence Detector

The array of SDs is surrounded by 3 FD stations. MD station is to the northeast. BRM station is to the southeast, and LR station is to the southwest respectively. Fig.24 are the pictures of the BRM and the MD FD stations.

The MD site is instrumented with 14 telescopes from the HiRes-I site The cameras each contain 256 hexagonal Photonis PMTs in 16×16 array. Each PMT views about $1°$ of sky. The telescopes are arranged in a "two ring" geometry with the first ring viewing from 3-17° and the second ring viewing from 17-31° from the horizon. The seven pairs of telescopes view 114° in azimuth. They have $2m \times 2m$ mirrors which have 3.75 m^2 of effective area and are with electronics which they had for the HiRes experiment. This site provides a direct link back to the HiRes analysis.

The MD FD site started standard data collection in November 2007. A duty cycle of the observation in this station is better than 10 %.

Each camera is calibrated nightly via a temperature stabilized UV LED. The 14 telescopes are housed in a concave building and are arranged so that they all overlook a common point at the focus of the building. The relative calibration of all of the telescopes at the site can be compared since they all overlook a vertical beam from a single xenon flush lamp. In addition to that, a Roving Xenon Flasher (RXF) is used to illuminate all cameras with the stability of better than 2 %. There are also instruments of microwave sensors with 30° field of view which measure the sky temperature to search for clouds.

There are 12 new telescopes are in the BRM and LR stations. The cameras of the telescopes consists of Hamamatsu PMT with 1° field of view. These sites also use a "two ring" geometry like MC station and have a field of view which is 3-33° above horizon and 108° in azimuth. The telescopes consist of 3m diameter, hexagonal mirror and the cameras are read out by new FD electronics. The data is sampled at 40 MHz, and 4 bins are summed so that 10 MHz samples are stored as described in [102].

Data collection is started in the BRM FD site and partially in the LR FD site in June 2007. Duty cycle of observation in these sites is about 10 %. The relative gain of PMTs is calibrated via built-in xenon flashers every night.

LIDAR (LIght Detection And Ranging) system is located in a rotating dome 100m to the side of the BRM station. A 4 mJ, energy tripled (355 nm

wavelength) Nd:YAG laser is mounted in the system. The receiver is a 10 inch Meade telescope with a PMT at its focal point [103].

An Infra-Red (IR) camera mounted next to the LIDAR system to monitor clouds [104]. The camera has a field of view of 26° × 20° which is slightly larger than the field of view of a fluorescence telescope and takes photos of 320 × 236 pixels. IR camera takes 12 pictures covering the entire Telescope Array every hour.

A CLF is at the center of the 3 FD stations. The CLF also uses an energy tripled YAG to fire a beam of 355 nm light into the sky [103]. The laser fires every half hour at a variety of energies. This allows one to measure the atmospheric transmission parameters (VAOD and horizontal extinction length) as well as to directly compare the reconstruction of the 3 FD sites.

We built an electron linear accelerator ELS to perform an end-to-end absolute energy calibration of the fluorescence telescopes including everything from the air fluorescence spectrum through the telescope optics and electronics. The maximum output beam energy is 40 MeV and the charge of 1 pulse is 10^{19} electrons. Typical pulse width is 1 μs and the repetition is about 0.5 Hz. An electron beam with the maximum total energy of 4×10^{16} eV, which is injected vertically into the air, generates air shower and fluorescence light is emitted. The absolute calibration is performed by the comparison of reconstructed energy and estimated energy by simulation. The ELS was installed 100m forward from the BRM FD station in March 2009. The status of the ELS is described in [105].

Figure 24: The BRM FD station (left top) and mirrors (right). The MD FD station and mirrors (left bottom).

4. Monte Carlo Simulation

The energy deposition in the SD is caused not only by the charged particles but also by the neutral components such as much abundant soft gamma rays and delayed neutrons produced in the air shower. In order for the air shower Monte Carlo (MC) to reproduce the SD energy depositions properly, effects of all the particles will have to be taken into account. A thin sampling method creates air shower events in a short time but it reproduces the SD energy deposition only in a statistical manner when many events are accumulated. A full simulation reproduces the proper energy deposition event by event, but the calculation time is prohibitive for sufficient numbers of events to be simulated. More concretely, a full simulation needs about one week/cpu for 10^{17} eV proton, about 2 years/cpu for 10^{19} eV proton and about 20 years/cpu for 10^{20} eV proton.

Several methods have been tried to comprise these 2 factors which are critical for SD simulation. De-thinning is the way to generate particles which have randomized momentums and arrival timings assuming virtual trajectories from the thinned particles. We developed a hybrid method using both full simulation data and thin sampled simulation results shown in 4.1. And an ensemble thinning method which was used in 4.1 was customized and applied to the air shower generations. And this is shown in 4.2.

4.1. TAMCDB

We developed a hybrid method to create a full spectrum of particles incident on the SD in a limited time based on the scaling features of air shower with the shower age and the Moliere unit (mu). It is based on a fast generation of thinned event and "wearing" it with a particle spectrum obtained from a pre-generated fully simulated event.

We produced more than 100 fully simulated events using parallel computing COSMOS using a PC cluster [106]. Up to 10^{19} eV, they are produced by the full simulation and a quasi full method with an approximation is used above 10^{19} eV [107]. A large amount of information (particle types, momentum vectors, timing etc.) are stored as the FDD (Four dimensional Development Data) data base at each stage of the shower development.

In the thin sampling method, integral quantities such as the total number of particles, lateral and arrival time distributions at a given depth are well reproduced if the appropriate thinning parameters are used. We produced 100 to 1000 shower events with thinning for a fixed set of parameters: the energy,

the zenith angle, the primary particle species and the hadronization model. The results are stored as the LDD (Longitudinal and Lateral Development Data) database. The major components of LDD are the total number of particles, lateral and arrival time distribution for each particle species.

In our method, a "full" simulation results are obtained in a short time by combining the LDD and FDD databases. It is predicted that shower parameters scale with the shower age in the longitudinal development and with the Moliere unit in the lateral development. It has been shown that in case of photons and electrons, good scaling parameters are the shower age and the Moliere length, and in case of muons and hadrons, the parameter cog (averaged depth of electrons) and the Moliere length are good parameters [108]. By taking the advantage of scaling, we can associate each part of the LDD event with the corresponding part of the FDD event with the same shower age/cog and the core distance measured in the unit of Moliere length. In this way, a single FDD event can be recursively used by many LDD events. The distribution also scales with the primary energy, and the LDD can be associated with the FDD at the different primary energy if properly scaled.

In this method, a fixed set of parameters of the energy, the zenith angle, the primary particle species and the hadronization model is needed to apply FDD data to LDDs. This fixed parameters make it difficult to use in more general purposes. We cannot easily apply this method to generate air showers whose primary particles follow continuous energy spectrum and zenith angle distribution as in nature for example.

4.2. Spectrum Set

Stimulated by a quasi full method which is used to make COSMOS FDD, the method to use an ensemble thinning were developed.

In making COSMOS FDD, the current method memorizes all the particles below preset E_{min} generated at various depths. If a particle has energy larger than E_{min} at generation, we follow its cascading until every energy becomes lower than E_{min}. We also have to memorize particles of energy larger than E_{min}, if they cross an observation level. Air shower induced by the memorized particles are divided into pieces and are distributed to many cpus and are followed with lower energy. These pieces are adjusted so that the total energy and the number of particles are identical. This identity enables to distribute pieces to CPUs equally. After the calculation in each CPU, the results are unified to the extensive air shower. This method is called as "skeleton-flesh" method and is implemented in COSMOS as a basic parallel-computing

program. Skeleton means the memorized particles and skeletons are divided into sub-skeletons and distributed to CPUs. Fleshing means the particle generation process in each CPU. In a quasi full method, sub-skeletons which have identical feature are randomly sampled and calculated.

The process to generate spectrum set of air shower is following. Firstly, E_{th} is set and 1000 sub-skeletons are generated and 100 sub-skeletons are randomly sampled from them, and E_{th} is lowered to 0.1 E_{th}. This process is repeated for 4 times. And then the shower particles are followed until the energies are lower than 100 keV.

This process enables non-thinned simulations, but the total number of particles in the air shower has 10^4 weight and the process makes the sparser particle distribution than in the real shower. To compensate this sparse distribution, the size of SDs is enlarged and the particles which pass through the SDs are considered. When the size of SDs is enlarged, the timings of shower particles are corrected to the positions of SDs using the local interpolation in the air shower.

Using this procedure, air shower events are generated between 10^{18} and 10^{20} eV with 0.2 step in log, and between 0° and 60° zenith angle with 0.01 step in cosine with QGSJET-II. 100000 events are generated in each energy step below 10^{19} eV and 10000 events are generated in each energy step above 10^{19} eV. Number of events are distributed to follow $cos\theta$ (θ: zenith angle) in cosine step.

4.3. Detector Simulation

Detector simulation is constructed using GEANT4. The view of constructed detector is shown in Fig.25. The energy depositions of the plastic scintillator caused by air shower particles are calculated and converted to the FADC waveforms using approximated electronics response. The conversion factor from energy depositions to FADC counts can be got by 1 MIP calibration which is described in the next section. The simulated FADC waveforms are used to test the event reconstruction programs.
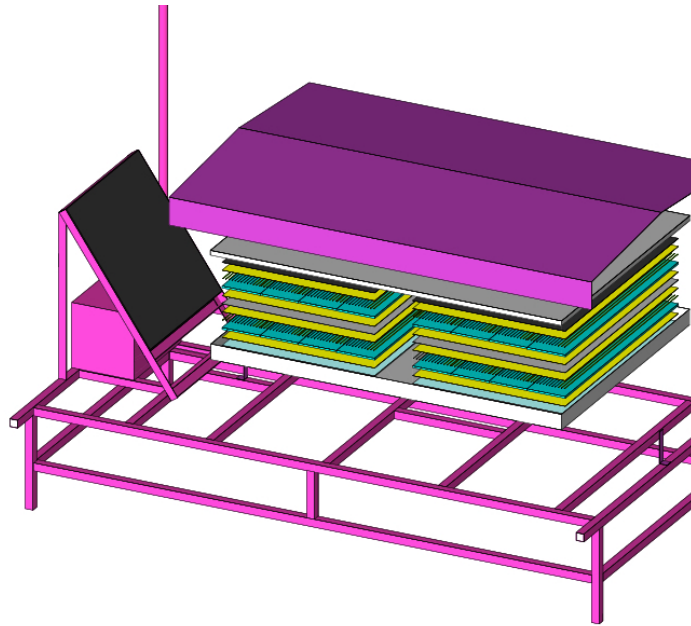
Figure 25: SD is constructed using GEANT4. Included items in SD are visible in this figure.

5. Data & Data Reduction

5.1. Data Set

Data collected from 11 May 2008 to 1 May 2011 is used in this analysis from the point of data quality.

5.2. Calibrations

The local SDs send monitor data to SD host electronics every second with level-1 trigger information. This monitor data which is locally accumulated enables us real-time calibration and monitoring. The monitor data includes level-1 trigger rate, GPS time stamps, and clock counts between 1 pps as every second data, and includes level-0 trigger rate, battery voltage and battery charging current as every minute data, and includes charge histogram, pulse height histogram, pedestal histogram, and GPS condition information as every 10 minutes data. These monitor data is used for calibrations and the health of the detectors.

- 1 MIP calibration

  The primary cosmic rays above several GeV mainly generate atmospheric energetic particles. At the ground level, typically several GeV atmospheric muons are dominant as secondary particles of cosmic rays.

  Relativistic charged particles like atmospheric muons lose their energy by ionizing and exciting atoms in the scintillator. The average energy loss of such a process is known to be given by the formula of Bethe-Bloch. According to the energy loss which is calculated using this formula, about 2 MeV/g/cm² energy loss of atmospheric muons which corresponds to the minimum energy loss of muons is expected in the plastic scintillators. This energy loss rate is not so much depending on the momentum of muons, so quite stable. And about 3 ns short decay time of the scintillation light in our plastic scintillators enables us to detect each muon, so the atmospheric muons are the powerful calibrators of the detector response of SD. This is the calibration method using minimum ionizing particles (MIP).

  We accumulate about 750 level-0 triggered events per second and draw charge histogram using them per 10 minutes. The time window for the integration to calculate a charge of a level-0 triggered event is 240 nsec. The shape of actually drawn charge histogram consists of energy loss

distribution and zenith angle distribution of atmospheric muons , the position dependence of the response of the SD, Poisson distribution of the number of photo-electrons generated at the surface of the PMT, and the distribution of the gain of the PMT and etc. The fluctuation of the number of photo-electrons generated at the surface of the PMT is a dominant factor in these components, but we should care about the asymmetric energy loss distribution and the zenith angle distribution.

Fig.26 shows a charge histogram for one SD together with MC simulation. In the MC simulation, detected particles are simulated using COSMOS air shower Monte Carlo from AMS energy spectrum and the detector simulation is carried out using GEANT4 as described in Section.4.3. In the simulation, the PMT gain, the scale factor and the number of photo electrons are set as fitting parameters. This fitting works well and the systematic error of the calculated energy loss is estimated to be 3 %.

Temperature coefficient of gains of TA SDs is about - 0.8 (%/°C) , and diurnal variation of temperature reaches up to 25 °C. So the monitor of charge histograms per 10 minutes also enables us to evaluate continuously the change of SD response due to the variation of temperature.

- Linearity

Linearity calibrations using LEDs and the pulse height histograms of the monitor data are used to check the linearity. These two calibrations are based on different methods. Firstly we show the LED calibration.

  – LED calibration

    A linear standard light source is needed to calibrate PMT linearity. A LED is a non-linear and temperature dependent device and its feature varies one by one, but luminosity of two LEDs is an exact summation of luminosity of each LED. So a comparison of the PMT response to light of two LEDs with the PMT response to light of each LED includes information about PMT linearity.
    When luminosity from LED1 is defined as x_1 and luminosity from LED2 is defined as x_2 and the PMT response function is defined as f(f:photon   output), PMT response relation can be described as
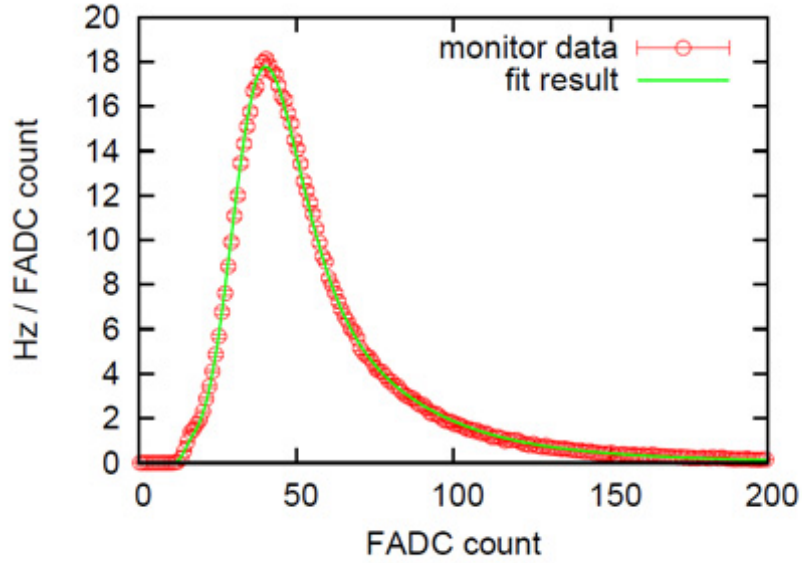
$$f(x_1 + x_2) = f(x_1) + f(x_2) \tag{5}$$

43

Figure 26: Measured charge histogram in the scintillator (open circles) together with expected MC simulation (solid line) for a scintillator layer of one of the SDs. Here we use COSMOS as air shower MC simulation and GEANT4 as detector MC simulation. The gain of this counter is estimated to be 17.4 FADC counts per MeV from MC simulation.

in linear region but when LED is more luminous, PMT response approaches saturation.

$$f(x_1 + x_2) < f(x_1) + f(x_2) \qquad (6)$$

By measuring the difference of PMT response, we can measure PMT linearity. This is the basic idea of this calibration.

We assembled two LEDs for one layer of plastic scintillators. Assembled LED position is shown in Figure.21.

Linearity calibrations using LEDs are carried out before the deployment of SDs. SD electronics can supply voltage to LEDs, so we use SD electronics for this calibration. In this calibration, we used 400 ns fixed width pulses to avoid the effect of cable crosstalk and switching noise which is showing up when the width is much narrower.

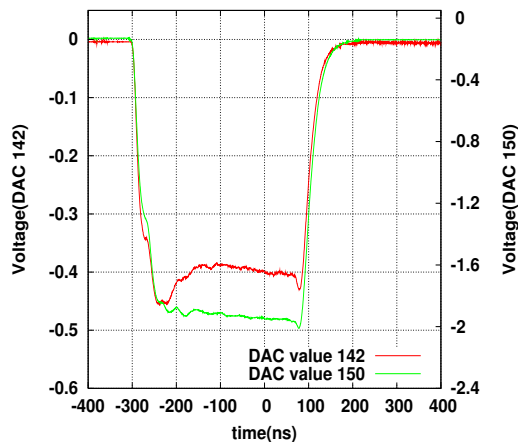When the PMT linearity is measured by 15 ns, 300 ns and 600 ns

Figure 27: PMT output voltage time distribution. LED input voltage is 2.77V and 3.13V and width is 400ns in this figure.

pulse width light, it was clear that the linear range is proportional to the pulse width. So the pulse height determines the PMT linear range and this is another reason why there is no problem with fixed width pulse.

The light pulse shapes which are observed by a PMT are showed in Figure.27. These pulses are used for the calibration.

We plotted typical PMT output ADC count at peak time bin of $f(x_1 + x_2)$ versus $f(x_1)+f(x_2)$ at the same time bin in Figure.28. In this measurement, we set $f(x_1) \approx f(x_2)$ to estimate linear range precisely, so $f(x_1)+f(x_2)$ ADC count includes non-linearity in about $(f(x_1) + f(x_2))/2$ ADC count region. We did the same measurement for all SDs.

The PMT linearity depends on its supplied voltage. We measured the linearity of 10 PMTs by using this method changing its supplied voltage, and the characteristic voltage dependence is found. $V^{1.5}$ dependence applied data is showed in the right figure of Figure.29. This supplied voltage dependence seems good to explain the data of 10 PMTs and the deviation from the estimated -5 percent non-linear point is less than 5% when HV difference is less than 200V.

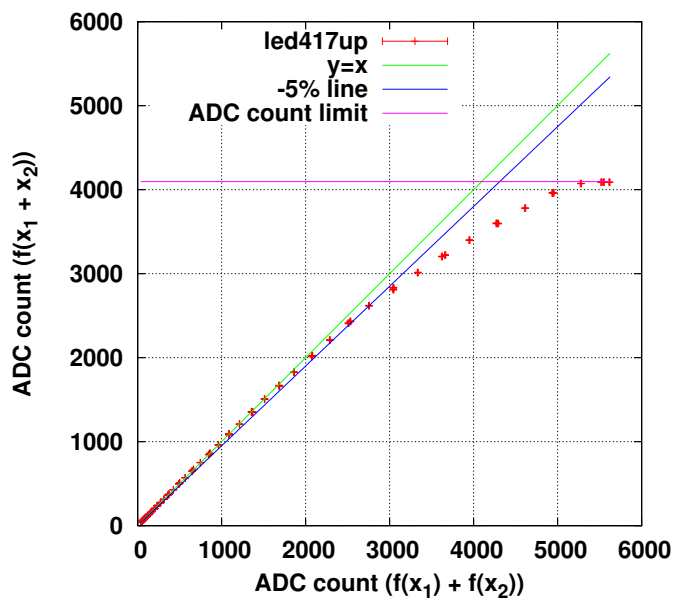This $V^{1.5}$ dependence and the feature of the current limit of the

Figure 28: Typical PMT correlation plot. Horizontal axis : $f(x_1) + f(x_2)$ Vertical axis : $f(x_1 + x_2)$, (f:photon   PMT output ADC count at peak time bin of $f(x_1 + x_2)$), x_1, x_2:photons from LED1,LED2 .

linearity can be explained well by the space charge effect. (detail is written in Appendix A.) The space charge between dynodes limits the linearity in this model.

The typical transit time of our PMT is about 33ns [110], and our PMT has 11 dynodes, so the transit time between dynodes would be about 3ns. When the input light pulse width is much more than this transit time , we can say that the current between electrodes does not depend on the position between electrodes, and that the assumption in Appendix A looks good. The typical FWHM of 1 muon pulse of our SD is about 20 ns, so this assumption seems good. So we expected that we can estimate each PMT linearity by using this $V^{1.5}$ dependence from measured data even if the supplied voltage is changed. And we expected that there is almost no temperature dependence of this limit so that we do not need to monitor this information so frequently for the linear range . These expectations were made sure by the pulse height histograms of the monitor data.
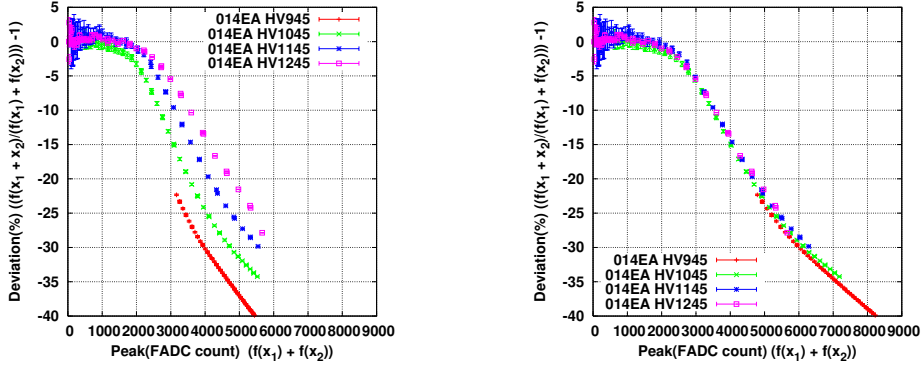

Figure 29: Left:PMT correlation plot supplied voltage dependence. Right:PMT correlation plot supplied voltage dependence. Peak ADC count of HV 945,1045,1145 data is scaled to HV 1245 by using $V^{1.5}$ dependence. Vertical axis : $f(x_1 + x_2)/(f(x_1) + f(x_2))$ -1 which does not depend on Peak count scale.

-5 percent non-linear points of all PMTs of deployed SDs is described in Figure.30 by using $V^{1.5}$ dependence. When the supplied voltages of all PMTs are scaled to 1100V, peak current distribution is like a Gaussian distribution and RMS/Mean is 18 %. This dispersion corresponds to the dispersion of the space charge ef-
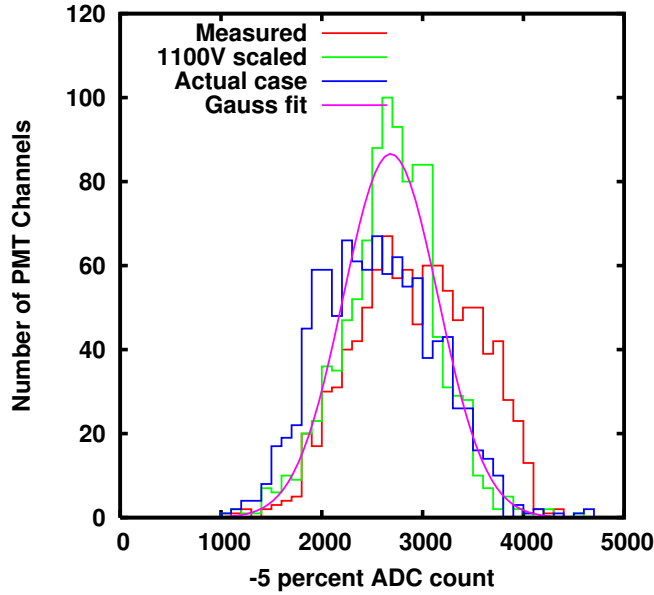
47

Figure 30: -5 percent non linearity point plot of all PMTs. Measured: measured -5 percent non-linearity point result, 1100V scaled:-5 percent non-linearity point is scaled to 1100V case, Actual case: the present situation after PMT gain is adjusted, Gauss fit: Gauss function fit to scaled distribution and mean is 2680 FADC count and root mean square is 470 FADC count.

fect under the same condition of PMTs. This dispersion may be because of the difference of the geometrical conditions between dynodes or the difference of the vacuum inside of the PMT.

At the present situation, 1 MIPs peak is adjusted to about 50 counts, and 2560 ± 570 counts is -5 percent non-linear point distribution in Figure.30, so the present dynamic range is about 51 ± 11 particles per 20ns. This typical linearity break corresponds to the detector response at about 650m in the 100 EeV vertical air shower.

– Linearity calibration using the pulse height information

The Pulse heights (FADC peak) are taken as a monitor data to check the linearity breaks and their variation. In this calibration method, the calibration source is cosmic ray signals.

The energy flux of cosmic rays shows a power low feature. On the other hand, the peak height of the triggered signal is expected to

48

show how large the air shower is or how close to the shower core when the pulse height is larger. So the peak height distribution is expected to reflect the power low of the primary cosmic rays.

If the non-linearity of PMTs show up, the peak height distribution is expected to show the break from the ideal peak height distribution. To measure this break is this calibration method. Actually, we do not know the ideal peak height distribution, so we took the average feature of the good PMTs as an ideal peak height distribution.

This calibration needs a lot of information of cosmic rays, so it takes so much time. We already checked that there is almost no temperature dependence from LED calibrations if the supplied voltage is the same. So the linearity break point is expected to be stable while this calibration is carried out.

Fig.31 shows an example of pulse height linearity obtained from linearity calibration by LED and the one estimated using pulse height monitor. In this figure, the supplied voltage is different from the voltage when linearity calibrations using LEDs are carried out, so the results by LEDs are scaled using the $V^{1.5}$ supplied voltage dependence of the linearity. The figure shows a good agreement between the monitor data and the results by LEDs and makes sure that the space charge effect in PMT is the main factor of the linearity break. In addition to that, this means that this effect does not much depend on the waveform shapes of the calibration source because the waveform signal of the cosmic rays as a calibration source is random.

- other monitored status

SD is operated using solar panel and battery charge, so it is important to monitor status of solar panel output voltage and current. The 1 pps pulses are generated from signals from satellites which is visible using a GPS antenna. The number of satellites which are visible is monitored using GPS module. 5 temperatures and 2 humidity sensors are equipped and the environment inside of the scintillator box and the electronics box is monitored. The rate of the atmospheric muons is stable and can be counted using SD, so the monitor of the rate is also useful to check the health of the SD.
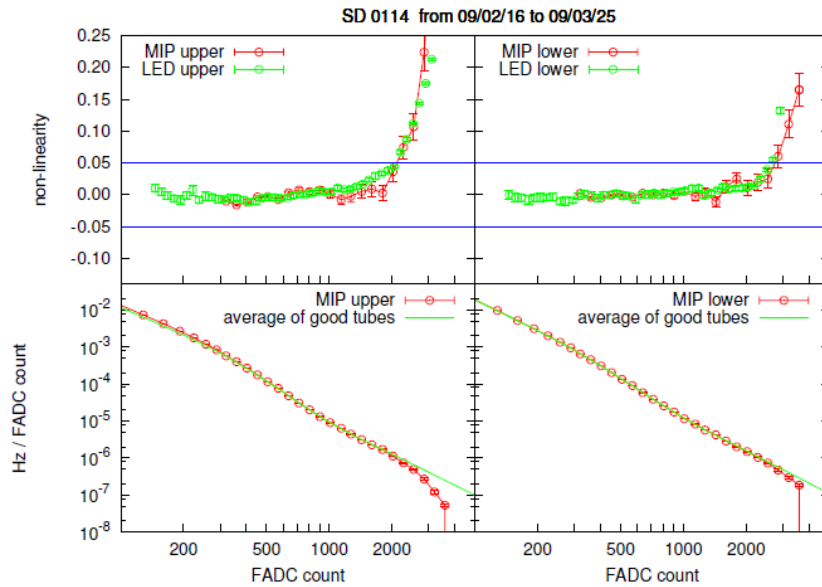
Figure 31: Result of comparison of linearity calibration using LED and calibration from monitor data. Top left panel shows deviation from estimated linear response at LED calibration and pulse height monitor for upper layer of a SD. Top right panel shows the same plot for a lower layer. Bottom left panel shows scaled pulse height histogram observed at upper layer and its average from good tubes. Bottom right panel shows the same plot for lower layer.

Fig.32 is an example of plot of monitoring data showing detected number of GPS satellites, battery voltage and its charging current and level-0, level-1 trigger rate plotted with SD environment monitor.

This information is used to check the health of SDs. If the GPS does not work well at one second, the timing of the acquired data from the SD at the second is not available for example.
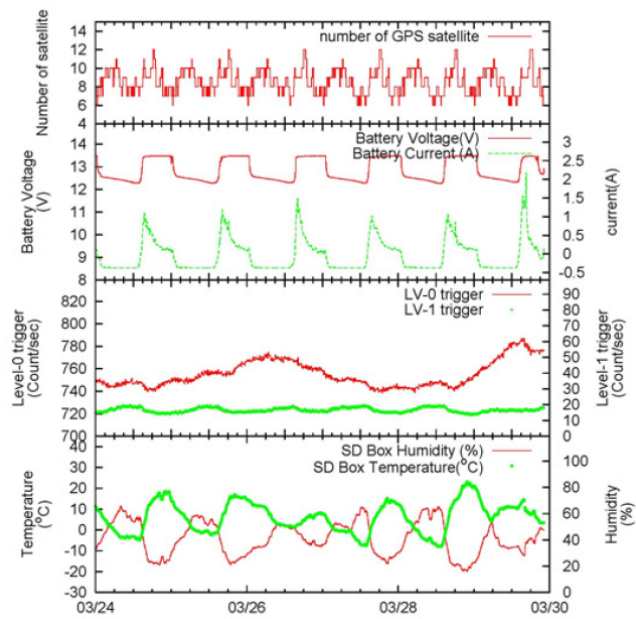
Figure 32: Monitoring plots, as a function of time, for one SD from March 22 to March 30 in 2009(UTC). From the top, the time variations in the number of detected GPS satellites, battery voltage and current, the rates of level-0 trigger and level-1 trigger, temperature and humidity inside of the SD box are shown.

5.3. Event Reconstruction and the Energy Scale

5.3.1. Event Reconstruction

After the energy depositions are determined by the 1 MIP calibration, the information of the timing of the leading edge of the signal and the energy depositions is used for event reconstruction as follows.

There are 2 types of fits in SD event reconstruction, to determine the geometry and the lateral density distribution. It begins with a fit for the geometry of the shower using the "modified Linsley" formula [112] which is given by

$$\chi^2 = \Sigma_{i=1}^{nSDs} \frac{(t_i - T_0 - T_{Plane} - T_D)^2}{T_s^2} + \frac{(\vec{R} - \vec{R}_{COG})^2}{(180m)^2} \tag{7}$$

where t_i is the leading edge time of i-th SD, T_0 is the time of the core hitting ground, T_{Plane} is the time of the shower front plane, T_D and T_S is the time delay and fluctuation, $\vec{R}$ is the core position and $\vec{R}_{COG}$ is the core position found from the center of gravity of observed charge.

The lateral density distribution is obtained by the fit of lateral distribution function (LDF) used by AGASA [113]. The used LDF formula is given by

$$\rho(r) \propto \left(\frac{r}{R_M}\right)^{-1.2} \left(1 + \frac{r}{R_M}\right)^{-(\eta-1.2)} \left(1 + \left(\frac{r}{1000[m]}\right)^2\right)^{-0.6} \tag{8}$$

$$\eta = 3.97 - 1.79 \cdot (\sec\theta - 1) \tag{9}$$

where $\rho(r)$ is charge density on r, R_M is Moliere distance and θ is zenith angle. Moliere distance 91.6m of AGASA is not changed and used here.

This lateral distribution function is actually applied to the detector response which corresponds to the energy depositions in the plastic scintillators. This detector response is counted using vertical equivalent muon (VEM) which corresponds to 2.05 MeV energy deposition in the plastic scintillator here and interpreted as charge density (VEM/m^2).

The charge density at 800m from the shower core S_{800} is used as an energy estimator. The primary energy can be represented well by S_{800} and zenith angle, so the table that consists of S_{800} and zenith angle for each primary energy from Monte Carlo simulation is prepared. The energy of the observed data can be reconstructed using this table. The table which is made using CORSIKA QGSjet-II which is shown in Fig.33.

These fitting procedure and formulae are tuned with the residuals of the fit to the data. The following quality cuts are applied to the data;

- Reduced χ^2 of geometry fit < 4

- Reduced χ^2 of LDF fit $\chi^2 < 4$

- Distance from the array boundary > 1.2 km

- Zenith angle $< 45°$

- Pointing direction uncertainty $< 5°$

- Fractional S_{800} error < 0.25
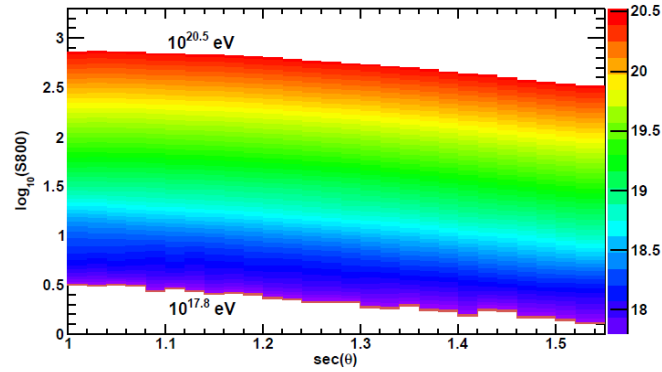
Figure 33: The zenith angle and S_{800} for each energy obtained from MC. The horizontal axis is zenith angle, the vertical axis is S_{800}. Different colors represent different primary energies.

5.3.2. Energy Scale

TA is the hybrid detector, and the SD energies and the FD energies can be compared using hybrid events which are measured both by FD and SD Figure.34 is the scatter plot of the energies of well-reconstructed 383 hybrid events. Hybrid events show that the energy of SD is 27 % larger than that of FD. We draw green lines as cut lines in this figure not to suffer from the bias in comparison. Figure.35 shows the proportion of the FD energies to -27% shifted SD energies using the data above each green line in Figure.34.

The mean values of the Gaussian fits are 0.02 ± 0.01 and 0.01 ± 0.02 in this figure, and the difference from the energy shift is not significant. The sigma value of the Gaussian fits are 0.13 ± 0.01 and 0.12 ± 0.02, which corresponds to about 20-30 % resolution. This resolution is expected to be mainly caused by the resolution of the measurement by SD because the energy resolution by FD is estimated to be about 10 %.

We scaled the SD energy of all the SD events by -27% such that the SD measured energy equals to the FD measured energy. This is because the FD measured energy is experimental as opposed to the SD measured energy, which heavily relies on the air shower simulation with significant ambiguities of hadronic interaction models at ultra-high energy. Number of events above 10 EeV is 856, and number of events above 40 EeV is 49, and the number of events above 57 EeV is 20 from the energy scale.

Figure.36 shows the differences of the arrival directions between FD and SD using hybrid events. The 68 % points from 0 degree in the distributions are $2.3°$ above $10^{18.5}$eV and $2.1°$ above 10^{19}eV. This distribution almost corresponds to the resolution of SD geometry reconstruction because the resolution of the geometry reconstruction of FD using hybrid data is about $0.1°$ and relatively negligible.
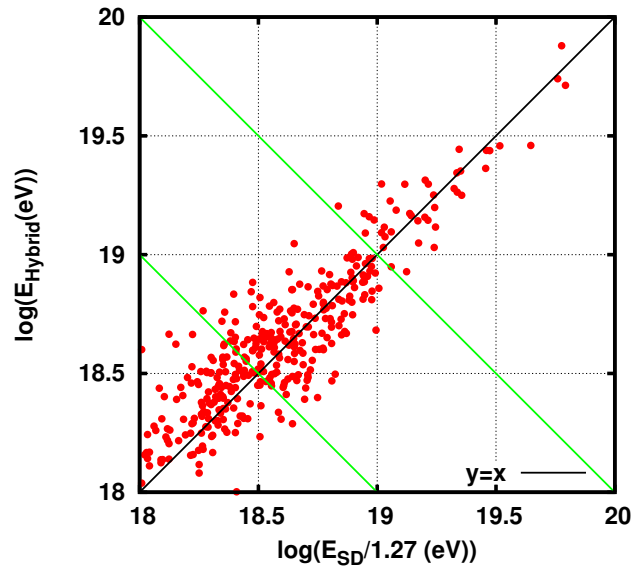
Figure 34: The comparison of measured energies using hybrid events which are observed in BRM and LR station is shown in this figure. Red circles are observed hybrid events. Green lines are the cut lines to check the data above $10^{18.5}$eV and above 10^{19}eV. Number of events above these lines is 238 and 42 correspondingly.
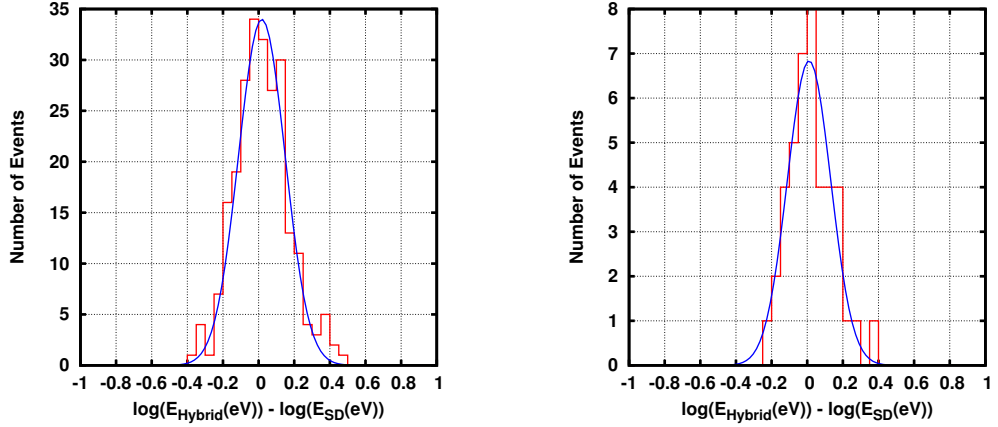
Figure 35: The differences of measured energies using hybrid events are shown here. Used events in this figure are the same as in Figure 34. The data above the green lines in Figure 34 is used as the data above $10^{18.5}$eV and 10^{19}eV. The horizontal axis is the difference between the FD energies and -27 % shifted SD energies. Left: events above $10^{18.5}$eV, Right: events above 10^{19}eV. Blue lines are the results of Gaussian fit.
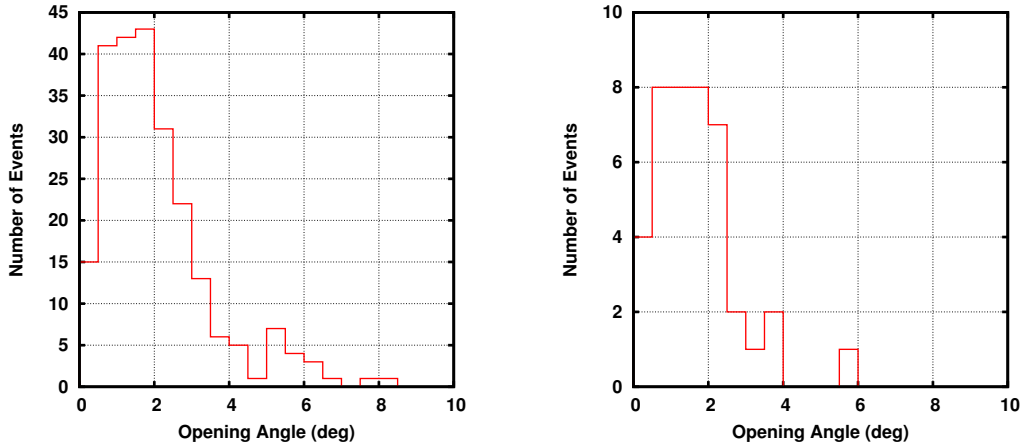

Figure 36: The differences of measured open angles using hybrid events are shown here. The completely same data set as in Figure35 is used for the data above $10^{18.5}$eV and 10^{19}eV. The data above $10^{18.5}$eV (10^{19}eV) is shown in the left (right) figure. The 68 % points from 0 degree in the distribution is 2.3° (2.1°).

6. Large Scale Anisotropy Analysis

The actual data reduction is shown in the previous section. The reduction gives arrival directions with about $2°$ accuracy above 10 EeV and when each event is observed. In this section we use these information to compare with the expectation from LSS. In Section.6.1, we construct the expectation from LSS using 2 Mass Extended Source Catalogue (XSCz). The magnetic deflections by regular Galactic magnetic fields are added to the LSS expectation and the methods of implementation are explained in Section.6.2. Kolmogorov-Smirnov (KS) test is used for the correlation search between data and expectations. The KS test which is used in this analysis is introduced in Section.6.3. The observed arrival directions are plotted in some coordinate systems in Section.6.4. The result of comparison using KS test of the data with isotropy is described in Section.6.5. The detailed result of comparison of the data with LSS with and without regular GMF is described in Section.6.6.

6.1. Large Scale Structure Model

We calculated expected observed flux ((relative exposure A)×(expected flux Φ)) χ in the following procedure. We compare observed events with Monte Carlo events using one-dimensional Kolmogorov-Smirnov test referring χ.

As a model of large scale structure, we used 2 Mass Extended Source Catalogue (XSCz) [115]. We use a sample of galaxies which are from 5 Mpc to 250 Mpc distant from the Earth and with Ks (2.2 μm) apparent magnitude < 12.5.

The galaxies within 5 Mpc was not included because they do not represent a proper statistical sample of LSS. The cut of 250 Mpc and the apparent magnitude cut are determined by the completeness of this catalogue. More than 90 % completeness for $|b| < 20°$ is achieved for sources brighter than 13.5 mag. The catalogue is incomplete near the Galactic center because the background light is blocked by large number of stars, but the even brighter sources can penetrate deep into the region. If Ks-band flux limit declines by about 0.5 mag, we can extract galaxies well down to $|b| \sim 5°$. Ks-band flux limit 12.5 mag is determined for better statistics and the galaxies are added in the incomplete region $|b| < 10°$ around the Galactic center. The detail of this process is described later in this section. More than that, accurate radial velocities are included for most galaxies when Ks-band flux limit is 12.5

mag where the radial velocities are available for about 40 % of the catalogue galaxies when Ks < 14 mag.

Especially for the case of lower energy threshold like 10 EeV, the uniform distribution is added to the LSS as the contribution far from 250 Mpc. This assumption of uniform distribution seems to be reasonable for our data because of the magnetic deflections of UHECRs and the cosmological principle. At lower energies, the random deflections by magnetic fields are expected to be larger and the deflections are roughly proportional to the reciprocal energy as reviewed in Section.2.2. The random deflections are estimated to be about 10-15° for 10 EeV protons only by Galactic magnetic fields using the latest results of Faraday rotation measurements [121]. The random deflections by inter-Galactic magnetic fields are estimated to be about 40° at 250 Mpc from our Galaxy when the field strength is 1 nG and the coherent length is 1 Mpc which is the upper limit from the Faraday rotation measurements [75] [116]. The random deflections by inter-Galactic magnetic fields depend on the distance and the deflections are estimated to be even larger for more distant sources. By the cosmological principle, the more distant clustering structure seems to be relatively smaller for us. The Corona Berealis structure dominates the 280-320 Mpc shell from our Galaxy in the northern hemisphere but the core of the structure lies only in $6° \times 6°$ region for us which can be smeared well just by random GMF effect for 10 EeV protons. For the higher energy threshold 40 and 57 EeV, the assumption of the uniform distribution seems to be also reasonable because of its small contribution by GZK effect and the small statistics.

After the distance and the magnitude cut, about 110,000 galaxies remains in the catalogue. In this catalogue, observed redshifts of all galaxies are available. Fig.37 shows the distribution of number of galaxies projected in the galactic coordinate using the Hammer aitoff projection.

We need to impose weights on galaxies to compensate number of galaxies which is cut by the limit of the apparent magnitude. Darker sources cannot be observed when they are far from the Earth with the same apparent magnitude limit, so the weights of the distant sources should be larger. We used sliding box weighting scheme to compensate invisible galaxies caused by the limit [117]. In this scheme, the distance dependence of weights is evaluated relatively by comparing nearest distributions of galaxies. So the weight can be determined using only galaxies in this catalogue. Fig.38 shows the distance dependence of weights calculated using this scheme. We can see the relative incompleteness caused by the limit of apparent magnitude as the

distance dependence of the weights.

Fig.39 shows the distribution of weights of galaxies projected in the galactic coordinate using the Hammer aitoff projection. In this figure, the color of the region which includes distant sources becomes darker than in the Fig.37.

Here we define a-priori 3 energy thresholds 10, 40 and 57 EeV which were used in HiRes, AGASA and Pierre Auger to avoid generating biases by searching energy thresholds. In the later section, we compare the data and the model above these 3 energy thresholds.

Then we calculate expected integral energy flux $\Phi(E_{th})$ in each direction to compare with observed arrival directions of UHECRs above an energy threshold E_{th}. The integral flux $\Phi(E_{th})$ from a single source at distance D can be expressed by

$$\Phi(E_{th}) = \frac{J^0(E_0)}{4\pi D^2(1+z)} \tag{10}$$

where E_0 is the energy threshold at the source and $J^0(E_0)$ is the integral flux above E_0 of the source. This E_0 is calculated considering interaction of CMB which consists of pion production and electron-positron pair production in the following procedure.

Proton energy loss during propagation from a source at redshift z can be described by the differential equation [36, 120]

$$\frac{1}{E}\frac{dE}{dz} = \frac{1}{1+z} + \frac{(1+z)\beta_0((1+z)E)}{H(z)}, \tag{11}$$

where

$$\beta_0(E) = -\frac{1}{E}\frac{dE}{dt} \tag{12}$$

at present cosmological epoch and the Hubble constant $H(z)$ is the same thing as in the equation (1). The first term in the equation (11) corresponds to the energy loss simply because of the cosmological expansion. The second term is for particle interactions. The energy threshold E_0 at the source as a function of observed energy E and redshift z is calculated by solving the equation (11) numerically. We consider 2 interaction processes in the second term in (11), so we can split the function $\beta_0(E)$ into the part β_0^π due to the pion photo-production and the part β_0^{ee} due to the electron-positron pair production. In the solving process, we use the approximation

$$\log \beta_0^\pi(E) = \sum_{n=1}^{5} a_n X^{n-1} \tag{13}$$

and

$$\log \beta_0^{ee}(E) = \sum_{n=1}^{5} b_n X^{n-1}, \tag{14}$$

where $X = \log(E/1eV)$. This approximation is valid above $10^{17.5}$ eV. The coefficients of this approximation are in the appendix of Ref.[120].

To get the concrete injection energy spectrum $J^0(E_0)$ of each galaxy, we need to assume the shape of the energy spectrum. Here we assume the simple power law of the injection energy spectrum

$$\frac{dJ^0(E)}{dE} = cE^p, \tag{15}$$

where c is the constant and p is the spectrum index. There is no luminosity evolution of each galaxy in the equation (15). Here, we assume that the injection energy spectra of all galaxies are same. So the constant c is same value for all galaxies. This is because there is no information of the luminosity of each galaxy for UHECRs so far and this issue is not so important when there are large number of sources.

In this model, p is only the parameter we need to assume. We fixed p as -2.62 from the point of the agreement with the observed energy spectrum. Fig.40 is the observed energy spectrum overlaid by the best fit expected energy spectrum. We use this power index value in the following study.

Now we can calculate $J^0(E_0)$ by $\int_{E_0}^{E_{max}} E^p$ for each galaxy. Here we set $E_{max} = 1000$ EeV because there is no event above 1000 EeV is observed. And we can calculate an integral flux $\Phi(E_{th})$ from a single source.

Fig.41 shows the distribution of expected flux above 10 EeV which reaches the Earth from weighted galaxies projected in the galactic coordinate using Hammer aitoff as an example. The energy loss of expected flux from nearby sources in propagation is smaller than that from distant sources, so the color of flux from nearby sources becomes relatively darker in this figure than in Fig.39.

The geometrical exposure of TA is calculated using the simplified formula shown in [114]. The air shower becomes larger if the energies of UHECRs become larger. So the trigger efficiency and the reconstruction efficiency approaches almost maximum if the energies become larger. In our case, the trigger efficiency becomes about 100 % when the energies of UHECRs above $10^{18.7} - 10^{18.8}$ eV and the zenith angle of the air showers is less than $45°$. So the exposure of ground arrays for UHECRs is expected to be simply expressed in the following way when the energies are above 10 EeV.

If the array is on the Earth, the Earth rotates on the axis so the exposure is irrespective of the right ascension if the detectors work continuously. The dependence of the exposure ω on the declination δ can be expressed by

$$\omega(\delta) \propto \cos(a_0)\cos(\delta)\sin(\alpha_m) + \alpha_m \sin(a_0)\sin(\delta), \tag{16}$$

where α_m is given by

$$\alpha_m = \begin{cases} 0 & \text{if } \xi > 1 \\ \pi & \text{if } \xi < -1 \\ \cos^{-1}(\xi) & \text{otherwise} \end{cases} \tag{17}$$

and

$$\xi = \frac{\cos(\theta) - \sin(a_0)\sin(\delta)}{\cos(a_0)\cos(\delta)}. \tag{18}$$

Here a_0 is the terrestrial latitude of the ground array and θ is the cut angle of the observed zenith angle. In our case, the latitude a_0 is 39.3° and the cut angle θ is 45°.

Fig.42 shows the distribution of expected flux multiplied by the relative exposure projected in the galactic coordinate using Hammer aitoff. The vertical color scales are same for 3 energy thresholds in this figure and the feature of the maps looks rather similar, so the difference of the color just means the difference of integral flux by energy thresholds.

Then we define a free parameter as a smearing angle which represents random components in the propagation of UHECRs.When we consider smearing angles θ_s, the integral flux $\Phi(E_{th})$ observed in the (l,b) direction is given by

$$\Phi(l, b, E_{th}) = \sum_i \Phi_i(E_{th}) w_i \tag{19}$$

where i is the index of galaxies in the catalogue and

$$w_i = \frac{\exp(-(\theta/\theta_s)^2)}{\pi \theta_s^2} \tag{20}$$

is a weighting factor and θ is the angle between galaxy i and the line of sight.

Depending on the energy threshold, the contamination from the sources which are far from 250 Mpc is considered as isotropic component. The total flux within the redshift z_{max} can be described by

$$\Phi_{tot}(E_{th}) = \frac{cn_{src}}{4\pi} \int_0^{z_{max}} dz \frac{J^0(E_0)}{H(z)(1+z)} \tag{21}$$

61

where n_{src} is the estimated uniform source density from the catalogue and z_{max} is set to be 5. Here we assume that the scale of 250 Mpc is large enough for the flux to be isotropic, so the proportion of the isotropic component to the total flux can be given by $\int_{z(D=250Mpc)}^{z_{max}} dz \frac{J^0(E_0)}{H(z)(1+z)} / \int_0^{z_{max}} dz \frac{J^0(E_0)}{H(z)(1+z)}$.

There is actually about 30 % energy resolution in the event reconstruction when the energies are above 10 EeV as mentioned in the Section.5.3.2, so the observed differential energy spectrum $d\Phi_{obs}(l, b, E)/dE$ is modified from $d\Phi(l, b, E)/dE$ like

$$\frac{d\Phi_{obs}(l, b, E)}{dE} = \int_0^\infty \frac{d\Phi(l, b, E')}{dE'} \frac{1}{\sigma\sqrt{2\pi}} \exp\left(-\frac{(E - E')^2}{2\sigma^2}\right) dE', \qquad (22)$$

where σ is the energy resolution. There are actually events with lower than 10 EeV true energy even when we apply 10 EeV energy threshold to observed events. We simulated $d\Phi(l, b, E)/dE$ when we apply energy thresholds to $d\Phi_{obs}(l, b, E)/dE$ in the following way.

We reconstructed Monte Carlo events which have E^{-3} energy spectrum $d\Phi_{obs}(l, b, E)/dE$ and simulated the thrown energy distributions $d\Phi(l, b, E)/dE$ when we apply 10, 40 and 57 EeV energy threshold to reconstructed energies. Fig.43 shows the thrown energy distribution to the Monte Carlo simulation. The power index of the energy spectrum is not changed by the energy resolution. The fractions of the events which are lower than the energy thresholds are about 30%, 20% and 20% for 10, 40 and 57 EeV energy threshold. Roughly speaking, the effect of magnetic fields depends on the reciprocal energies of the events. The average bending angle can be roughly estimated to increase about 25-30 % considering the contamination in average using this dependence.

We generated expected flux map from LSS considering this contamination. We made expected flux map for $10^{18.0} - 10^{18.1}$, $10^{18.1} - 10^{18.2}$ $\cdots$ $10^{20.4} - 10^{20.5}$ eV and cumulated them for each arrival direction with the weight of simulated number of events in Fig.43.

The distance dependence of the fraction of the flux is shown in Fig.44 when we replace the uniform source density with LSS within 250 Mpc. The flux is rather concentrated within the nearby distance because of the clusters of LSS. The fraction of the flux which comes far from 250 Mpc is estimated to be about 59 %, 32 % and 7 % of total flux when the energy thresholds are 10, 40, and 57 EeV in this assumption as we can see in the right figure of Fig.44. We use this proportion to add the isotropic component to the expected observed flux within 250 Mpc.

We calculated expected observed flux ((relative exposure A(l,b))×(expected flux $\Phi_{tot}(l, b)$)) $\chi_{tot}(l, b)$ using these procedure except for the region ($|l| < 90°$, $|b| < 10°$) around the Galactic center. In this region, the completeness of galaxy catalogue is drastically worse because the region around the Galactic center is quite dense and opaque from infrared photons. To make a complete map in our exposure, we extrapolate the distribution of galaxies in the following way.

Firstly, we exclude galaxies with coordinates $|l| < 30°$, $|b| < 10°$ and galaxies with coordinates $30° \leq |l| < 90°$, $|b| < 5°$. And then, we add mirror galaxies with coordinates with $l' = l$ and $b' = \pm 20 - b$ when $|l| < 30°$, $|b| < 10°$. Here the plus(minus) sign corresponds to $b > 0$ ($b < 0$). We also add mirror galaxies with coordinates with $l' = l$ and $b' = \pm 10 - b$ when $30° \leq |l| < 90°$ and $|b| < 5°$.

This extrapolation way considers only the continuity around the boundary of the incomplete region. In TA case, the exposure around the Galactic center is small. In addition to that, the statistics above 40 EeV is small. So we applied this approximation and used all observed data without cut above 40 EeV. More than 800 events are observed above 10 EeV and the magnetic deflection around 10 EeV may be much more than 10 degrees so we applied the cut to the data above 10 EeV after this extrapolation. We considered the detailed cut in the next section.

Fig.45 and Fig.46 show the distribution of the expected flux $\chi_{tot}(l, b)$ above 3 energy thresholds when smearing angles are 6 degrees. The average of the total expected flux is scaled to 1 in Fig.45 and each contour band contains one fifth of the total flux in Fig.46. The difference of the contamination of isotropic component is visible in this figure. The contrast is clearer when the energy threshold is higher. If the distribution of observed arrival directions follow LSS, number of events which dropped at each contour of Fig.46 should be same when statistics is infinity. In this meaning, the maps of Fig.46 overlaid with observed arrival directions are drawn many times in the later sections.
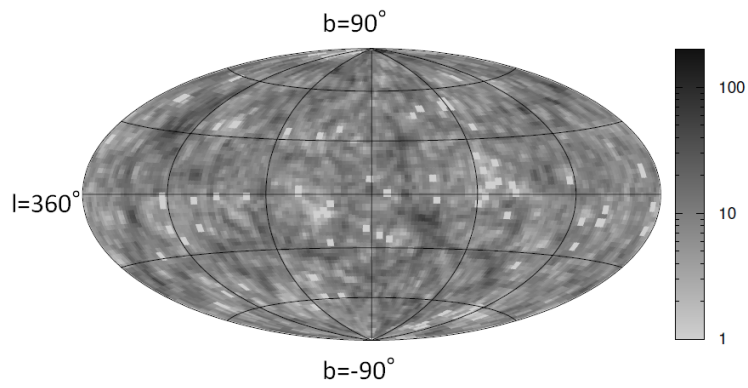
Figure 37: The distribution of number of galaxies projected in the galactic coordinate using Hammer aitoff. Number of galaxies is accumulated in each $2(\mathrm{deg}) \times 2(\mathrm{deg})/\cos(b)$ region and expressed as color.
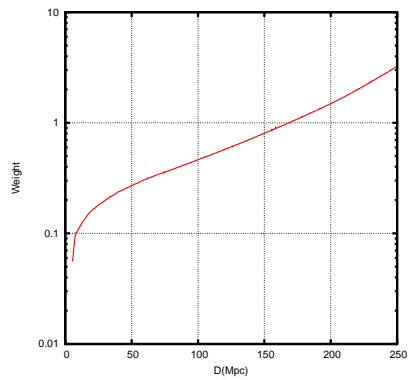

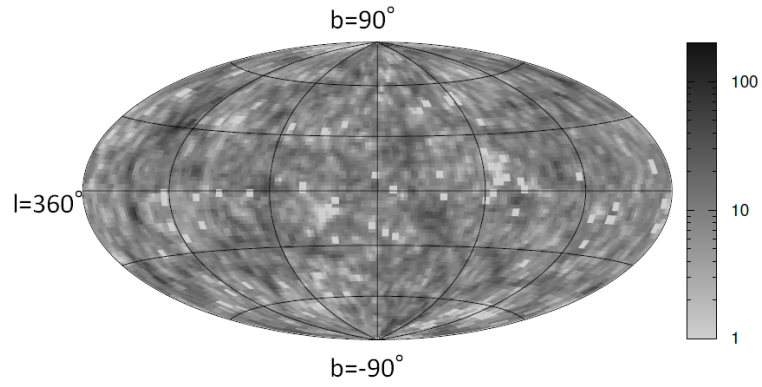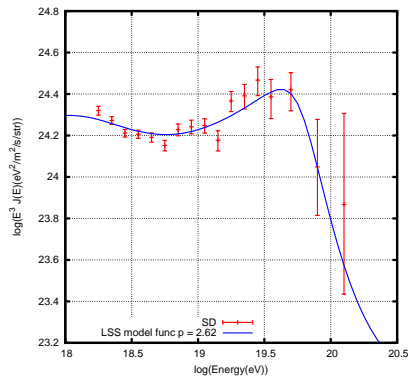Figure 38: The distance dependence of weights which are calculated using sliding box weighting scheme.

Figure 39: The distribution of weights of galaxies projected in the galactic coordinate using Hammer aitoff. The weights of galaxies are accumulated in each $2(\deg) \times 2(\deg)/\cos(b)$ region and expressed as color.

Figure 40: The observed energy spectrum which is fitted by the primary energy spectrum index 2.62. $\chi^2/\text{d.o.f}$ is 1.4 when the energies are above 10^{18} eV.
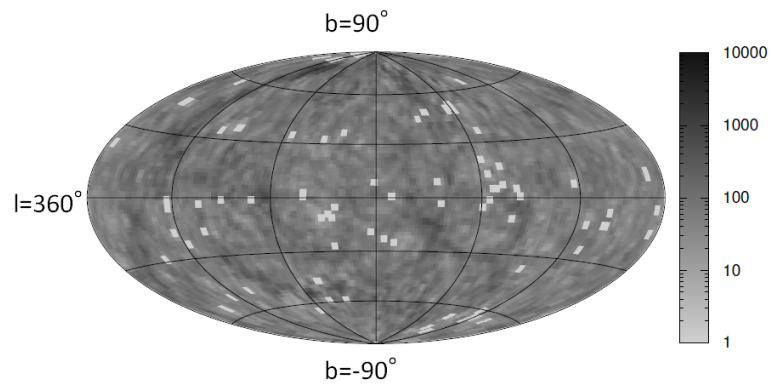
Figure 41: The distribution of expected flux above 10 EeV which reaches the Earth from galaxies projected in the galactic coordinate using Hammer aitoff. The expected flux from weighted galaxies are accumulated in each $2(\deg) \times 2(\deg)/\cos(b)$ region and expressed as color. In this figure, the absolute value of the scale of the color is arbitrarily determined and does not have any meanings.
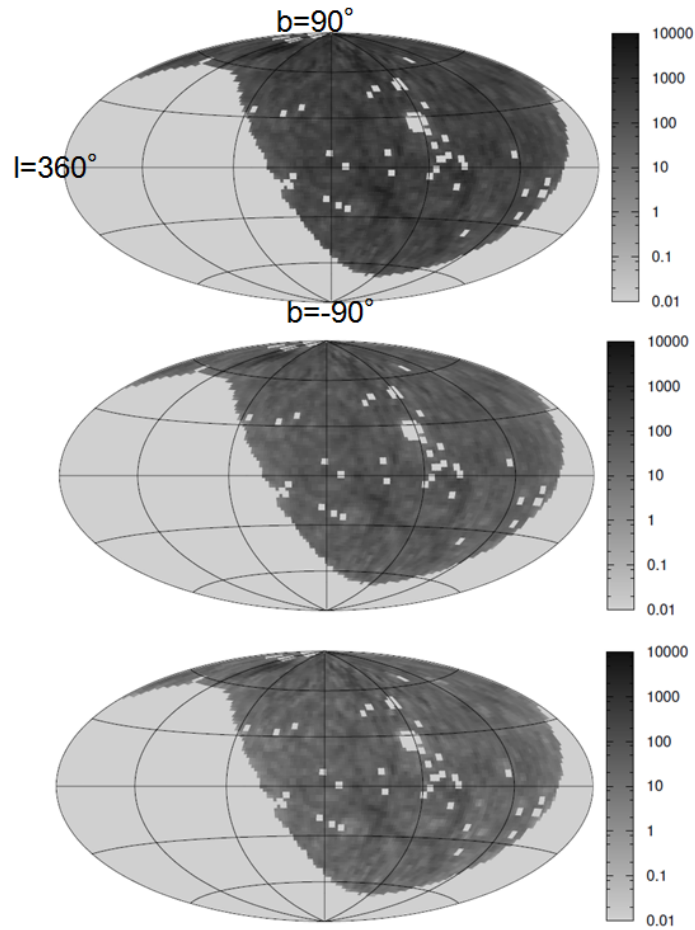
Figure 42: The distribution of expected flux from weighted galaxies multiplied by the relative exposure of TA above 10 EeV, 40 EeV, and 57 EeV projected in the galactic coordinate using Hammer aitoff. Top figure: E > 10 EeV, middle: E > 40 EeV, bottom: E > 57 EeV. The expected flux from weighted galaxies are accumulated in each 2(deg) × 2(deg)/cos(b) region and expressed as color. The absolute value of the scale of the color is the same thing as in Fig.41.
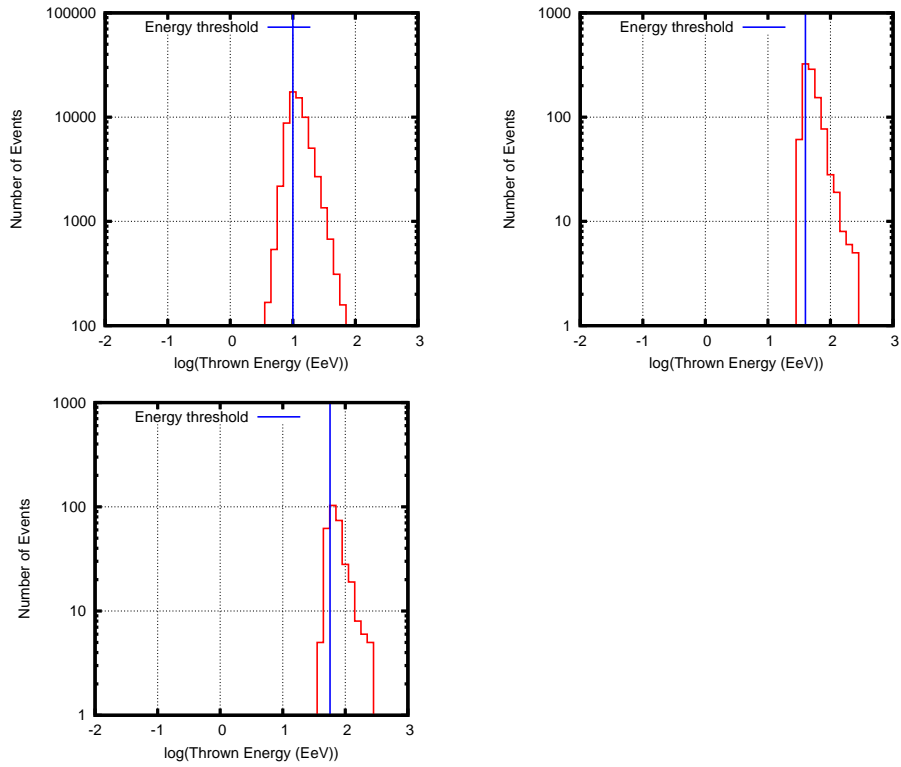
Figure 43: The thrown energy distributions to the Monte Carlo simulation are shown here. Energy spectrum of thrown Monte Carlo events follows E^{-3}. The energy thresholds 10, 40 and 57 EeV are applied to reconstructed energies of Monte Carlo events. The events above 10, 40 and 57 EeV are shown in the left, middle and right figure. The total number of reconstructed events which have energies above each energy threshold is 64746, 970 and 310 respectively. The number of events which have lower thrown energies than the applied energy thresholds is 20000, 206 and 74 respectively.
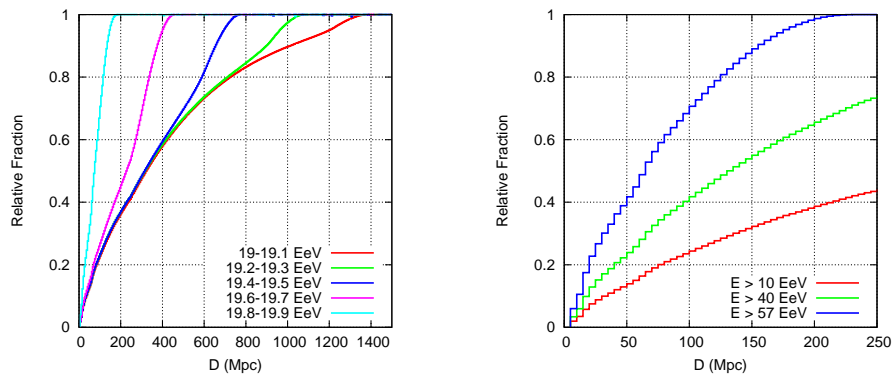
Figure 44: The distance dependence of the fraction of the contribution to the observed flux is shown in the left figure completely in the same way as in Fig.5. The uniform source density is replaced by LSS within 250 Mpc by scaling the total flux of LSS to that of uniform source density within 250 Mpc. In the right figure, the distance dependence of the fraction for the same model as in the left figure is drawn for the energies above 10, 40 and 57 EeV. The feature within 250 Mpc for three energy thresholds which we use for anisotropy search is drawn in this figure.
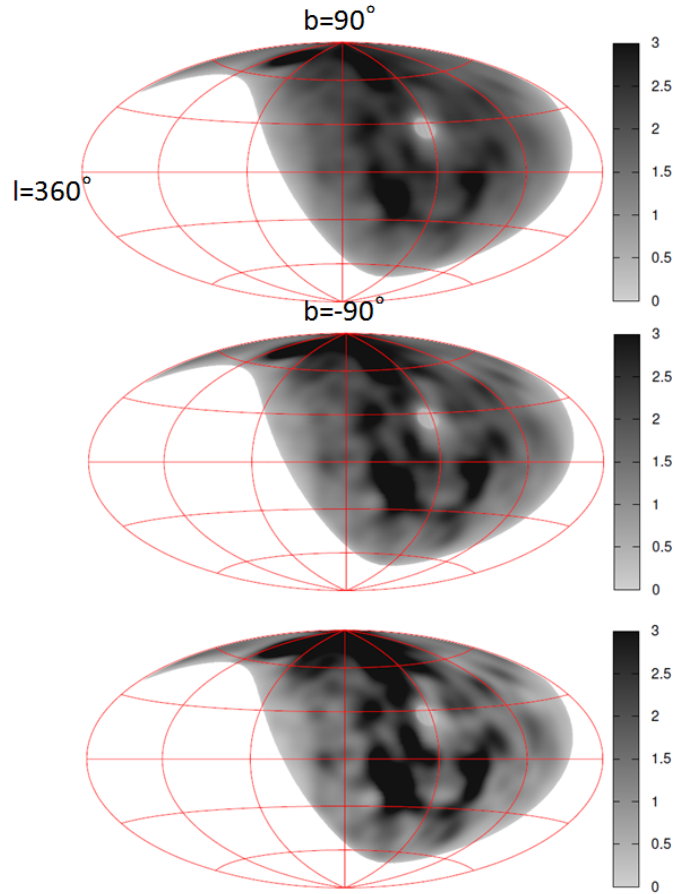
Figure 45: The contour map of expected flux $\chi_{tot}(l, b)$ above 10 EeV, 40 EeV, and 57 EeV is shown here. Top figure: E > 10 EeV, middle: E > 40 EeV, bottom: E > 57 EeV. The average of the total expected flux is scaled to 1. The isotropic components are 59 %, 32 % and 7 % of the total flux, respectively.
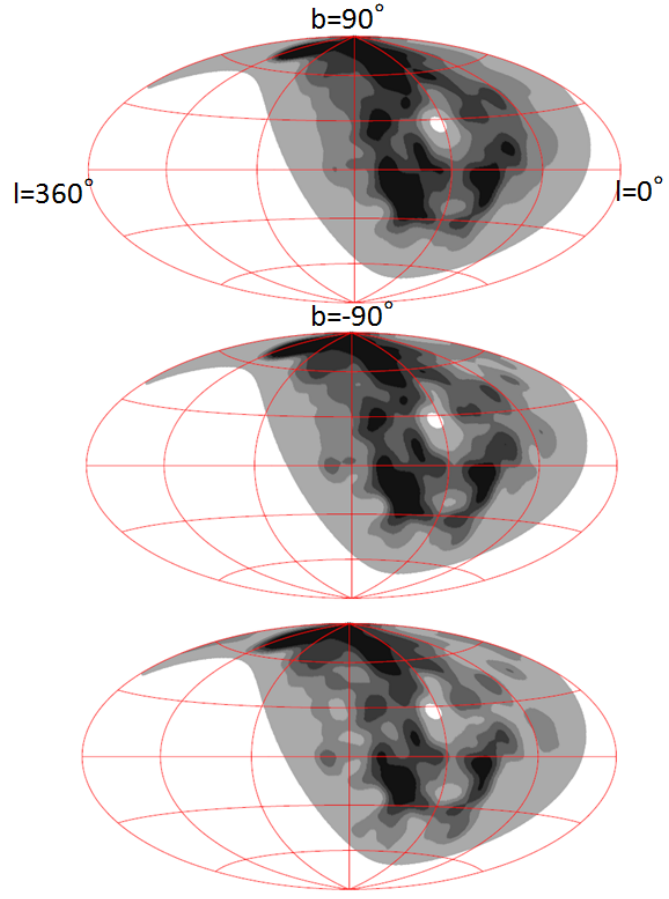
Figure 46: The contour map of expected flux $\chi_{tot}(l, b)$. Each contour band contains one fifth of the total flux. The expected flux in the darker region is larger. Top figure: E > 10 EeV, middle: E > 40 EeV, bottom: E > 57 EeV.

6.2. Regular Galactic Magnetic Field

Regular component of Galactic magnetic field (GMF) distorts expected χ map coherently. This effect cannot be included as a Gaussian component in a smearing angle.
So we implemented this effect to LSS analysis. The methods are shown here.

There is an issue of the ambiguity of the regular Galactic magnetic field models, so we need to consider the model dependence when we include this effect. Despite the progress of several observations of Faraday rotation, there is no confirmed overall picture of the Galactic magnetic fields including its disk fields and halo fields. Firstly we show the models of regular Galactic magnetic fields which have been considered and then we show the methods to implement our analysis. We also consider the uncertainty of the incomplete region using various regular Galactic magnetic field in this section.

6.2.1. Regular Galactic Magnetic Field Models

- Disk field

  The density of the Galaxy is concentrated on the Galactic disk. The spiral feature of the Galaxy is observed and the regular Galactic magnetic field related to that is also observed.

  The direction of the regular Galactic magnetic field at the sun vicinity is observed, so the direction on this spiral arm is known. But the direction of the regular GMF on the spiral arm is not known which is at the opposite side from the Galactic center.

  There are several models typically considered which are related to the uncertainty of the direction of the regular GMF. Here we introduce bi-symmetric spiral (BSS) field model and axi-symmetric spiral (ASS) field model and ring model. Fig.6 shows examples of the direction of these models. The direction of BSS model is symmetric from z direction which is perpendicular to the Galactic disk. The direction of ASS model is symmetric around the axis which is perpendicular to the Galactic disk and is located at the Galactic center. The ring model has a concentric circular feature. In this model, the direction depends only on the distance from the Galactic center. The ring model is rather disfavored but actually there is no experimental constraint so far [81].

  Here we applied the logarithmic spiral field model with coplanar and constant pitch angle which is shown in Ref.[15, 122]. This form can be

written in the cylindrical coordinate system which is centered at the Galactic center as

$$\begin{cases} B_r &= B(r,\theta,z)\cos p \\ B_\theta &= B(r,\theta,z)\sin p \\ B_z &= 0, \end{cases} \qquad (23)$$

where p is the pitch angle. When the BSS model is used,

$$B(r,\theta,z) = B(r)\cos\left(\theta - b\ln\frac{r}{R_\odot} + \phi\right)\exp\left(-\frac{|z|}{z_0}\right), \qquad (24)$$

where

$$\phi = b\ln\left(1 + \frac{d}{R_\odot} - \frac{2}{\pi}\right) \qquad (25)$$

and $b = 1/\tan p$ and d is the distance to the first field reversal. When the ASS model is used,

$$B(r,\theta,z) = B(r)\left|\cos\left(\theta - b\ln\frac{r}{R_\odot} + \phi\right)\right|\exp\left(-\frac{|z|}{z_0}\right). \qquad (26)$$

$B(r)$ is the amplitude of the regular GMF model and is defined as

$$B(r) = \begin{cases} B_0\frac{R_\odot}{r\cos\phi} & r > R_c \\ B_0\frac{R_\odot}{R_c\cos\phi} & r \leq R_c. \end{cases} \qquad (27)$$

When the ring model is used, the applied formula is taken from Ref.[83].

$$B(r,\theta,z) = D_1(r,z)D_2(r) \qquad (28)$$

$D_1(r,z)$ is defined as

$$D_1(r,z) = \begin{cases} B_0\exp\left(-\frac{R_\odot-r}{R_0} - \frac{|z|}{z_0}\right) & r > R_c \\ B_0\exp\left(-\frac{|z|}{z_0}\right) & r \leq R_c. \end{cases} \qquad (29)$$

$D_2(r)$ means the signature in this model.

$$D_2(r) = \begin{cases} +1 & r > 7.5 \text{ kpc} \\ -1 & 6 \text{ kpc} < r \leq 7.5 \text{ kpc} \\ +1 & 5 \text{ kpc} < r \leq 6 \text{ kpc} \\ -1 & r \leq 5 \text{ kpc}. \end{cases} \qquad (30)$$

When the BSS model in Ref.[83] is applied, the exponential type of the radial dependence like the equation (29) is used.

- Halo field

  Fig.7 is the result of the recent observation of the RM amplitudes which was shown in Ref.[123]. This figure shows clear antisymmetric feature below and above the Galactic plane.

  This seems to be also an indication of the antisymmetric halo field. The detailed model fitting using parameters of this antisymmetric toroidal halo field model with disk field model using recent data of RM is shown in Ref.[121].

  The formula of the toroidal field model is taken from Ref.[83, 124].

  $$B_\theta^H(r, z) = B_0^H \frac{1}{1 + \left(1 + \frac{|z| - z_0^H}{z_1^H}\right)^2} \frac{r}{R_0^H} \exp\left(-\frac{r - R_0^H}{R_0^H}\right). \qquad (31)$$

  This formula is the case of the halo field at the northern hemisphere. The direction of the magnetic field is the opposite at the southern hemisphere.

  Fig.47 shows the distribution of the field strength and the schematic view of the free parameters related to the geometry in this formula using the parameters in Ref.[83]. z_0^H is the height at the maximum field strength in this model. z_1^H means the thickness of the vertical distribution in the model. R_0^H corresponds to the width of the horizontal distribution of this halo field model.

- Vertical field

  The existence of this component is ambiguous from the point of observation as reviewed in Section.2.2. So this field is not applied in this thesis.

6.2.2. Methods

We calculated the distortion caused by the regular Galactic magnetic fields in the previous subsection using following procedure.
We define the original direction as (l',b') in the Galactic coordinate system and actually observed direction as (l,b). We calculated only this relation
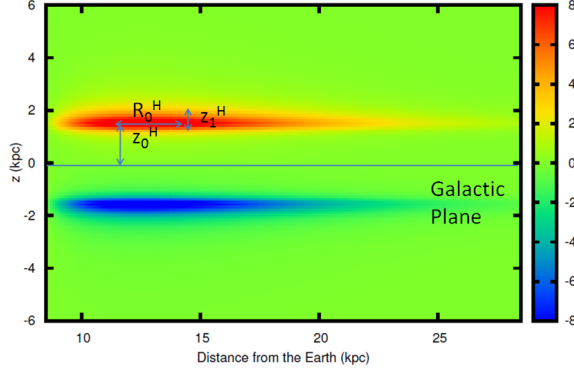
Figure 47: An example of the distribution of the field strength using the halo field model (31) in this figure. The free parameters in this formula using the parameters in Ref.[83]. The color shows the field strength and the maximum color range in this figure is 8 uG. $z_0^H = 1.5$ kpc, $z_1^H = 0.2$ kpc when $|z| < z_0^H$ and otherwise $z_1^H = 0.4$ kpc, $B_0^H = 10$ uG and $R_0^H = 4$ kpc.

$(l, b) \mapsto (l', b')$ to get a deflected flux map. The reason of this is explained in the following. We start from the phase space distribution along the trajectories of cosmic rays.

Let us consider the evolution of the phase space distribution $f(\vec{x}, \vec{p})$ of cosmic rays from the time t to $t + dt$. The number dN of particles around the $\vec{x'}, \vec{p'}$ at $t' = t + dt$ can be given by

$$f(\vec{x'}, \vec{p'})d^3x'd^3p'. \tag{32}$$

This number remains constant, if the Jacobian of the transformation $\vec{x}, \vec{p} \mapsto \vec{x'}, \vec{p'}$ which is given by

$$J = \frac{\partial(\vec{x'}, \vec{p'})}{\partial(\vec{x}, \vec{p})} \tag{33}$$

is one. From $\vec{x'} = \vec{x} + \vec{v}dt$ and $\vec{p'} = \vec{p} + \vec{F}dt$, the diagonal component of J is

$$1, 1, 1, 1 + \frac{\partial F_x}{\partial p_x}dt, 1 + \frac{\partial F_y}{\partial p_y}dt, 1 + \frac{\partial F_z}{\partial p_z}dt, \tag{34}$$

while the off-diagonal components are of order $O(dt)$. So the expansion of the dJ to first-order of dt in first-order is given by

$$J = 1 + \left(\frac{\partial F_x}{\partial p_x} + \frac{\partial F_y}{\partial p_y} + \frac{\partial F_z}{\partial p_z}\right)dt + \cdots \tag{35}$$

75

Thus the phase space distribution $f(\vec{x}, \vec{p})$ is constant along a trajectory, if $\nabla_p \vec{F} = 0$. This condition is satisfied in an electromagnetic field. $p = |\vec{p}|$ is constant in a pure magnetic field, so $p^2 f(\vec{x}, p)$ is also constant in this condition. Now we are considering purely regular Galactic magnetic fields, so this condition is fulfilled.

The conservation of the phase space element $d\Gamma = d^3 p d^3 x$ during the evolution is also stated in this Liouville's theorem. The element of $d^3 p$ of the orthogonal coordinate system can be converted to $p^2 dp d\Omega$ of the spherical coordinate system where $d\Omega$ is the phase space of the direction vector. The element of $d^3 x$ of the orthogonal coordinate system can be converted to $dAdz$ of the coordinate system of the flux tube of cosmic rays where the cross section dA of the flux tube is perpendicular to the momentum and the coordinate z is along the trajectory.

So the phase space element $d\Gamma$ can be converted to $p^2 dp d\Omega dA dz$. Now the observed differential flux $dN/(dAdtd\Omega dE) \propto d\Phi(l, b)/dE$ can be expressed by the phase space distribution as

$$\frac{dN}{dAdtd\Omega dE} = vp^2 f(\vec{x}, p)\frac{dp}{dE} = p^2 f(\vec{x}, p) \qquad (36)$$

, where v is the velocity of the cosmic rays. So the differential flux along the cosmic ray trajectory is constant.

$$\frac{d\Phi(l', b')}{dE} = \frac{d\Phi(l, b)}{dE} \qquad (37)$$

According to this relation, the differential flux in corresponding points before and after the correction for the Galactic magnetic field are simply equal. Thus, the flux map corrected for GMF can be easily calculated by tracing backward particle trajectories. The uniform flux distribution must be transformed to a uniform one in the pure magnetic fields also according to this result.

So the total integral flux $\Phi_{tot}(l, b, E_{th})$ can be given by

$$\Phi_{tot}(l, b, E_{th}) = \int_{E_{th}}^{\infty} \frac{d\Phi(l', b', E)}{dE}dE + \Phi_{iso}(l, b, E_{th}), \qquad (38)$$

where $\Phi_{iso}(l, b, E_{th})$ is the isotropic component from distant sources far from 250 Mpc. This integration is numerically carried out with 10 EeV resolution in this thesis.

Tracing backward particle trajectories is the process to follow the trajectory of a particle with the same energy and opposite charge that leaves the Earth in that direction up to a point where the effect of the galactic magnetic field becomes negligible [125]. The trajectories of anti-proton with charge -e and energy E leaving the Earth can be obtained numerically solving the equation

$$\frac{d^2\vec{x}}{d^2t} = -\frac{ec^2}{E}\frac{d\vec{x}}{dt} \times \vec{B}(\vec{x}).$$ (39)

We actually used anti-proton back-tracking calculation from the Earth to 100 kpc far away from the Galactic center to get the conversion $(l, b) \mapsto (l', b')$.

6.2.3. Contamination of the Flux from the Incomplete Region

As described in the Section.6.1, we determined to cut the incomplete region to minimize the uncertainty of the expected flux when we use the data above 10 EeV because of the larger number of data quantity. If we assume that the expected flux is completely unknown in the region ($|l| < 90°$, $|b| < 10°$), there are 2 points needed to be considered. One is the effect of the regular Galactic magnetic field. The flux from this region can go out, deflected by the regular Galactic magnetic field.

To estimate the expanded region by the regular Galactic magnetic field, we used some types of models. ASS(BSS) and even(odd) models in Ref.[15] are tested using the anti-proton backtracking in the previous section as examples of disk field models. Ring + halo and BSS + halo models in Ref.[83] are tested as examples of disk + halo field models. Firstly, we set the points per $0.5° \times 0.5°$ along the Galactic latitude and longitude all over the sky. Then we backtrack each point to the original direction using 10, 20, 30, $\cdots$ 100 EeV. If the point reach the incomplete region, we count the observed steradian $0.5° \cdot 0.5° \cdot \cos(b)$. The accumulated observed steradian corresponds to the expanded region by the regular Galactic magnetic field for each energy.
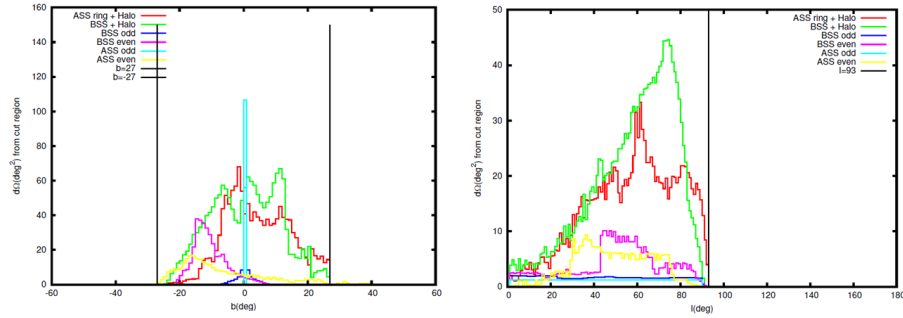
Fig.48 shows the expanded incomplete region by some regular Galactic magnetic fields which is accumulated with E^{-3} weight by the Galactic latitude and by the Galactic longitude. If there is no magnetic deflection, we can see the histogram just inside of $|b| < 10°$ in the left figure, and inside of $|l| < 90°$ in the right figure. At the right figure, we cannot see the histogram above 93°. This is because the deflection feature of considered all the models is almost vertical to the Galactic plane. The vertical field is not considered in this thesis. The histograms of the odd models in this figure are quite

small because the deflection pattern avoids to reach the region around the Galactic center. The height of the histograms of the fields with this halo models is rather high because of the large deflection angles. But the maximum and minimum value of the histogram is not so much different between the disk model and the disk + halo model and the histogram is hardly seen at $|b| > 27°$. So we determined the cut region related to the regular Galactic magnetic field as $(|l| < 93°, |b| < 27°)$ above 10 EeV.

The other is the effect of the smearing angle. The flux from this region can go out, smeared by some reasons like random extra-Galactic magnetic fields and like random Galactic magnetic fields. This is the free parameter of this analysis, so we cannot test using the smearing angle which is larger than the cut angle if we fix the cut angle. We fixed the cut angle as 25° just because this is enough large angle from the point of our statistics.

Considering these two factors, we determined the cut region as $(|l| < 118°, |b| < 52°)$ above 10 EeV for safety.

Figure 48: The expanded incomplete region by some regular Galactic magnetic fields which is accumulated with E^{-3} weight by the Galactic latitude and by the Galactic longitude. The left figure shows the accumulated observed steradian along the Galactic longitude. So we can see the latitude dependence in the left figure. The right figure shows the accumulated observed steradian along the Galactic latitude. So we can see the longitude dependence in the right figure. ASS(BSS) and even(odd) models in Ref.[15] are tested as examples of disk field models. Ring + halo and BSS + halo models in Ref.[83] are tested as examples of disk + halo field models. The black line is the determined cut region. Most of all the histograms are inside of the line.

6.3. Kolmogorov-Smirnov Test

After we make expected flux map described in the previous section, we assign corresponding expected flux value to each observed event, and then we compare the values of observed events with the values of 1,000,000 Monte Carlo events using one-dimensional Kolmogorov-Smirnov(KS) test.

Here we take the expected flux from LSS as the dimension of this test to maximize the difference between the structure and isotropy. If the distribution of the arrival directions follow LSS, the arrival directions are expected to be concentrated in the higher flux region such as dark region in Fig.46. This concentration is our estimator. If there is no significant concentration, events are isotropic. If we can sort events by the corresponding expected flux from LSS, this sorting process minimizes the solid angle which is occupied by events at high expected flux end when the events come from LSS. Our KS test is doing this process without binning events in the following way to compare events with LSS models.

KS test is understood well as a test which compares continuous data with a function of one variable. In our case, firstly we make a cumulative distribution function $S_{N_1}(\chi)$ from N_1 observed events and corresponding expected flux $\chi(l, b)$. And then we make a cumulative distribution function $S_{N_2}(\chi)$ from N_2 simulated events and calculate the greatest discrepancy D between 2 cumulative distribution function. This D is called as D-statistics and given by

$$D = \max_{-\infty < \chi < \infty} |S_{N_1}(\chi) - S_{N_2}(\chi)|. \tag{40}$$

The left of Fig.49 shows the example of the observed D.

It is convenient to use KS test because we can approximately calculate the significance probability from D in a good accuracy under the null hypothesis that the 2 distributions come from the same distribution. The significance probability that D above observed D (D_{obs}) is accidentally observed can be given by

$$Pr(D > D_{obs}) = Q_{KS}\left(\sqrt{\frac{N_1 N_2}{N_1 + N_2}} D\right) \tag{41}$$

where the function Q_{KS} is

$$Q_{KS}(x) = 2 \sum_{j=1}^{\infty} (-1)^{j-1} \exp(-2j^2 x^2). \tag{42}$$

This significance probability does not depend on the distribution when the distribution is continuous.

We actually simulate expected D 1,000,000 times by Monte Carlo method from LSS model and estimate $\Pr(D > D_{obs})$, so we do not suffer from the inaccuracy of the formulae even when the observed number of events is very small. The right of Fig.49 shows the example of the simulated distribution of D from LSS model and the corresponding region of $\Pr(D > D_{obs})$.
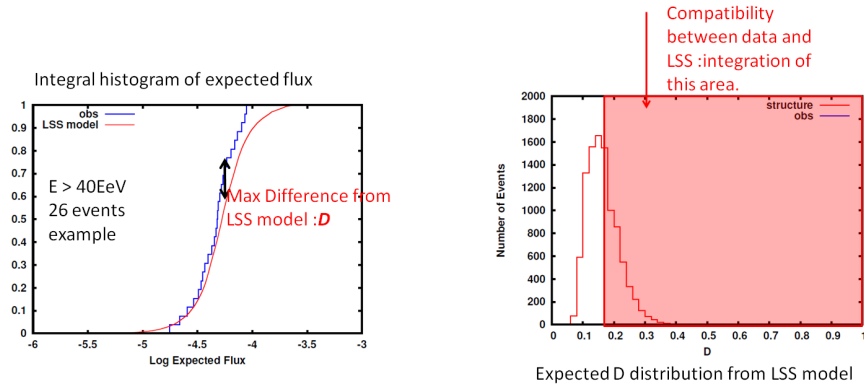

Figure 49: This figure shows an example of the procedure of the analysis using KS test. Left figure: an example of statistics D calculated between cumulative distribution function of data and LSS model. Right figure: an example of the simulated distribution of D from LSS model and the corresponding region of $\Pr(D > D_{obs})$.

6.4. Conversion of Coordinate System

We converted arrival direction of each reconstructed event to the direction in the equatorial coordinate(J2000) and then to the direction in the Galactic coordinate.

Converted data is plotted in Fig.54. We compare this result with large scale structure.

The right ascension and declination dependence of the distribution of the data is shown in Fig.51 and Fig.52. The uniform distribution expected from the TA exposure is consistent with the data in this coordinate from the point of χ^2 and KS test.
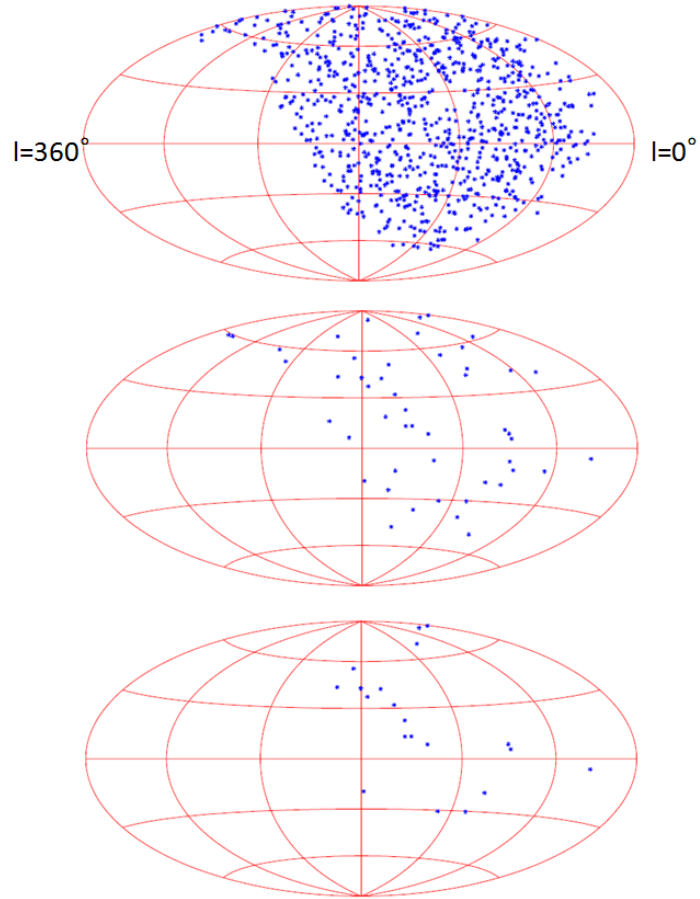
Figure 50: Arrival directions of UHECRs projected in the Galactic coordinate. Top: E > 10 EeV, arrival directions of observed 856 events, Middle: E > 40 EeV, arrival directions of observed 49 events, Bottom: E > 57 EeV, arrival directions of observed 20 events
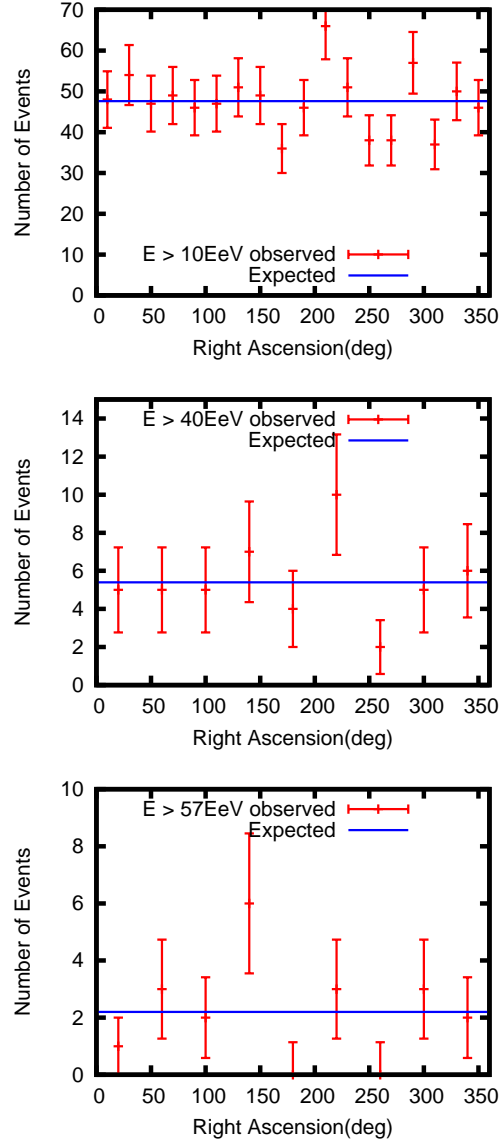
Figure 51: Right ascension dependence of the arrival directions of UHECRs. Top: E >
10 EeV, arrival directions of observed 856 events, Middle: E > 40 EeV, arrival directions
of observed 49 events, Bottom: E > 57 EeV, arrival directions of observed 20 events.
χ^2/d.o.f. is 0.76, 0.28 and 1.2, respectively. KS probabilities are 0.92, 0.83 and 0.44,
respectively.
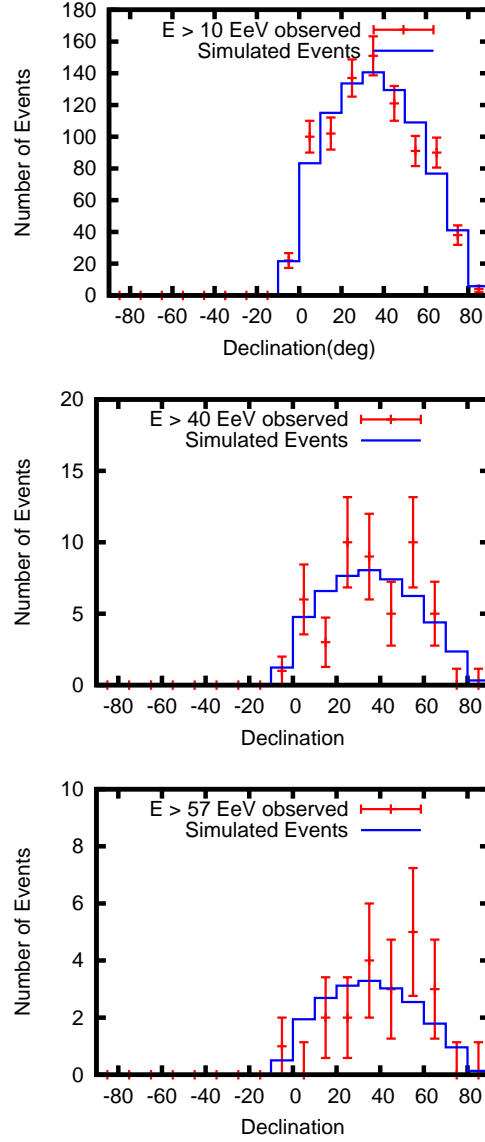
Figure 52: Declination dependence of the arrival directions of UHECRs. Top: E > 10 EeV, arrival directions of observed 856 events, Middle: E > 40 EeV, arrival directions of observed 49 events, Bottom: E > 57 EeV, arrival directions of observed 20 events. χ^2/d.o.f. is 1.7, 0.78 and 0.49, respectively. KS probabilities are 0.40, 0.91 and 0.29, respectively.

6.5. Comparison with Isotropy

We calculated the compatibility between observed arrival directions and isotropic distribution. We generated 1,000,000 Monte Carlo events which follow TA exposure. TA exposure is calculated using the formula shown in [114].

We can assign corresponding relative exposure value to each observed event, so we compared observed events with Monte Carlo events using one-dimensional KS test referring relative exposure. Calculated KS probability is shown in table.1. This result says that the observed arrival directions are compatible with isotropic distribution in this data set.

	E_{th} =10 EeV	E_{th} =40 EeV	E_{th} =57 EeV
p-value for isotropy model	0.40	0.64	0.17

Table 1: p values for isotropy model
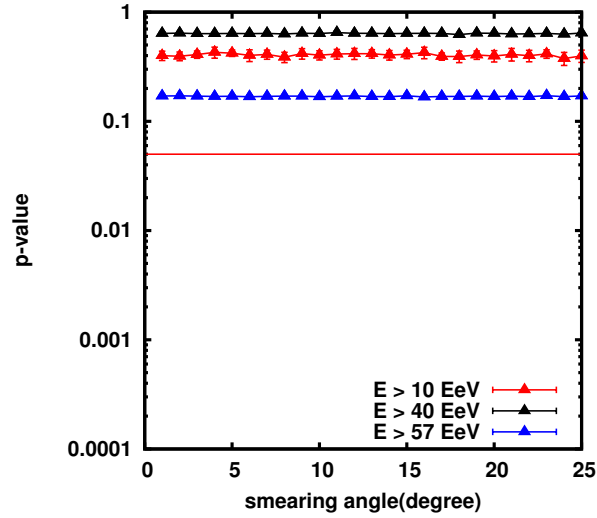
Figure 53: E_{th} =10, 40, 57 EeV. Compatibility between isotropy model and data. The compatibility does not depend on the smearing angle of the exposure.

85
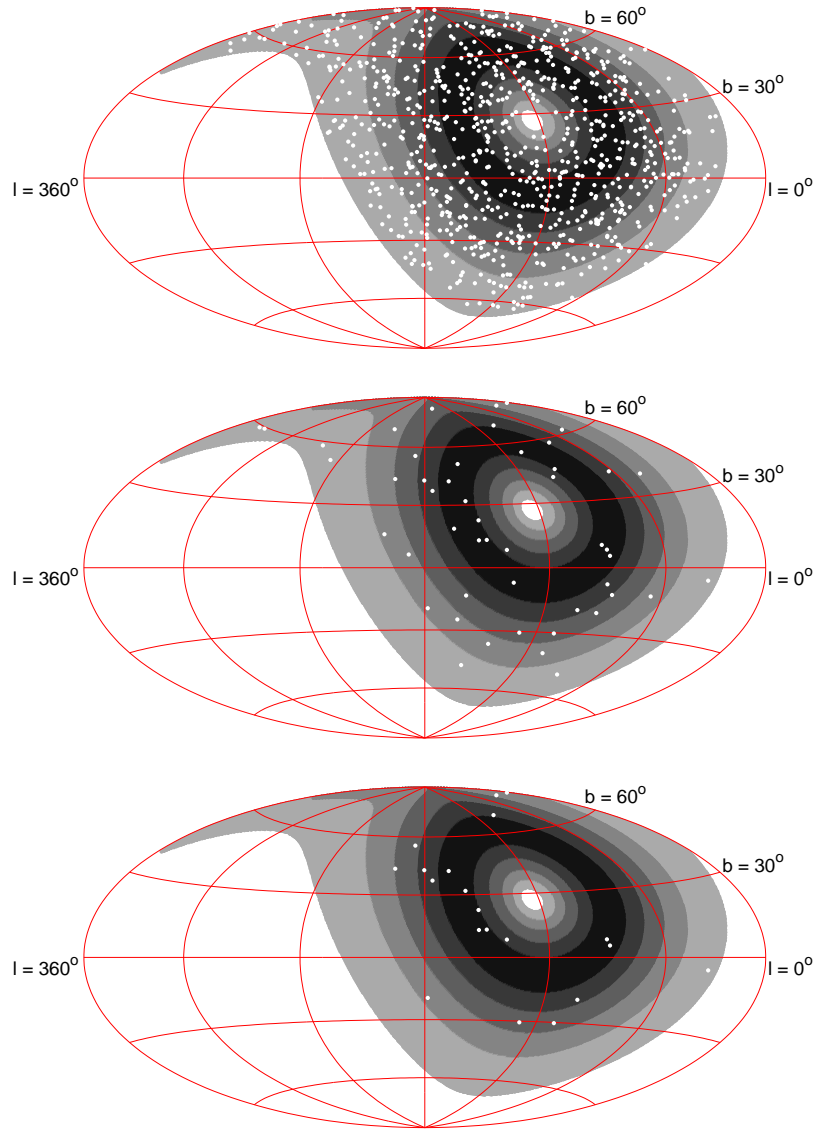
Figure 54: Contour maps of TA relative exposure are overlaid with observed arrival directions of UHECRs. Each contour band contains one fifth of the total exposure. Top: E > 10 EeV, arrival directions of observed 856 events, Middle: E > 40 EeV, arrival directions of observed 49 events, Bottom: E > 57 EeV, arrival directions of observed 20 events

6.6. Comparison with LSS

6.6.1. Comparison without Regular GMF

We calculated the compatibility between observed arrival directions and LSS model following the procedure described in the Section.6.1 and 6.3 We generated 1,000,000 Monte Carlo events which follow LSS model. Contour maps of expected flux χ_{tot} from LSS model are overlaid with observed arrival directions of UHECRs in Fig.55.

We can assign corresponding expected flux value to each observed event. The observed events are compared with Monte Carlo events using one-dimensional KS test referring this expected flux from LSS model. Calculated KS probability is shown in Fig.56. The observed arrival directions above 40 EeV are compatible with LSS model in this data set within 95 % confidence level. The observed arrival directions above 57 EeV are compatible with LSS model in this data set within 95 % confidence level when the smearing angle θ_s is less than 18 degrees. On the other hand, the observed arrival directions above 10 EeV are incompatible with LSS model in this data set at least 95 % confidence level.

This result means that we have a larger statistics at lower energies and we can say which model is compatible with the data above 10 EeV. Fig.57 shows the separation between isotropy and LSS model when the smearing angle is 6 degrees. We can see that the separation between isotropy and LSS is larger at lower energies depending on the statistics despite the larger contamination of the isotropic component which comes far from 250 Mpc at low energies. Especially the data around 10 EeV, the effect of the magnetic deflections is expected to be larger, so the regular component should be included more carefully. This study is shown in the next section.
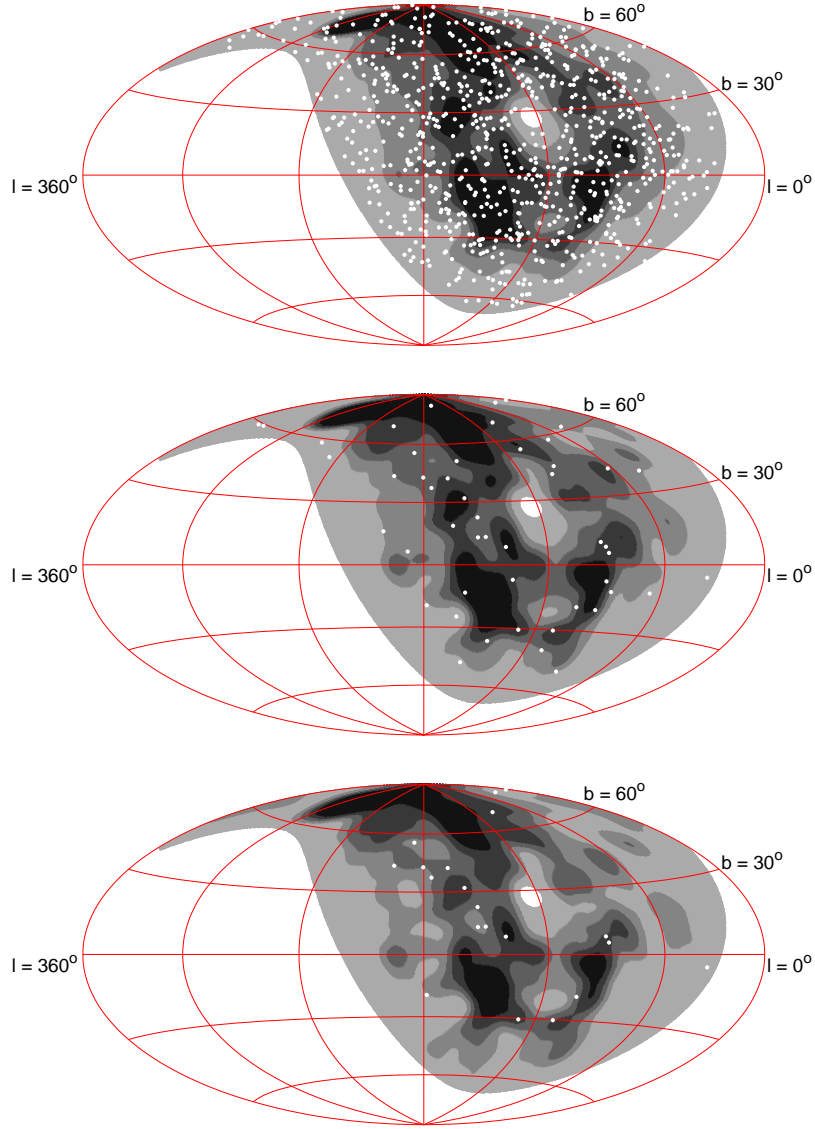
87

Figure 55: Contour maps of expected flux χ_{tot} from LSS model are overlaid with observed arrival directions of UHECRs in this figure. Top: E > 10 EeV, smearing angle $\theta_s = 6°$ expected flux map, 856 observed events overlaid.Each contour band contains one fifth of the total flux, Middle: E > 40 EeV, smearing angle $\theta_s = 6°$, 49 events, Bottom: E > 57 EeV, smearing angle $\theta_s = 6°$, 20 events.
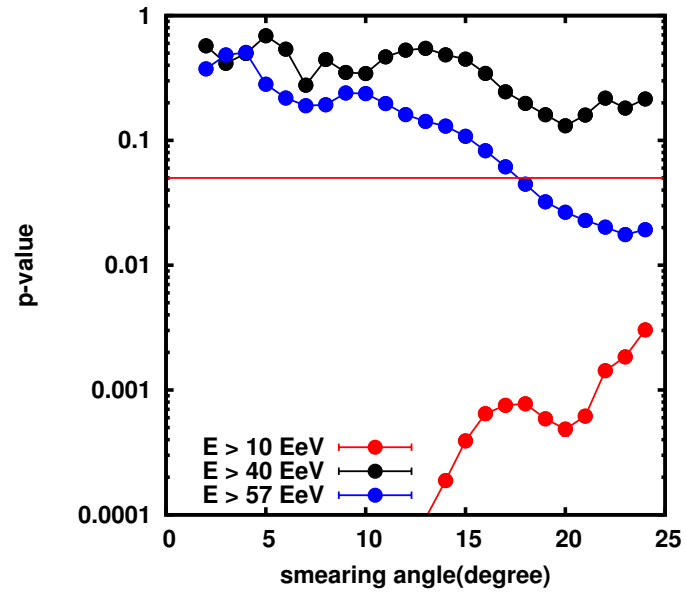
Figure 56: E_{th} =10, 40, 57 EeV. Compatibility between LSS model and data using KS test.
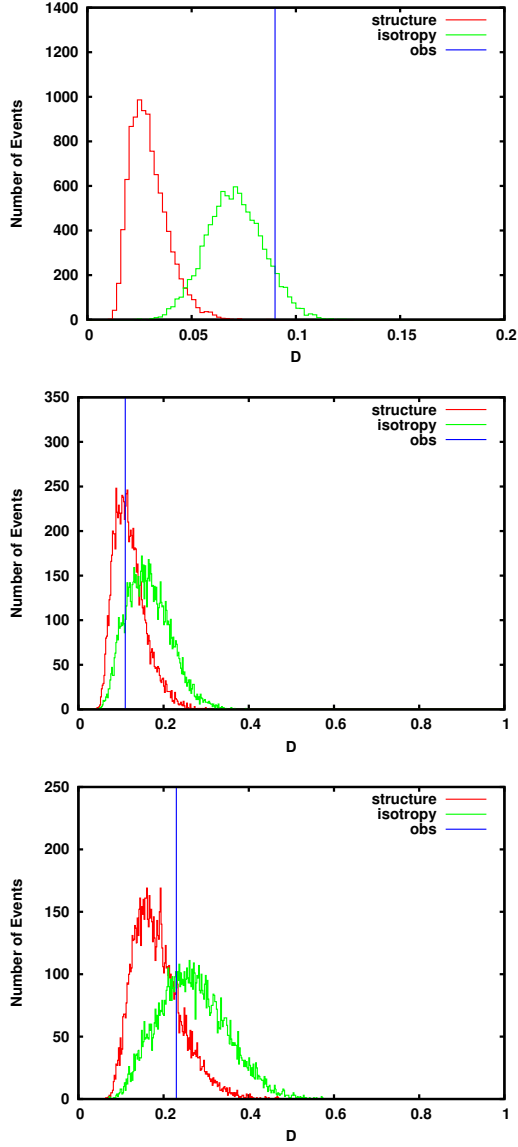
Figure 57: E_{th} =10, 40, 57 EeV. Expected D distributions of isotropy and LSS models are shown here when the smearing angles are 6 (deg). This D value is the maximum difference in the cumulative number distribution between the sample and LSS model referring χ value of LSS. The top figure is the case when E_{th} =10 EeV, the middle figure is the case when E_{th} =40 EeV and the bottom figure is the case when E_{th} =57 EeV. The observed D is 0.09, 0.11 and 0.23 correspondingly.

6.6.2. Comparison with Regular GMF

The observed arrival directions above 10 EeV are incompatible with LSS model in this data set at least 95 % confidence level. The uncertainty of the regular Galactic magnetic field is large. Especially about the toroidal halo field model, the uncertainty of the field strength and the geometry seem to be directly related to the uncertainty of the trajectory of UHECRs because much large steradian from the Earth is occupied by the Galactic halo than the Galactic disk.

We search for the regular Galactic magnetic field model which improve the compatibility between the data and LSS model above 10 EeV. The compatibility between the data and LSS model with various regular Galactic field model and with 1-25° smearing angle is calculated in this search. We tested the disk field models and halo field models in Ref.[83] and Ref.[121]. As a result, the regular Galactic magnetic field without toroidal halo field model does not improve the present compatibility, but the regular Galactic magnetic field with toroidal halo field model can improve the compatibility.

Then we search for the good parameters of the toroidal field models which are also accepted from the point of goodness of fit between RM and the regular GMF model. At this time, we fix the disk field model parameters which are called as benchmark model in Ref.[121]. Fig.58 shows an example of the fit of RM results. If the χ^2 of the goodness of fit is small enough, the parameters of the regular GMF is accepted. The reduced χ^2 in the Fig.58 is 2.16 for example. If the reduced χ^2 is from 2.16 to about 2.46, the parameters are accepted. This range of the reduced χ^2 is approximately corresponds to $1\,\sigma$ from the best fit value. Fig.59 and 60 shows the parameter dependence of the compatibility between the data and LSS when the halo field strength which corresponds to B_0^H in the equation (31) is 3 uG and 4 uG respectively. Thicker halo field or stronger halo field tends to improve the compatibility between the data and LSS in these figures. This is because the thicker or stronger halo fields lead to larger coherent magnetic deflection of UHECRs.

The maximum field strength of the halo field B_0^H is constrained from the synchrotron radio-emission from the Galactic relativistic electrons according to Ref.[121]. This constraint favors halo fields with 2-5 uG, so we searched parameters with $B_0^H \leq 4$ uG here.

The best parameters are shown in table.2 as far as we searched. Fig.61 shows the deflection angle pattern maps using this GMF model. Calculated expected flux $\chi_{tot} = A(l,b)\Phi_{tot}(l,b,E_{th})$ maps using this GMF model are

shown in Fig.62. Calculated KS probabilities using this GMF model above 10 EeV are shown in Fig.64. An example of the compatibility between the LSS model with disk only regular GMF and the data is also shown in the same figure. These types of model cannot drastically improve the compatibility because of their smaller magnetic deflections.

Calculated KS probabilities using this GMF models above 40 and 57 EeV are shown in Fig.63. The compatibilities between data and LSS look also good at higher energy thresholds with this model. So $E > 40$ EeV and $E > 57$ EeV data is compatible with LSS models with or without regular GMF. This is because of small amount of data. The separation is not clear now between different expected distributions of $E > 40$ EeV and $E > 57$ EeV data like in Fig.57.

On the other hand, the model dependence of the GMF models changes the compatibility of LSS model with data when energy threshold is 10 EeV. This is because of the larger amount of data above 10 EeV and the effect of larger magnetic deflections in the lower energy.

Local(position at the Sun) field strength (uG)	2.0
Distance to the first field reversal from the Sun (kpc)	-0.6
Pitch angle (deg)	-6.
Disc height (kpc)	1.0
Distance from the Sun to the Galactic center (kpc)	8.5
Disk field model	BSS
B_0^H in the equation (31) (uG)	4
R_0^H in the equation (31) (kpc)	8
z_0^H in the equation (31) (kpc)	1.3
z_1^H when $|z| < z_0^H$ in the equation (31) (kpc)	0.25
z_1^H when $|z| \geq z_0^H$ in the equation (31) (kpc)	1.2

Table 2: Galactic magnetic field model parameters are shown here which are picked as a best parameter from the point of the compatibility between the data and LSS above 10 EeV.
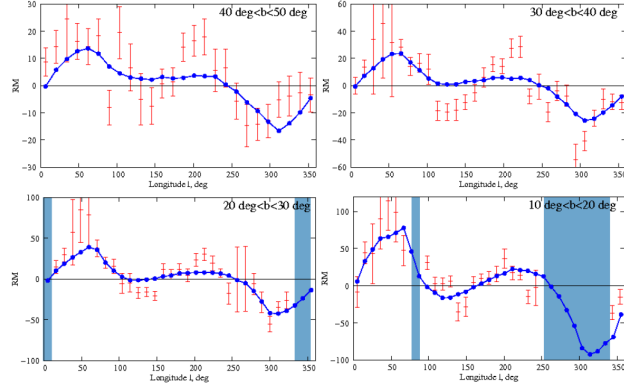
Figure 58: An example of the fit result of the RM data which is observed by NVSS [123]. Blue solid lines correspond to the fit model. The red points are observed RM results by NVSS. The shaded region is not included in the fit. [121]
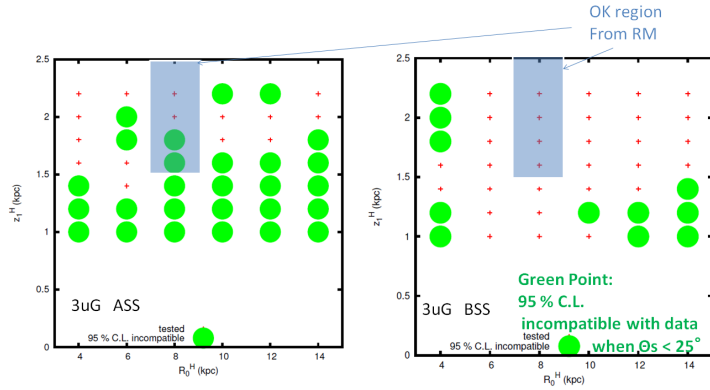

Figure 59: The parameter dependence of the compatibility between the data above 10 EeV and LSS when the halo field strength which corresponds to B_0^H in the equation (31) is 3 uG. The vertical axis z_1^H when $|z| \geq z_0^H$ corresponds to the thickness of the halo field. The horizontal axis R_0^H corresponds to the horizontal range of the halo field. The compatibility between the data and LSS is tested but not rejected with some smearing angles within 25 (deg) at red points. The gray shaded area is the accepted region from the point of fit between RM and regular GMF model. The boundary condition of the gray area is about 1 σ difference from the best fit parameters.

93
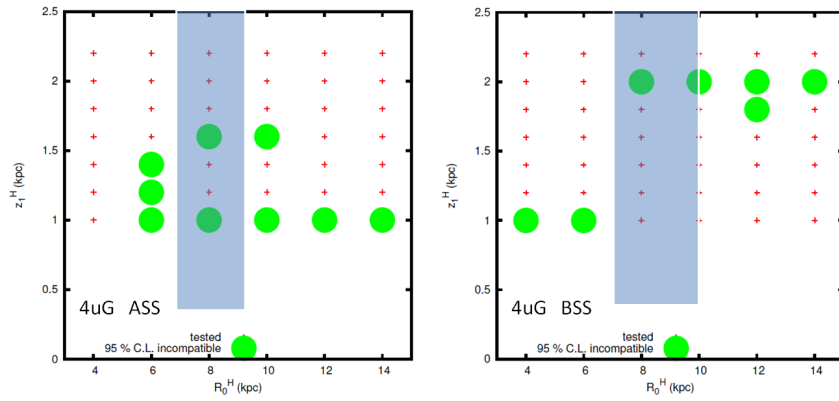
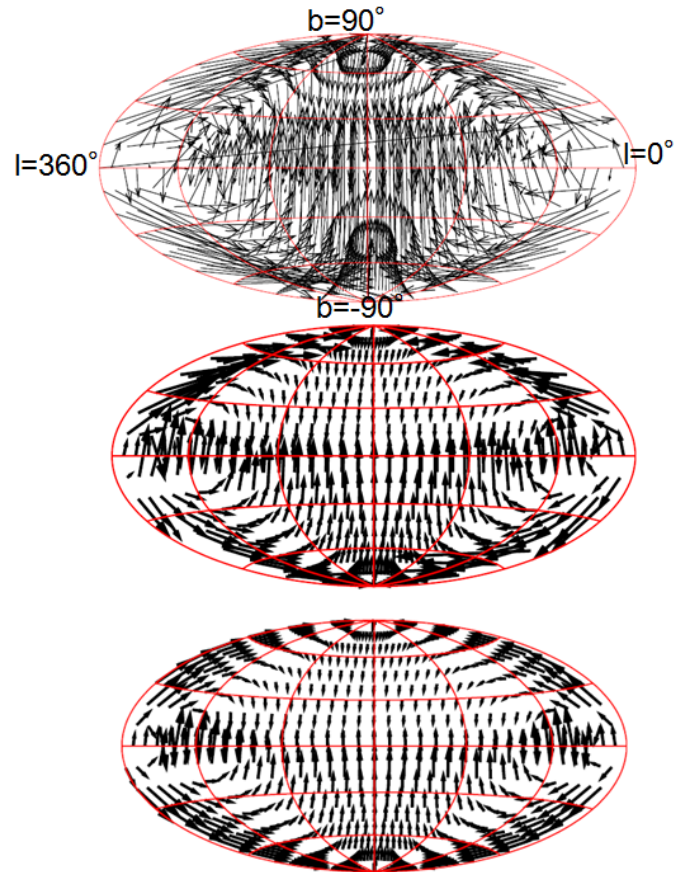Figure 60: This figure is completely same thing as Fig.59 except for B_0^H condition. $B_0^H = 4$ uG in this figure.

Figure 61: This figure is the deflection angle pattern map by GMF which is shown in table.2. Top: E = 10 EeV.,Middle:E = 40 EeV, Bottom: E = 57 EeV. The head of the arrow is the original direction from the observed direction.
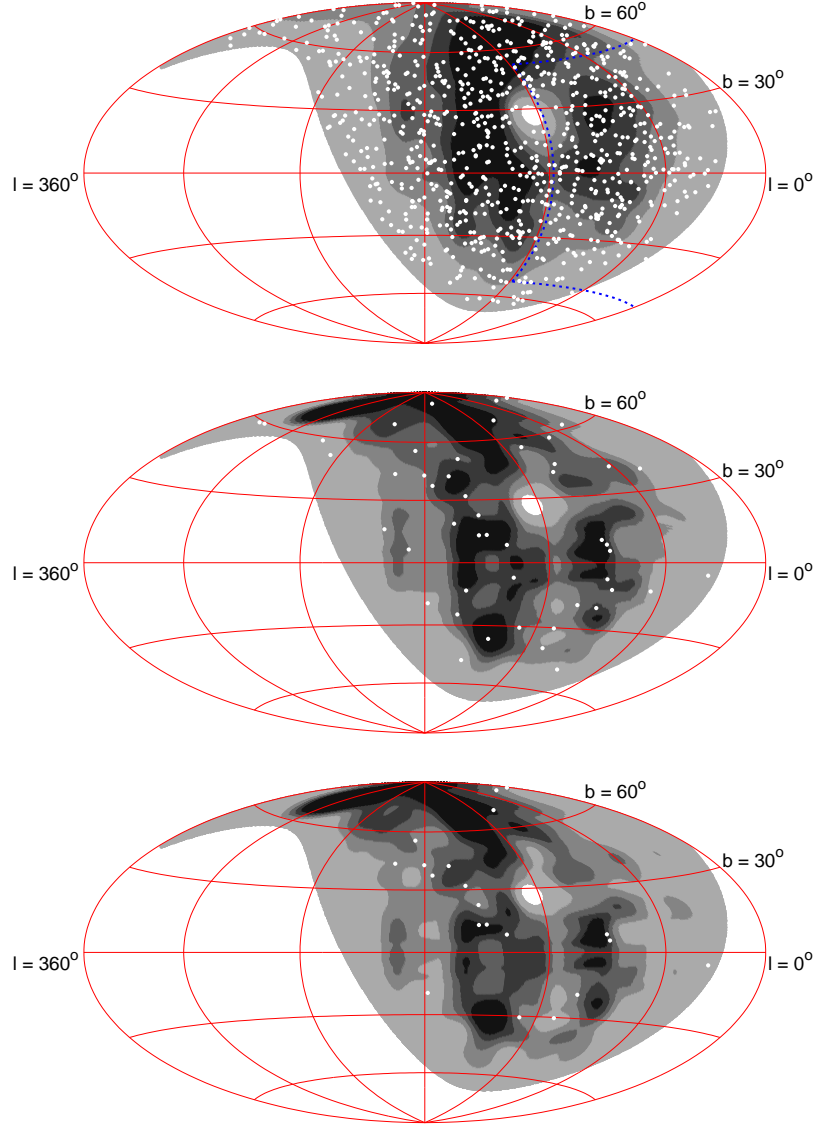
Figure 62: Contour maps of expected flux χ_{tot} from LSS model are overlaid with observed arrival directions of UHECRs in this figure considering GMF which is shown in table.2. Top: E > 10 EeV, smearing angle $\theta_s = 6°$, Middle: E > 40 EeV, smearing angle $\theta_s = 6°$, Bottom: E > 57 EeV, smearing angle $\theta_s = 6°$.
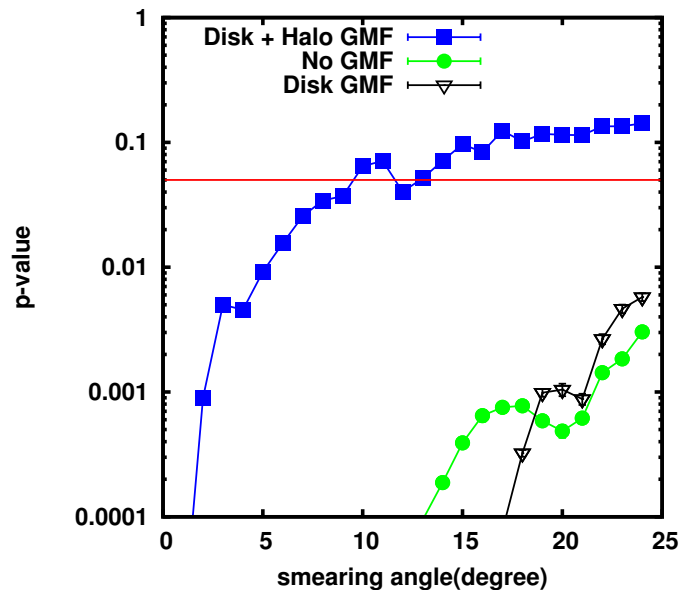
Figure 63: E_{th} =10 EeV. Compatibility between LSS with regular GMF and data is drawn as blue points. The GMF parameters are shown in table.2 with data. We exclude halo field from this model and we did the same test for comparison. P-values without regular GMF are also shown here for comparison.

6.6.3. Systematic Uncertainties depending on the Source Density

If there are so small number of sources, the expected flux distribution becomes rather irregular feature. So the observed arrival direction can be deviated from the LSS feature in this case. We checked whether the conclusion above 10 EeV can change or not if the source density is different in this section.

We are using about 100,000 galaxies of 2 Mass XSCz catalogue with weights within 250 Mpc. Firstly we determine the number source density which we want to test, and calculate how many galaxies are expected within 250 Mpc. The galaxies in this catalogue are selected as UHECR sources depending on the weights. In this process, the double counts of the galaxies are accepted. And then the same way as in Section.6.1 is carried out and the expected flux map is made. In this process, the selection of the galaxies as sources can be different. This selection fluctuate the flux map.

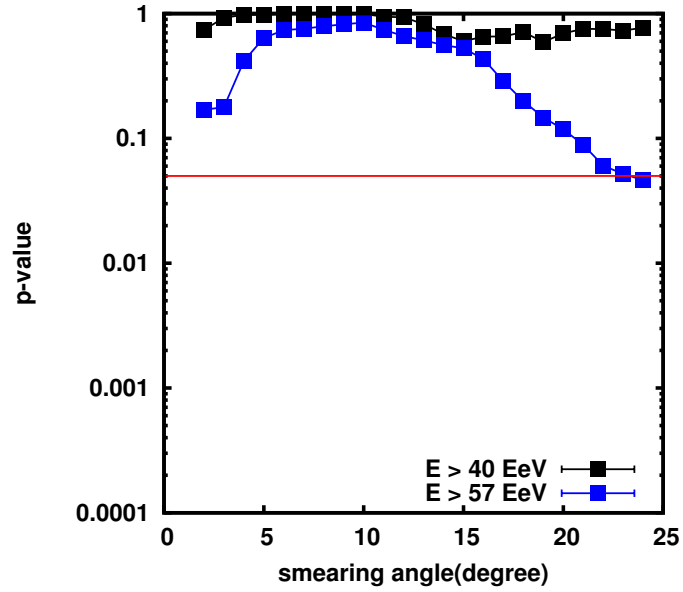Fig.65 is the result of p-value calculations when we compare the data

97

Figure 64: E_{th} =40, 57 EeV. Compatibility between LSS with regular GMF and data is drawn as blue points. The GMF parameters are shown in table.2 with data.

above 10 EeV with these model flux maps with 2 different source densities, $2 \cdot 10^{-4}$ Mpc^{-3} and $2 \cdot 10^{-5}$ Mpc^{-3}. According to Haverah Park result, the rough lower limit of the source density is 10^{-5} Mpc^{-3} [126]. According to Pierre Auger first result, the source density is estimated to be about 10^{-4} Mpc^{-3} [27] [127]. The source densities which we tested are around these source densities. P-values in Fig.65 is also very small with large smearing angle. So the conclusion does not change even if the source density is much smaller than our model.
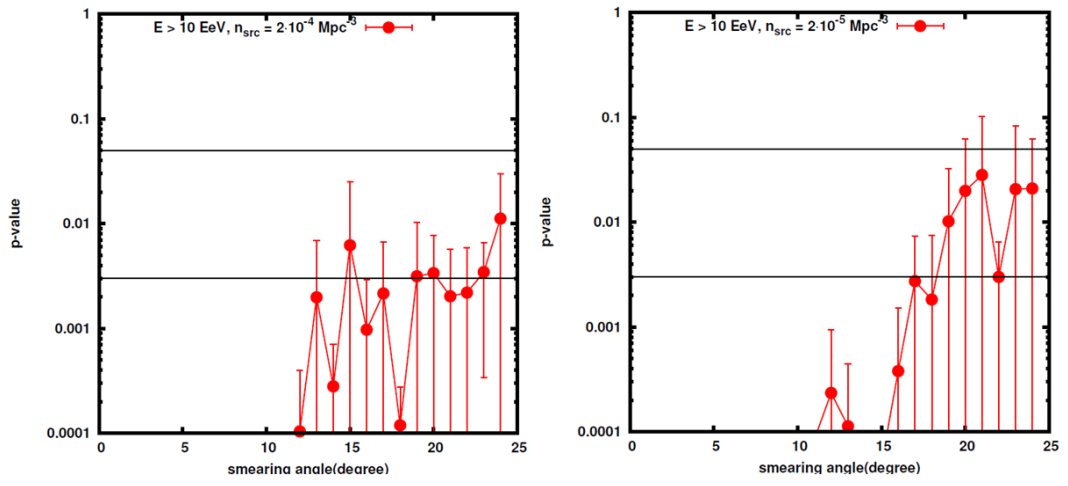
Figure 65: E_{th} =10 EeV. Compatibility between LSS without GMF and data is drawn as red points. The expected source density is decreased from Fig.56. At the left figure, the source density $2 \cdot 10^{-4}$ Mpc^{-3} is applied, and the source density $2 \cdot 10^{-5}$ Mpc^{-3} is applied in the right figure.

7. Summary & Conclusions

TA SD steadily continues to observe UHECRs for more than 3 years with more than 97 % duty cycle. We used this SD data to search for the correlation with LSS.

We used galaxies in 2 Mass Extended Source Catalogue to represent the matter distribution in the LSS and calculated the propagation of UHECRs to the Earth. We used protons for the calculation reflecting the results of Xmax measurements by TA FD. The deflections by regular GMF, which is built consistent with Faraday rotation measurements, is taken into account. The random component of magnetic deflections of UHECRs is included in the propagation as a free parameter. We compared the arrival directions of UHECRs with the expected flux from the LSS using one-dimensional KS test.

The summary result of the comparison is shown in Figure 66. The compatibility of UHECR data with the isotropy is indicated by black triangles. The compatibility with isotropy is good irrespective of energy thresholds, and it is independent of the smearing angl as it should be.

The red squares and blue circles represent the compatibility with proton LSS model with and without GMF deflection. The compatibility with the proton LSS model without GMF deflection is below 0.3% CL for low energy threshold (E > 10 EeV) and below 5% CL for high energy threshold (E > 57 EeV) with smearing angle larger than 17 degrees. It should be noted that the anticipated smearing angle by the GMF may be about 3 degrees for 40 EeV and 10-15 degrees for 10 EeV. The compatibility with the proton LSS model improves significantly with an introduction of the GMF deflection as shown by the red squares in Figure 66, indicating the importance of the GMF effect in understanding the UHECR anisotropy.

This result is not consistent especially with the result of HiRes. The data rejected LSS in 95 % C.L. according to HiRes when the smearing angle is less than 10 degrees and the energies are above 40 and 57 EeV. Our LSS model is also consistent with the data in this energy range. HiRes does not have much statistics but the inconsistency with our result would exist especially at small smearing angles. Pierre Auger shows similar type of analysis using likelihood test and the smoothed density maps which is generated using 2 Mass Redshift Survey (2MRS) and Swift-BAT catalog of AGNs. This test is carried out for the data above 57 EeV and the Auger arrival directions are compatible with models of the local matter distribution based on 2MRS

galaxies with a few degrees smoothing angles as a conclusion. This analysis adds isotropic fraction to the matter distribution, so the discussion may be needed at this point but our result seems to be rather consistent with this result. The AGASA does not show similar analysis, but the data above 40 EeV is both consistent with isotropy and LSS because of small amount of data according to the result of cross-correlation with LSS which is generated based on IRAS galaxies. This result is consistent with our result.

In summary, we observed the UHECR arrival directions in the northern hemisphere and found that there is no deviation from the isotropy. The UHECR data is also compatible with the proton LSS model when the effect of appropriate GMF is taken into account. It should be noted that the compatibility with the LSS requires a relatively strong (4 μG) and thick (1.2 kpc FWHM) halo GMF, yet consistent with the existing Faraday rotation measures.
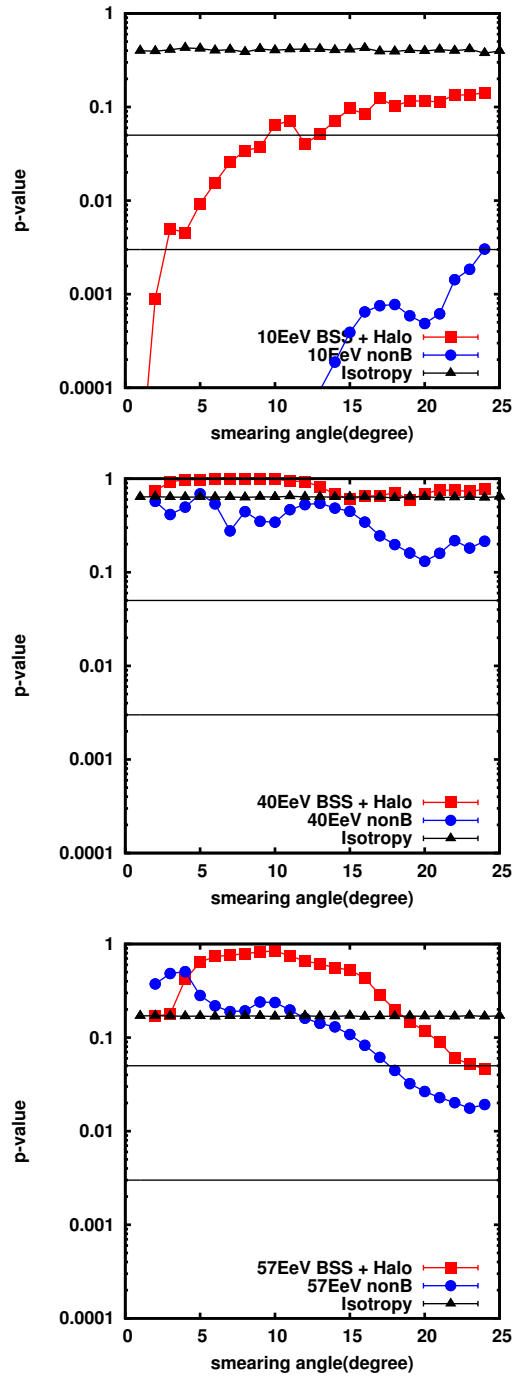
Figure 66: Summary plot of compatibility between LSS/isotropy model and data.

Acknowledgments

Appendix A.Space Charge Effect

When we assume that parallel plane electrodes are in a vacuum and that current between electrodes i does not depend on the distance from one electrode, we can calculate space charge effect.[111]
Here initial velocity from one electrode is defined as v_0, distance from one electrode is x, electric potential from one electrode is $\phi(x)$, electric field just above one electrode is E_0, space charge between electrodes is $\rho(x)$, $\phi(0) = 0$, voltage between electrodes is V and distance between electrodes is L.
We can get following equations in this assumption between electrodes.

$$i = -\rho v \tag{43}$$

$$-\frac{d^2\phi}{dx^2} = \frac{\rho}{\epsilon_0} \tag{44}$$

$$\frac{1}{2}m_e(v^2 - v_0^2) = e\phi \tag{45}$$

When the current is completely limited by space charge,E_0 and v_0 are zero. In this case,we can get

$$\phi(x) = \left(\frac{3}{4}\right)^{4/3} \left(\frac{2i}{\epsilon_0}\right)^{2/3} \left(\frac{2m_e}{e}\right)^{1/3} x^{4/3} \qquad (46)$$

So the current limit between electrodes is

$$i = \frac{8}{9}\epsilon_0 \sqrt{\frac{e}{2m_e}} \frac{V^{3/2}}{L^2}. \qquad (47)$$

So the current limit is expected to show this $V^{3/2}$ feature.

References

[1] http://www.telescopearray.org/

[2] J.N. Matthews, for the Telescope Array Collaboration: Proc. of 31st ICRC Łódź 2009, #1386.

[3] M. Takeda *et al.* Phys. Rev. Lett. 81, 1163(1998).

[4] T. Abu-Zayyad *et al.* Phys. Rev. Lett. 92, 151101(2004).

[5] K. Greisen, Phys Rev. Lett. 16, 748 (1966). and G.T. Zatsepin and V.A. Kuz'min, Sov. Phys. JETP. Lett. 4, 78 (1966).

[6] V. Berezinsky, J. of Phys: Conf. Series 120, 012001 (2008).

[7] J. Abraham *et al.* Pierre Auger Collaboration, Phys. Rev. Lett. 101, 061101 (2008).

[8] G.B. Thomson, arXiv:astro-ph/1010.5528 (2010).

[9] A. Taketa, Doctor Thesis in preparation (2012).

[10] J. Abraham *et al.* Pierre Auger Collaboration, Phys. Rev. Lett. 104, 091101 (2010).

[11] R.U. Abbasi *et al.* HiRes Collaboration, Phys. Rev. Lett. 104, 161101 (2010).

[12] Y. Tameda *et al.* , for the Telescope Array Collaboration: Proc. of 32nd ICRC 2011, #1268.

[13] M. Takeda *et al.* Astrophys. J. 522, 225(1999).

[14] P.G. Tinyakov & I.I. Tkachev, JETP. Lett. 74, 445 (2001).

[15] P.G. Tinyakov & I.I. Tkachev, Astropart. Phys. 18, 165 (2002).

[16] D.S. Gorbunov *et al.* Astrophys. J. 577, L93 (2002).

[17] R.U. Abbasi *et al.* HiRes Collaboration, Astrophys. J. 623, 164 (2005).

[18] R.U. Abbasi *et al.* HiRes Collaboration, Astropart. Phys. 27, 512 (2007).

[19] P. Abreu *et al.* Pierre Auger Collaboration, arXiv:astro-ph.HE/1009.1855v1 (2010).

[20] T. Okuda, Doctor Thesis (2011).

[21] D.S. Gorbunov & S.V. Troitsky, Astropart. Phys. 23, 175 (2005).

[22] R.U. Abbasi *et al.* HiRes Collaboration, Astrophys. J. 636, 680 (2006).

[23] J. Abraham, *et al.* Pierre Auger Collaboration, Science 318, 938 (2007).

[24] J. Abraham, *et al.* Pierre Auger Collaboration, Astropart. Phys. 29, 188 (2008).

[25] E. Waxman, K.B. Fisher & T. Piran, Astrophys. J., 636, 680 (2006).

[26] H. Yoshiguchi, S. Nagataki & K. Sato, Astrophys. J., 592, 311 (2003).

[27] H. Takami, K. Sato, Astrophys. J., 678, 606 (2008).

[28] T. Kashti, E. Waxman, JCAP, 05, 006 (2008).

[29] R.U. Abbash, *et al.* HiRes Collaboration, arXiv:astro-ph.HE/1002.1444v1 (2010).

[30] K. Ptitsyna & S. Troitsky, arXiv:astro-ph/0808.0367v2 (2008).

[31] A.M. Hillas, AARA&A 22,425 (1984).

[32] P.L. Biermann & P.A. Strittmatter, Astrophys. J., 322, 643 (1987).

[33] J.P. Rachen & P.L. Biermann, Astron. Astrophys. 272, 161 (1993).

[34] C.A. Norman, D.B. Melrose, & A. Achterberg, *Astrophys. J.*, 454, 60 (1995).

[35] F.A. Aharonian, Mon. Not. R. Astron. Soc. 332, 21 (2002).

[36] V.S. Berezinsky, A. Gazizov, & S. Grigorieva, Phys. Rev. D 74, 043005 (2006).

[37] E.G. Berezhko, *Astrophys. J.*, 684, L69 (2008).

[38] C.D. Dermer, S. Razzaque, J.D. Finke, & A. Atoyan, New Journal of physics 11, 065016 (2008).

[39] R. Schopper, G.T. Birk, & H. Lesch, *Astrophys. J.*, 17, 347 (2001).

[40] M. Milgrom & V. Usov, Astrophys. J. 449, L37 (1995).

[41] E. Waxman, Phys. Rev. Lett. 75, 386 (1995).

[42] M. Vietri, Astrophys. J. 453, 883 (1995).

[43] C.D. Dermer, Astrophys. J. 574, 65 (2002).

[44] E. Waxman, Astrophys. J. 606, 988 (2004).

[45] K. Murase, K. Ioka, S. Nagataki, & T. Nakamura, Phys. Rev. D 78, 023005 (2008a).

[46] K. Murase, K. Ioka, S. Nagataki, & T. Nakamura, Astrophys. J. 651, L5 (2006).

[47] X.-Y. Wang, S. Razzaque, P. Mészáros, & Z.-G. Dai, Phys. Rev. D 76, 083009 (2007).

[48] R.J. Protheroe & A.P. Szabo, Phys. Rev. Lett. 69, 2885 (1992).

[49] E. Boldt, & P. Ghosh, Mon. Not. R. Astron. Soc., 307, 491 (1991).

[50] A. Nerov, & D. Semikoz, New Astron. Rev., 47, 693 (2003).

[51] A. Nerov, P. Tinyakov, & I. Tkachev, J. Exp. Theor. Phys., 100, 656 (2005).

[52] A. Nerov, D. Semikoz, & I. Tkachev, arXiv:astro-ph/0712.1737 (2007).

[53] J. Arons, *Astrophys. J.*, 589, 871 (2003).

[54] K. Murase, P. Mészáros, & B. Zhang, Phys. Rev. D 79, 103001 (2009).

[55] A. Venkatesan, M.C. Miller, & A.V. Olinto, *Astrophys. J.*, 484, 323 (1997).

[56] H. Kang, D. Ryu, & T.W. Jones, *Astrophys. J.*, 456, 422 (1996).

[57] S. Inoue, G. Sigl, F. Miniati, & E. Armengaud, arXiv:astro-ph/0701167 (2009).

[58] E. Fermi, Phys. Rev., 75, 1169 (1949).

[59] R. Blanford & D. Eichler, Phys. Rept. 154, 1 (1987).

[60] A.R. Bell, Mon. Not. R. astr. Soc., 182, 147 (1978).

[61] F.M. Rieger & P. Duffy, *Astrophys. J.*, 617, 155 (2004).

[62] E.V. Derishev, F.A. Aharonian, V.V. Kocharovsky, & VI. V. Kocharovsky, Phys. Rev. D 68, 043003 (2003).

[63] M. Ostrowski, arXiv:astro-ph/0801.1339 (2008).

[64] J.G. Kirk, A.W. Guthmann, Y.A. Gallant, & A. Achterberg, *Astrophys. J.*, 542, 235 (2000).

[65] P. Blasi & M. Vietri, *Astrophys. J.*, 626, 877 (2005).

[66] M. Lemoine & G. Pelletier, *Astrophys. J.*, 589, L73 (2003).

[67] E. Waxman, Phys. Rev. Lett. 75, 386 (1995).

[68] E. Waxman, Lect. Notes. Phys. Vol. 576 (2001), p. 122.

[69] P. Bhattacharjee & G. Sigl, Physics Reports, 327, 109B (2000).

[70] D.N. Spergel *et al.* WMAP Collaboration, Astrophysical. J. Suppl. 143, 175 (2003), D.N. Spergel *et al.* D.N. Spergel *et al.* Ap.J.S. 170, 377 (2007).

[71] D. Harari, S. Mollerach, & E. Roulet, JCAP, 11, 12 (2006).

[72] R. Aloisio, V.S. Berezinsky, & S. Grigorieva, arXiv:astro-ph/0802.4452v3 (2008).

[73] K. Dolag, D. Grasso, V. Springel, & I. Tkachev, arXiv:astro-ph/0410419v2 (2005).

[74] D. Ryu, H. Kang, J. Cho, & S. Das, arXiv:astro-ph/0805.2466v1 (2008).

[75] G. Sigl, F. Miniati, & T. A. Enßlin, arXiv:astro-ph/0401084v2 (2004).

[76] H. Kang, S. Das, D. Ryu, & J. Cho, arXiv:astro-ph/0706.2597v2 (2008).

[77] P.G. Tinyakov & I.I. Tkachev, Astropart. Phys. 24, 32-43 (2005).

[78] E. Roulet, J. Mod. Phys. A 19, 1133 (2004). (arXiv:astro-ph/0310367 (2004))

[79] R.J. Rand & S.R. Kulkarni, *Astrophys. J.*, 343, 760 (1989). H. Ohno & S. Shibata, MNRAS, 262, 953 (1993).

[80] P.P. Kronberg, K.J. Newton-McGee, arXiv:astro-ph.GA/0909.4753v1 (2009)

[81] H. Men, K. Ferriére, & J.L. Han, A&A, 486, 819 (2008).

[82] J.L. Han, K. Ferriére, & R.N. Manchester, *Astrophys. J.*, 610, 820 (2004).

[83] X.H. Sun, W. Reich, A. Waelken, & T.A. Enßlin, A&A, 477, 573 (2008).

[84] J.L. Han & G.J. Qiao, A&A, 288, 759 (1994).

[85] J.L. Han, G.J. Qiao, & R.N. Manchester, MNRAS, 306, 371 (1999b).

[86] S.A. Mao, B.M. Gaensler, M. Haverkorn, E.G. Zweibel, G.J. Madsen, N.M. McClure-Griffiths, A. Shukurov, P.P. Kronberg, arXiv:astro-ph.GA/1003.4519v1 (2010)

[87] C. Indrani, A.A. Deshpande, New Astronomy, 4, 33 (1998).

[88] J.L. Han, R.N. Manchester, A.G. Lyne, & G.J. Qiao, *Astrophys. J.*, 507, L17 (2002).

[89] T. Gaisser, Cosmic Rays and Particle Physics, Cambridge Univ. Press (1991).

[90] M.S. Longair, High energy astrophysics(Cambridge Univ.Press,1981)

[91] M. Teshima *et al.* , J.Phys.G: Nucl.Phys 12 (1986) 1097-1113

[92] A.M. Hillas, Proc. 12th ICRC, Hobart, 3, 1001 (1971).

[93] H.Y. Dai *et al.* , J. Phys. G, 14, 793 (1988).

109

[94] M.S. Longair, High energy astrophysics 2nd Edition (Cambridge Univ.Press,1992)

[95] AGASA Spectrum data up to 2003/December.

[96] Bird *et al.* , *Astrophys. J.*, 424, 491 (1993).

[97] http://www.auger.org/technical_info/spectrum2008/Flux_systematic_info.txt

[98] Egorova *et al.* , Nucl. Phys. B(Proc Suppl), 136, 3 (2004).

[99] http://www.akeno-icrr.u-tokyo.ac.jp

[100] T. Nonaka, for the Telescope Array Collaboration: Proc. of 31st ICRC Łódź 2009, #977.

[101] A. Taketa, for the Telescope Array Collaboration: Proc. of 31st ICRC Łódź 2009, #924.

[102] H. Tokuno, for the Telescope Array Collaboration: Proc. of 31st ICRC Łódź 2009, #942. and L.M. Scott, for the Telescope Array Collaboration: Proc. of 31st ICRC Łódź 2009, #1148.

[103] T. Tomida, for the Telescope Array Collaboration: Proc. of 31st ICRC Łódź 2009, #801.

[104] Y. Tsunesada, for the Telescope Array Collaboration: Proc. of 31st ICRC Łódź 2009, #828.

[105] T. Shibata, for the Telescope Array Collaboration: Proc. of 31st ICRC Łódź 2009, #790.

[106] http://cosmos.n.kanagawa-u.ac.jp/cosmosHome/index.html

[107] K. Kasahara & F. Cohen, In Proc. 30th Int. Cosmic Ray Conf., 4, 581-584 (2008).

[108] F. Cohen & K. Kasahara, In Proc. 30th Int. Cosmic Ray Conf, 4, 585-588 (2008).

[109] NSPB320BS Spec Sheet,Nichia Chemical Industries Co.,Ltd.

[110] 9124B series Spec Sheet,ElectronTubes Co.,Ltd.

[111] Langmuir et al. Phys.Rev. 21, 419-435 (1923).

[112] M.Takeda et al., Astropart.Phys. 19 447-462 (2003).

[113] S.Yoshida et al.,J.Phys.G:Nucl.Part.Phys.20 651-664 (1994).

[114] P. Sommers, Astropart. Phys. 14, 271, (2001).

[115] T. Jarrett, arXiv:astro-ph/0405069 (2004).

[116] P.P. Kronberg Rep.Prog.Phys. 325-382 (1994).

[117] H.B.J. Koers & P.G. Tinyakov, MNRAS 399: 1005, (2009).

[118] H.B.J. Koers & P.G. Tinyakov, JCAP 0904: 003, (2009).

[119] V.S. Berezinsky *et al.* , Astrophysics of Cosmic Rays, North-Holland, Amsterdam, (1990); T. Gaisser, Cosmic Rays and Particle Physics, Cambridge Univ. Press, (1991).

[120] H.B.J. Koers & P.G. Tinyakov, PRD 78, 083009, (2008).

[121] M.S. Pshirkov, P.G. Tinyakov, P.P. Kronberg & K.J. Newton-McGee, arXiv:astro-ph.GA/1103.0814v1 (2011).

[122] T. Stanev, *Astrophys. J.*479(1997)290; Han & Qiao, A&A 288, 759 (1979).

[123] A.R. Taylor, J.M. Stil, C. Sunstrum, *Astrophys. J.*702, 1230 (2009).

[124] M. Prouza & R. Šmída, A&A, 410, 1 (2003).

[125] K.O. Thielheim & W. Langhoff, J. Phys. A: Gen. Phys. 1, 694 (1968).

[126] E. Waxman, K.B. Fisher & T. Piran, Astrophys. J., 483, 1 (1997).

[127] A. Cuoco *et al.* Astrophys. J., 702, 825 (2009).